Superresolved Swept-Wavelength Interferometry:
Fundamental Limits and Use in Three-Dimensional Surface Characterization

by

Martha Ingeborg Bodine

B.S., LeTourneau University, 2006

A thesis submitted to the
Faculty of the Graduate School of the
University of Colorado in partial fulfillment
of the requirement for the degree of
Doctor of Philosophy
Department of Electrical, Computer and Energy Engineering
2017

This thesis entitled:
Superresolved Swept-Wavelength Interferometry:
Fundamental Limits and Use in Three-Dimensional Surface Characterization
written by Martha I. Bodine
has been approved for the Department of Electrical, Computer and Energy Engineering

____
Robert R. McLeod

____
Eric D. Moore

Date_______________

The final copy of this thesis has been examined by the signatories, and we
find that both the content and the form meet acceptable presentation standards
of scholarly work in the above-mentioned discipline.

Bodine, Martha I. (Ph.D., Electrical, Computer and Energy Engineering)

Superresolved Swept-Wavelength Interferometry: Fundamental Limits and Use in Three-Dimensional Surface Characterization

Thesis directed by Professor Robert R. McLeod

The high signal-to-noise ratios typical of swept-wavelength interferometry (SWI) enable distance measurements to be superresolved with theoretical 2σ uncertainties as low as $1\text{x}10^{-4}$ of Fourier transform-limited resolution. This result was obtained by numerically comparing four frequency estimation methods: Local Linear Regression (LLR), Estimation of Signal Parameters via Rotational Invariance Techniques (ESPRIT), Nonlinear Least Squares (NLS), and Candan's Estimator (CE). For distances greater than 5 to 20 times the SWI system's transform-limited resolution, it was shown that CE provides the fastest and most accurate results, with precision approaching the Cramér–Rao bound.

Experimentally, the accuracy and precision of superresolved SWI were verified by comparing superresolved distance measurements against a known standard. In an SWI system with 34 μm transform-limited resolution, accuracy was shown to be greater than $2\text{x}10^{-3}$ of the transform limit, while thermal drift during data collection was shown to degrade the system's 1σ precision to approximately $9\text{x}10^{-2}$ of the transform limit.

In combination with superresolution, swept laser sources with long coherence lengths create the possibility for time-multiplexed SWI systems to make high-accuracy, single-shot, non-contact, three-dimensional measurements of arbitrarily shaped surfaces. An algorithm for reconstructing surface shapes from SWI distance measurements was developed, and an 8-channel prototype system was used to characterize the surfaces of an optical flat, a cylindrical lens, and a coin. Resulting accuracies of ±1 μm demonstrate that this measurement method is feasible and warrants further development.

This thesis is dedicated to my grandmother,

Ingeborg Bodine.

Acknowledgements

Among the many people who have supported and encouraged me through my Ph.D. research, the one I most want to thank is my advisor, Bob McLeod. His dedication to seeing his students through the whole of their graduate education has been one of the constants in my own time as a graduate student. No matter how busy he was, he always made time to hear about my latest results—or help me through the difficulties I was encountering when there were no results—propose and entertain new, wild ideas, and encourage me to aspire and work toward the big goals that I sometimes thought were beyond my reach.

I also want to thank Eric Moore for his guidance and his generosity with time and ideas, particularly during the early stages of my Ph.D. research. His vision, insight, and encouragement have been invaluable.

Finally, I want to thank the other members, past and present, of my research group. In particular, I am grateful to Anna Linnenberger for introducing me to the optics laboratory during my first year as a graduate student; to Amy Sullivan, our lab manager, for helping me learn to navigate many of the practical difficulties associated with research; and to Charlie Rackson, for our many enjoyable and productive conversations about 3D surface reconstruction.

Contents

List of Tables

List of Figures

Chapter 1

Introduction

1.1 Introduction to Superresolved Swept-Wavelength Interferometry

1.1.1 Measuring distance with light

On October 14, 1960, the Eleventh General Conference on Weights and Measures declared that the platinum bars that had defined the length of a meter for one hundred sixty-one years were to be replaced with a new standard: the vacuum wavelength of light [1]. The 1960 standard, defined as 1,650,763.73 vacuum wavelengths of the light from an atomic transition of krypton-86, was updated in 1983 to be the vacuum length of the path travelled by light in 1/299,792,458 of a second. In 2018, the 26th General Conference on Weights and Measures is expected to ratify a new definition of the *Système International d'Unités*, defining the value of a second by the frequency separation between the two hyperfine levels of the cesium-133 atom, and thereby establishing a new, and potentially final, international definition for the length of a meter [2].

The first use of electromagnetic radiation to measure distance predates the adoption of the 1960 meter standard by more than three decades. June 17, 1935 saw the first successful demonstration of radio detection and ranging—radar—on Orford Ness, a British peninsula on the coast of the North Sea [3]. This first system was a type of pulsed radar; it measured distance by measuring the time-of-flight of a radio-frequency pulse from a transmitter to the target and then back to a receiver. Twenty-five years later, in 1960, the invention of the laser [4] allowed similar time-of-flight measurements to be made at optical frequencies. Limited laser power restricted early laser ranging measurements to distances below a few kilometers [5], but by 1962, the first optical measurement of the distance between the earth and the moon had been achieved [6]. Today, light detection and ranging (LIDAR) systems exist which can measure distances of hundreds to thousands of meters with accuracies down to ±1 cm, even through scattering atmospheres containing dust, fire, fog, or smoke [7] [8].

At both radio and optical frequencies, the minimum distance that can be measured with a time-of-flight system is limited, fundamentally by the pulse width of a transmitted signal, and often functionally by the speed of electronic hardware. At radio frequencies, this limitation has been circumvented with frequency-modulated continuous-wave (FMCW) radar, which measures the distance between a transmitter and target by interfering a swept-frequency signal with a copy of that signal which has been delayed by the round-trip time-of-flight between the transmitter and the target [9] [10]. The periodicity of the received interference pattern is proportional to the time delay between the two copies of the swept-frequency signal, and the distance between transmitter and target can be obtained by multiplying the measured time delay by half the speed of light.

Many optical frequency analogs to swept-source FMCW radar have been developed. The first such system was likely described in 1981 by Eickhoff and Ulrich [11], who named their measurement technique optical frequency domain reflectometry (OFDR) to distinguish it from the similar time-of-flight measurement method known as optical time domain reflectometry (OTDR) [12]. Since 1981, OFDR systems have typically been developed to characterize fiber-optics networks and components [13] [14], or to be used in conjunction with fiber networks to measure quantities such as strain [15], temperature [16] [17], or vibration [18] [19]. Other swept-wavelength interferometry systems include FMCW ladar (laser detection and ranging) [20] [21] [22] [23], and swept-source optical coherence tomography (SS-OCT), which has been highly successful in measuring biological samples such as skin [24] [25], blood vessels [26] [27], and perhaps especially, the human eye [28] [29] [30] [31]. While these systems differ from each other in in the details of their system designs and experimental applications, they all share the same fundamental structure and measurement principle. They are all forms of swept-wavelength interferometry.

1.1.2 Superresolving swept-wavelength interferometry measurements

Two key characteristics of SWI account for its many and varied experimental successes. The first is its ability to simultaneously measure delay times to many reflectors, provided the reflectivity of each is small. The second is its sensitivity. Coherent, heterodyne detection and large bandwidths provide swept-wavelength interferometry measurements with characteristically high signal to noise ratios (SNRs), in some cases 70dB or greater [32]. For target reflectors with sufficient spacing between them, these high SNRs allow measurements of reflector spacing to be superresolved.

Traditionally, the resolution of a SWI system is set by the bandwidth of the swept source—put more specifically, the transform-limited resolution is equal to the inverse of sweep bandwidth. However, in at least two cases, SWI measurements have been reported in the literature as having both accuracy and precision exceeding the transform limit by several orders of magnitude [33] [20]. In a third, closely related case, spectral-domain OCT measurements of a dielectric thin film were reported to have precision of 10^{-4} of the OCT system's transform-limited resolution [34]. Despite these remarkable results, neither the limits of superresolution for SWI measurements—

i.e. the extent to which transform-limited resolution may be exceeded—nor the causes of those limits have been systematically quantified.

1.2 Superresolution Limits

Broadly speaking, the word superresolution may be used to describe any method that enhances the resolution of an imaging or measurement system beyond its traditional limits. During the last twenty years, superresolution methods have received a good deal of attention, particularly in the field of fluorescence microscopy. Structured illumination microscopy [35], photo-activated localization microscopy (PALM) [36], stochastic optical reconstruction microscopy (STORM) [37], and stimulated emission depletion (STED) microscopy [38] are likely the best-known superresolved microscopy methods, but others have been developed. Outside of microscopy, a number of computational approaches to superresolution have been proposed [39] [40] [41] [42], although their practical success has been limited [43]. Perhaps as a consequence of all this activity, the word "superresolution" has come to describe a large and somewhat disparate collection of measurement and imaging techniques. In this section, I attempt to draw a distinction between two classes of superresolution methods, those that exceed the diffraction limit, and those that exceed the resolution limit, in any given measurement or imaging system.

It is helpful to first step back and review the difference between the diffraction limit and the resolution limit of an imaging system. In a two-dimensional (2D) spatial imaging system, the diffraction limit is equal to the spot size of the image of a point source. Diffraction-limited spot size is inversely proportional to the numerical aperture (NA) of the imaging system. The higher the spatial frequency bandwidth of the system, the smaller the diffraction-limited spot size will be.

In contrast to 2D spatial imaging methods, swept-wavelength interferometry (SWI) is a one-dimensional, temporal measurement method. In SWI, the quantity analogous to the diffraction limit in a spatial imaging system is the Fourier transform-limited resolution, which is inversely proportional, not to the spatial frequency bandwidth of the system, but to the temporal bandwidth of the swept source. Here, a terminological confusion first presents itself. In SWI, the transform-limited resolution of the SWI system is a measure of the resolvability of any single delay time, and not necessarily a measure of the resolvability of two neighboring delay times (although, of course, these two measures are related). In both SWI and in 2D spatial imaging systems, however, the word "resolution," used on its own, refers to the distinguishability of two neighboring delay times or point sources.

The most common standard for the minimum resolvable distance between two incoherent point sources is the Rayleigh resolution criterion. In the familiar example of a diffraction-limited imaging system with a circular pupil function, two point sources are Rayleigh resolved when the first null of the Airy intensity pattern resulting from one point source falls at the center of the Airy pattern emerging from the second [43]. In a SWI system, the equivalent criterion is that two reflectors are separated from each other by a time delay approximately equal to twice the transform-limited resolution of the system[1]. Because of the parallel between spatial and temporal resolution criteria, I will refer to any reflectors that meet the delay time separation requirement as being Rayleigh resolved.

---

[1] If the amplitude of the swept source is constant as a function of optical frequency, then the exact separation requirement is given by the product of the transform-limited resolution and the spacing between the maximum and first minimum of the sinc function, i.e. roughly 1.429 times the transform-limited resolution.

In 2012, Candès and Fernandez-Granda proved that any point sources (or in the case of SWI, reflectors separated by a time delay) that meet the Rayleigh resolution criterion may be superresolved with precision limited only by signal-to-noise ratio (SNR) [44]. Given infinite SNR, any properly separated point sources or delay times may be superresolved with infinite precision! Put differently, the diffraction limit (or transform limit) of a measurement or imaging system may be exceeded, to a potentially infinite extent, provided only that the Rayleigh resolution criterion is met.

If the Rayleigh resolution limit itself is to be exceeded, two approaches are available. The first approach may be generally described as bandwidth extrapolation [43]. Given a data set or an image in which point sources do not meet the Rayleigh criterion, point sources may be superresolved using a variety of computational techniques [39] [40] [41] [42]. Unfortunately, all of these methods require very high SNR in order to have a chance of success, and their practical utility has therefore been limited [43].

A second approach has been tremendously successful, however. It is exemplified in a variety of forms by the superresolved fluorescence microscopy methods. All of these methods work by combining a series of superresolved images in which point sources are Rayleigh resolved and only the *diffraction limit* is exceeded, into a final image in which point sources are not Rayleigh resolved and the *resolution limit* is exceeded. Unfortunately, for SWI, there currently exists no rigorous method for suppressing the reflection from one or the other of a pair of reflectors which are not Rayleigh resolved, and consequently, this second approach is unavailable. The study of superresolution for SWI data must therefore, at least for now, be restricted to the following question: For any two reflectors that are Rayleigh-resolved, by how much can the transform-limited resolution of the SWI system be exceeded, both in precision and in accuracy, and why? To answer this question, the field of frequency estimation stands almost ready-made.

1.3 Introduction to Frequency Estimation

Frequency estimation is a rich and well-developed field, dating back to at least 1974, when Rife and Boorstyn presented a maximum-likelihood method for estimating the parameters of a complex sinusoid from discretely sampled, noisy data [45]. Frequency estimation is a type of spectral analysis, specifically, a type of parametric spectral analysis, which concerns itself with estimating the frequency components of a signal composed of one or more complex exponentials [46]. In almost all cases, the goal of the estimation process is to determine, with resolution finer than the bandlimited (i.e. transform-limited) resolution of the data set, the exact frequencies present in a given signal. For SWI data, the parameters to be estimated with resolution finer than the transform-limit are delay times; and by using frequency estimation methods to search for these delay times, SWI measurements may be superresolved.

Frequency estimation methods can be broadly divided into two classes: single-frequency estimation methods (applied to signals containing only one frequency component), and multiple-frequency estimation methods (applied to signals composed of a sum of complex exponentials). For the considerably simpler problem of single-frequency estimation, a great variety of methods and applications have been proposed and analyzed. In addition to the maximum-likelihood method presented by Rife and Boorstyn, these methods include a linear regression approach [47] [48], autocorrelation methods [49] [50], the well-known parabolic estimator [10], and many others. In the more difficult case of multiple-frequency estimation, the best-known approaches include the Nonlinear Least Squares estimator, the Yule-Walker auto-regression method, and the Pisarenko, MUSIC (MUtiple SIgnal Classification), and ESPRIT (Estimation of Signal Parameters via Rotational Invariance Techniques) estimators [46].

From among the many available frequency estimation methods, I have selected two multiple-frequency methods, Nonlinear Least Squares and ESPRIT, and two single-frequency methods, a linear regression method and a variant of the parabolic estimator, and compared their performance in superresolving SWI measurements. The justifications for selecting these particular estimators will be discussed in Chapter 2. Here, it is important to note that the size and richness of the frequency estimation literature is a consequence of the unique suitability of individual estimation methods to certain types of estimation problems. No universal "best estimator" exists—rather, the choice of any one estimator is a compromise among competing needs for accuracy, precision, and speed in any given estimation problem.

1.4 Thesis Outline

The remainder of this thesis is organized into four sections. The first section, contained in Chapter 2, is an examination of how frequency estimation methods may be used to superresolve SWI data. Using a numerical model, I quantify the fundamental limits, both in uncertainty and precision, of four methods for superresolving SWI measurements, and examine the experimental conditions under which each method is appropriate.

The next section, Chapter 3, is an investigation of the experimental limits of SWI. I analyze how six potential sources of systematic error—non-Gaussian noise, spurious delay times, laser power fluctuation, dispersion mismatch, temperature drift, and laser sweep nonlinearity—can prevent superresolved SWI measurements from reaching fundamental uncertainty limits. I also quantify the extent to which each of the latter four error sources must be controlled in order for superresolved SWI to achieve measurement accuracy equal to limiting measurement uncertainty. Finally, I present an experimental demonstration of the accuracy of an SWI system, showing superresolved accuracy well below the system's transform-limited resolution across a series of measured distances spanning three times the system's transform-limited resolution.

Chapter 4 is an exploration of how superresolved SWI may be time-multiplexed and used for the characterization of optical surfaces. First, I present an analysis of the system design considerations specific to a time-multiplexed, superresolved SWI system. I then describe the calibration requirements for such a system. Next, I describe the design of an 8-channel, time-multiplexed SWI system and lay out the calibration procedure for this system. After describing the development of an algorithm for surface reconstruction from an array of measured delay times, I present and analyze the experimental results of the measurements for two surfaces, a cylindrical lens and a coin, of low-order rotational symmetry.

Finally, in Chapter 5, I summarize the work contained in this thesis and conclude with a brief discussion of potential future developments for superresolved SWI.

Chapter 2

Fundamental Limits of Superresolved Swept-Wavelength Interferometry

In chapter two, I examine the limits of uncertainty and precision for superresolved swept-wavelength interferometry (SWI) measurements. I begin by developing mathematical and numerical models of an ideal SWI system. I then use these models to evaluate four methods of superresolving SWI distance measurements: Local Linear Regression (LLR), ESPRIT (Estimation of Signal Parameters via Rotational Invariance Techniques), Nonlinear Least Squares (NLS), and Candan's estimator. I first examine the uncertainty limits of SWI measurements for targets containing a single reflective surface and for those containing multiple reflective surfaces. Next, I compare the precision, or noise tolerance, of these four methods. Finally, I conclude with an analysis of root-mean-square error for each superresolution method and a discussion of the conditions under which these superresolution methods are appropriate.

2.1 Fundamentals of Swept-Wavelength Interferometry

I begin with a brief overview of the fundamentals of swept-wavelength interferometry. This subject has previously been analyzed in detail [51], so here I provide the concepts and notation that are the foundation for the work described later in this thesis.

Figure 2.1 shows the basic structure of a fiber-optic SWI. At the heart of the system is a tunable laser that sweeps across a continuous band of wavelengths. A fiber-optic coupler splits the output of this tunable laser into two separate arms, a reference arm and a sample arm, each with a different optical path length. Although the coupling ratio may take on any value, for simplicity, I assume here that it is 50:50.

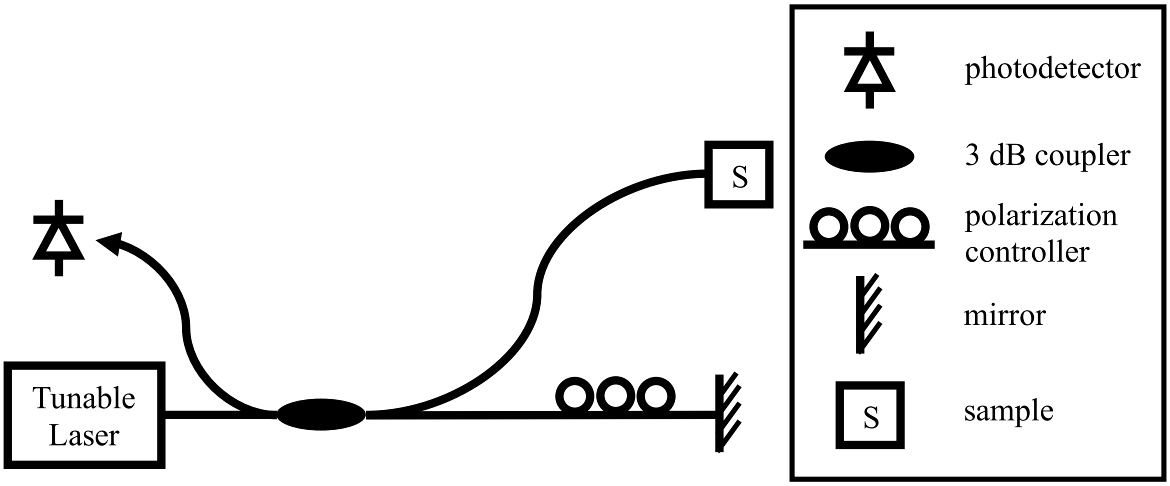

Figure 2.1 System diagram for a simplified swept-wavelength interferometer.

Mathematically, the output of the tunable laser can be represented by

$$\boldsymbol{E}(\nu[t]) = E(\nu[t])e^{2\pi j\nu[t]t}\widehat{\boldsymbol{Q}}\,. \tag{2.1}$$

The output electric field $\boldsymbol{E}$ is a function of the laser's instantaneous optical frequency ν, sampled at lab time t. Both the amplitude and phase of $\boldsymbol{E}$ are functions of optical frequency, while the polarization, given by unit vector $\widehat{\boldsymbol{Q}}$, is assumed to be constant throughout the laser sweep.

At the photodetector, the detected intensity U is given by

$$U(\nu[t]) = |\,\boldsymbol{E}(\nu[t-\tau_R]) + \boldsymbol{E}(\nu[t-\tau_S])\,|^2\,. \tag{2.2}$$

Variables τ_R and τ_S represent the group delay times of the signals in the reference and sample arms, respectively. After dropping a constant phase offset and assuming $\nu[t-\tau_1] \approx \nu[t-\tau_2]$, Equation (2.2) may be rewritten as

$$U(\nu[t]) = 2I(\nu[t])\{1 + \cos(2\pi\nu[t]\tau_0)\}\,, \tag{2.3}$$

where the differential delay time τ_0 is equal to $\tau_S - \tau_R$, the difference in group delay times between the sample and reference arms. The assumption that $\nu[t - \tau_1]$ is equal to $\nu[t - \tau_2]$ is an expression of the slow tuning approximation [52]. Qualitatively, this approximation assumes that the difference in group delays between the reference and sample arms is small enough that the optical frequencies being recombined at the coupler are the same.

To simplify this initial analysis, I assume that the sample arm of the SWI system contains only one reflective surface and therefore only one delay time τ_R. In experiments in which this is in fact the case, the number of fringes, i.e. periods of the cosine function in (2.3), across the laser sweep bandwidth can be counted to determine the differential delay time τ_0. This counting method is used, for example, in frequency scanning interferometry [53] [54] [55] [56] [57]. However, when the sample contains many reflective surfaces, the signal collected at the photodetector will be a superposition of many cosine terms, corresponding to the many differential delay times between sample and reference arms. Additionally, the collected signal will contain a series of cross-terms corresponding to every possible combination of delay time differences in the SWI system. In this more complicated case, the many differential delay times may be obtained by taking the Fourier transform of the collected signal.

Returning to the simple case in which the sample arm contains only one reflective surface, the discrete Fourier transform (DFT) of the collected signal is given by

$$\widetilde{U}[\tau] = \Im\{I[\nu]\} * \{2\delta(0) + \delta[\tau - \tau_0] + \delta[\tau + \tau_0]\}\,. \tag{2.4}$$

The signal $\widetilde{U}$, now a function of delay time τ, contains peaks centered at $\tau = \pm\tau_0$ in the positive and negative sidebands. The width and shape of these peaks is given by the Fourier transform of the profile of the laser's output intensity I as it sweeps across optical frequencies. (Note that any detector nonlinearity may be also be represented in the expression $I[\nu]$.)

If output power is constant over the laser sweep, and the photodetector is perfectly linear, then the laser's output intensity is given by

$$I[\nu] = \sigma E_0^2 \operatorname{rect}\left[\frac{\nu - \nu_c - {}^{B}\!/_{2}}{B}\right], \tag{2.5}$$

where E_0represents a constant electric field amplitude, σ is a constant representing detector responsivity, and ν_c is the center frequency of the laser sweep bandwidth B. In this case, the discrete Fourier transform of the detected signal is given by

$$\begin{aligned}\widetilde{U}[\tau] = \sigma E_0^2 B\{\, &2\operatorname{sinc}[B\tau] + \operatorname{sinc}(B[\tau - \tau_0]) \\ &+ \operatorname{sinc}(B[\tau + \tau_0])\,\}\, e^{-j2\pi\left(\nu_c + \frac{B}{2}\right)[\tau]}\,.\end{aligned} \tag{2.6}$$

In general, spacing between samples in the delay time domain—or DFT bin size—is equal to the inverse of laser sweep bandwidth B. The details of setting and maintaining this spacing will be discussed in section Section 3.1.6. In this chapter, I assume that DFT bin size, represented by variable s_τ, is perfectly constant and exactly equal to B^{-1}. Given these assumptions, Equation (2.6) may be rewritten as a function of a discrete counting variable m, yielding

$$\begin{aligned}\widetilde{U}[m] = \sigma E_0^2 B\{\, &2\operatorname{sinc}[Bms_\tau] + \operatorname{sinc}(B[ms_\tau - \tau_0]) \\ &+ \operatorname{sinc}(B[ms_\tau + \tau_0])\,\}\, e^{-j2\pi\left(\nu_c + \frac{B}{2}\right)ms_\tau}, \\ m = \Big\{-\frac{M}{2}, &-\frac{M}{2} + 1, \dots, \frac{M}{2} - 1\Big\},\end{aligned} \tag{2.7}$$

where M is the total number of samples. Explicitly noting the discretization of U will simplify the later discussion of superresolving SWI measurements.

2.2 Superresolution using Frequency Estimation Methods

Because the differential delay time τ is not a discrete variable, but a physical quantity, it may take on an intinite number of potential values. It is therefore extremely unlikely that any given delay time will be equal to an integer multiple of DFT bins. Instead, exact delay times will typically be centered some fraction δm_i of the way between sample points. For a sample containing i reflectors, the exact differential delay time corresponding to the i^{th} reflector is given by

$$\tau_i = (m_i + \delta m_i)s_\tau\,. \tag{2.8}$$

Indices m_i are the highest amplitude points in each of the delay time peaks. The Fourier transform-limited measure of each delay time τ_i is given by the product of index m_i and DFT bin size s_τ. Superresolution is the process estimating delay times with resolution finer than the Fourier transform limit, either through a direct estimate of the fraction δm_i, or through some other method.

2.2.1 Overview of numerical model

In practice, temperature and pressure related fluctuations in the atmosphere, the target, and the SWI system itself typically set experimental limits on the accuracy and precision of any SWI measurement system [53] [58]. To avoid these limitations and examine the fundamental limits of superresolved SWI, I use data that has been generated numerically, rather than experimentally. This approach is particularly advantageous in the evaluation of uncertainty limits—results may be compared with the parameters of a known model, rather than with secondary experimental measurements which are themselves subject to environmental instability.

Data was generated according to the specifics of the system shown in Figure 2.2. This model is very similar to the experimental system described in [33] and identical to the system used for experiments in Chapter 3. In the measurement arm of the interferometer, two reflectors are located approximately 50% of the way through the unambiguous range of the system. The tunable laser sweeps from 1500 nm to 1570 nm, resulting in a sweep bandwidth of 8.9 THz. A trigger interferometer with a 20 m path length mismatch between the two arms sets both the sample spacing in optical frequency (10 MHz) and the total number of samples per laser sweep (891,103). The laser's tuning rate is assumed to be slow enough that the trigger interferometer can perfectly compensate for laser sweep nonlinearity, i.e. second and higher order sweep rate nonlinearities can be neglected [52].

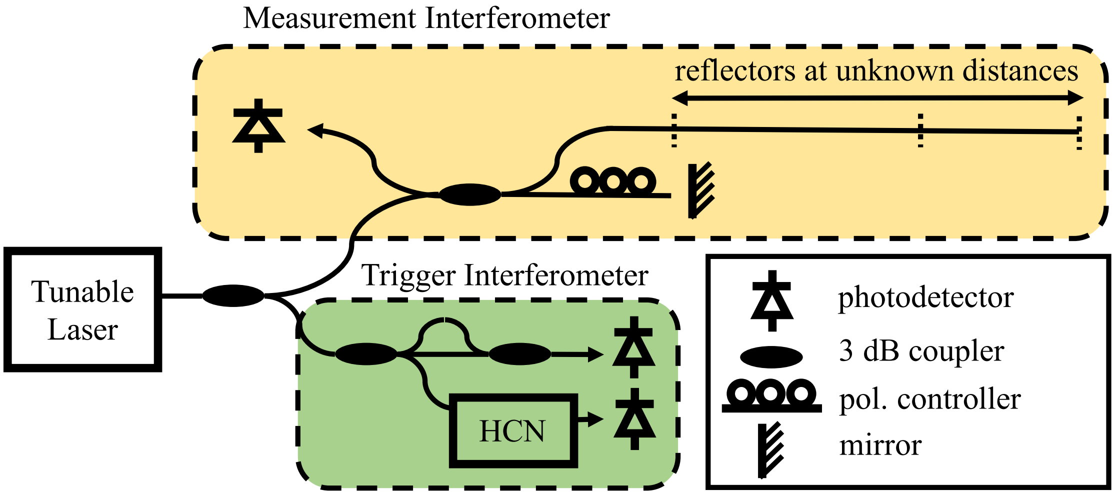

Figure 2.2 System diagram of a fiber-based SWI used as the model for numerical experiments. The Michelson geometry of the measurement interferometer enables the measurement of multiple reflective surfaces. The trigger interferometer consists of a Mach-Zehnder interferometer and a hydrogen cyanide (HCN) gas reference cell.

Mathematically, the data corresponding to a single laser sweep takes the following form:

$$U(\nu[t]) = 2 + \cos(2\pi\nu[t]\tau_a) + \cos(2\pi\nu[t]\tau_b) + Z[t]\,. \tag{2.9}$$

The signal U, sampled at times t, is a function of the instantaneous laser frequency ν. This signal consists of a DC offset term, two oscillatory terms created by the two reflectors in the measurement arm of the interferometer, and an additive noise term *Z[t]*. Note that because this model contains two reflectors, the full expression for the signal *U* would also contain a cross term; however, because this term would be lower in amplitude than the terms of interest and very near DC, its impact on the terms of interest is negligible. For the sake of simplicity, I have omitted it. Rewriting Equation (2.9) as a function of discrete sampling variable m gives

$$U[m] = 2 + \cos(2\pi\tau_a[\nu_0 - \delta\nu \cdot m]) + \cos(2\pi\tau_b[\nu_0 - \delta\nu \cdot m]) + Z[m]\,, \qquad (2.10)$$

$$m = \{0,1,\ldots,M-1\}\,,$$

where variable $\delta\nu$ denotes optical frequency spacing between samples, and variable ν_0 represents the optical frequency at the start of the laser sweep.

Delay times τ_i to each of the two reflectors correspond to path length mismatches between arms of the measurement interferometer. Physical path length mismatches are obtained by multiplying delay times by half the speed of light. Zero-mean Gaussian noise *Z[t]* is added to the signal by drawing values from a normal distribution whose variance is equal to noise power. In Figure 2.3a, a portion of the signal is plotted against laser wavelength λ. The DFT of this signal, shown in Figure 2.3b, contains two peaks, centered at delay times τ_a and τ_b. A close-up view of the second peak, shown in Figure 2.3c, reveals that delay time τ_b is located between sample points, approximately in the center of a DFT bin. (The fastidious reader may notice that the peaks in Figure 2.3b are not located 50% of the way through the unambiguous range of the numerical model described earlier, but are in fact much closer to the DC term. This discrepancy occurs only in Figure 2.3, and is included so that the two delay time peaks in Figure 2.3b will appear distinct.)

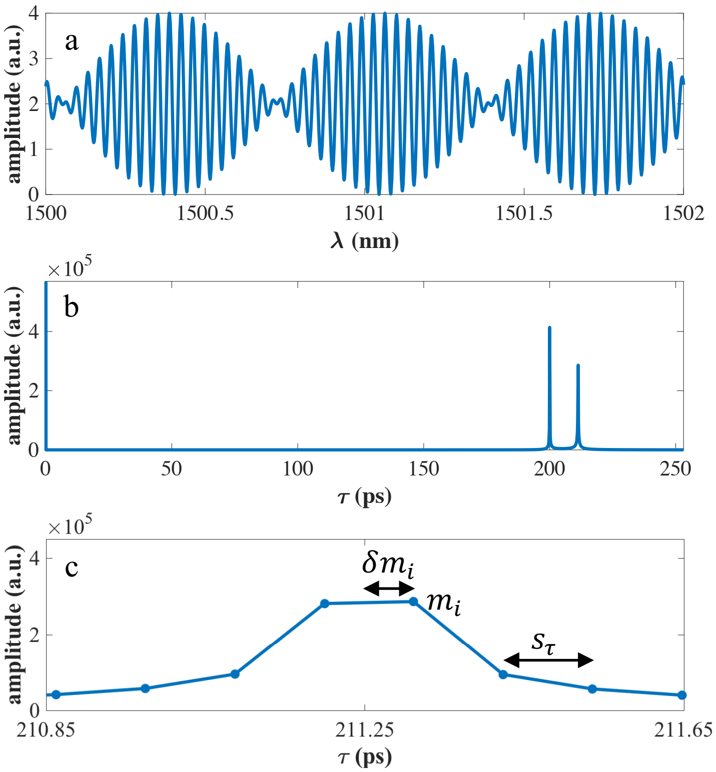

Figure 2.3 (a) Portion of measurement arm signal as a function of optical wavelength. Two reflectors in the measurement arm result in a signal composed of a beat frequency and an underlying carrier frequency. (b) Positive sideband of the DFT of the measurement signal contains a DC component as well as peaks corresponding to reflections from two surfaces. (c) Time delay to the second reflector is between sample points.

Here, I compare four estimators capable of superresolving SWI measurements. The first two, Estimation of Signal Parameters via Rotational Invariance Techniques (ESPRIT) [59] and Nonlinear Least Squares (NLS) [60] are well-known and well-characterized methods from the frequency estimation literature. Here, I apply them to SWI data, using them to estimate delay times instead of frequencies. The third estimator was developed specifically for making superresolved OFDR measurements [33], but unlike ESPRIT and NLS, its statistical properties are unknown. Here I refer to this method as Local Linear Regression (LLR) in order to disambiguate the estimation method itself from the entire experimental process the authors of [33] call Precision Ranging. Finally, I examine the performance of Candan's estimator, a relatively recent contribution to the field of frequency estimation [61]. Strictly speaking, Candan's estimator belongs to the class of parametric single frequency estimators. However, it has many desirable properties, and, given appropriate conditions, may be successfully applied to data containing multiple delay times.

2.2.2 Nonlinear Least Squares

For signals composed only of a summation of complex exponentials and corrupted only by white Gaussian noise, NLS is the maximum likelihood estimator [60] [62]. As such, it is consistent, asymptotically efficient, and asymptotically unbiased [63]. Even in the presence of colored noise, NLS estimates are asymptotically unbiased [64]. The NLS estimation method seeks to minimize the function

$$f(\omega, \alpha, \varphi) = \sum_{m=1}^{M} \left| U[m] - \sum_{i=1}^{k} \alpha_i e^{j(\omega_i m + \varphi_i)} \right|^2 , \tag{2.11}$$

where $U[m]$ is the sampled signal, and parameters ω, α, and φ represent the angular frequency, amplitude, and phase of the i^{th} component of the sum of complex exponentials. For SWI data, the frequencies ω_i are give by

$$\omega_i = 2\pi\delta\nu\tau_i , \tag{2.12}$$

where $\delta\nu$ is the spacing between samples in optical frequency, and τ_i is an individual delay time.

For SWI problems, it is generally not the amplitudes and phases, but the delay times τ_i, and therefore the angular frequency components ω_i, that are of interest. This is true for the majority of frequency estimation problems, although in most cases, the sampled signal $U[m]$ is a function of temporal frequency, not of delay time, as it is in the case of SWI data. The NLS method reduces the search for frequency, amplitude, and phase to a search for frequency alone by maximizing the value of merit function Q as a function of the angular frequency components ω_i. For any given values of the frequency components, the merit function Q is given by

$$Q = \bar{U}^* \bar{\bar{B}} \left(\bar{\bar{B}}^* \bar{\bar{B}} \right) \bar{\bar{B}}^* \bar{U} \, . \tag{2.13}$$

The data vector $\bar{U}$, given explicitly by

$$\bar{U} = \begin{bmatrix} U[1] \\ \vdots \\ U[M] \end{bmatrix}, \tag{2.14}$$

is a column vector containing the data points in the sampled signal $U[m]$. Matrix $\bar{\bar{B}}$, given by

$$\bar{\bar{B}} = \begin{bmatrix} e^{j\omega_1} & \cdots & e^{j\omega_k} \\ \vdots & \ddots & \vdots \\ e^{jM\omega_1} & \cdots & e^{jM\omega_k} \end{bmatrix}, \tag{2.15}$$

is a function of frequency components ω_i.

Because NLS is a parametric method, the number of reflectors contributing to the SWI data must be known in advance. And unlike LLR, ESPRIT, and Candan’s estimator, NLS is an optimization method, dependent on the quality of the initial guesses used to seed the optimization process. The optimization search space contains many local maxima, and in general, the quality of initial guesses required for convergence to the global maximum is unknown [60]. However, for the model used here, containing only two reflectors, I found that the search space is convex within 1 DFT bin of the global maximum. This is shown in Figure 2.4.

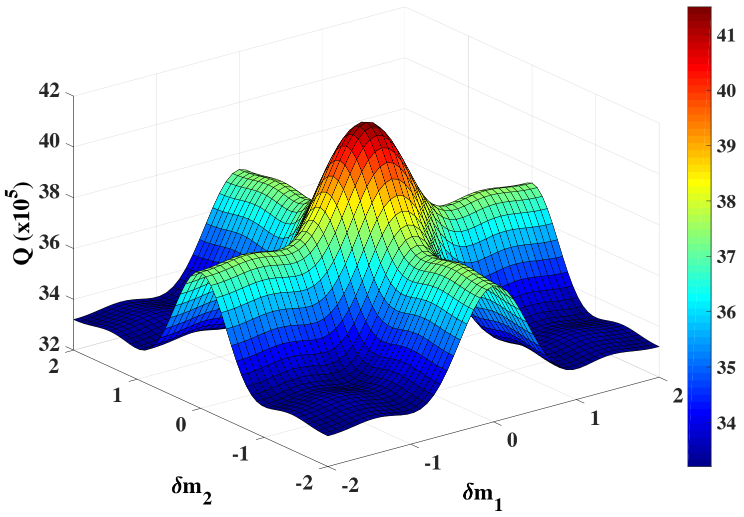

Figure 2.4 NLS search space for a signal containing two reflection times. The merit function Q *is determined by the spacing* δm *between true delay times and delay time guesses.*

Interestingly, in the two-reflector case, the NLS search space reveals that superresolving delay times that are not Rayleigh resolved may be possible with an NLS search, were it somehow possible to seed the search process with sufficiently accurate initial guesses. This is illustrated in Figure 2.5. Figure 2.5a shows the search space for a signal containing two Rayleigh resolved delay times. The global maximum is at least one DFT bin from the nearest minima. By contrast, Figure 2.5b shows the search space for a signal containing two delay times separated by half a DFT bin—

roughly one-third of the Rayleigh resolved distance. In the latter case, the separation between the global maximum and the nearest minimum is reduced to less than a quarter of DFT bin.

Recalling the discussion in Section 1.2, Figure 2.5 also clearly illustrates the dramatic increase SNR that would be required to superresolve reflectors that are not Rayleigh resolved (Figure 2.5b) compared those that are (Figure 2.5a).

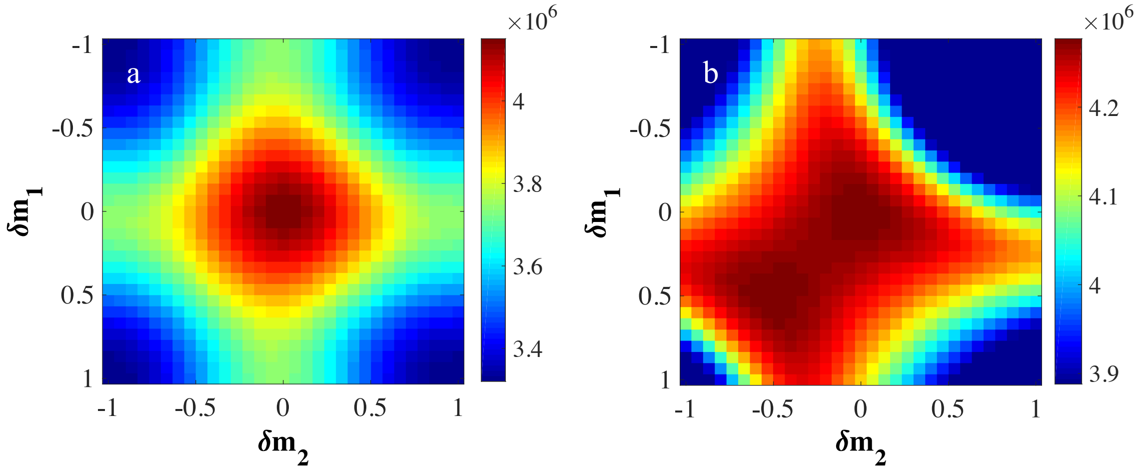

Figure 2.5 NLS search space for a signal containing two reflectors separated by (a) 5 DFT bins, and (b) 0.5 DFT bins.

To locate maxima in NLS search spaces, I used the Nelder-Mead simplex algorithm [65], implemented using MATLAB's *fminsearch* function [66]. However, the default value for the size of the simplex in the *fminsearch* function is too large for the search spaces generated by the NLS method. The default simplex encompasses an area of the search space containing, in addition to the global maximum, many other local maxima; and consequently, the search algorithm was likely to converge to a local, instead of global, maximum. To eliminate this problem, I reduced the initial size of the simplex to one 10,000th of its default value. Additionally, I reduced the step size tolerance exit criteria from its default value of 10^{-4} to 10^{-7} of DFT bin size. (Figure 2.6 illustrates the exit—or convergence—criteria for the Nelder-Mead simplex. The step size criterion is denoted as StepTolerance.)

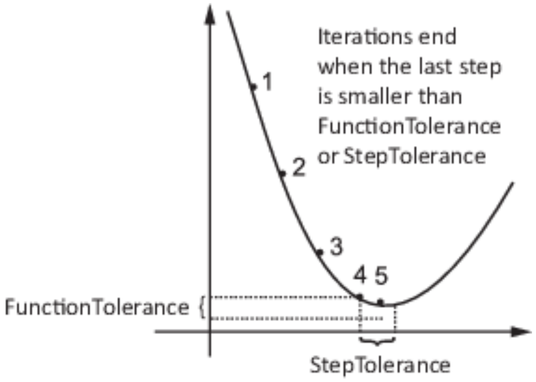

Figure 2.6 Convergence criteria for the Nelder-Mead simplex [67].

Further reducing the step size tolerance to below 10^{-7} of DFT bin size produces no additional improvement in the results of the NLS search, although it does continue to increase search time. This is shown in Figure 2.7. As the search exit criterion TolX decreases, the standard deviation of estimated delay times decreases as well, although this comes at the cost of increased search time. However, when the search exit criterion TolX drops below approximately 10^{-7} of DFT bin size, further reduction in exit criterion TolX ceases to correspond to reductions in the standard deviation of estimated delay times (although the search time continues to increase).

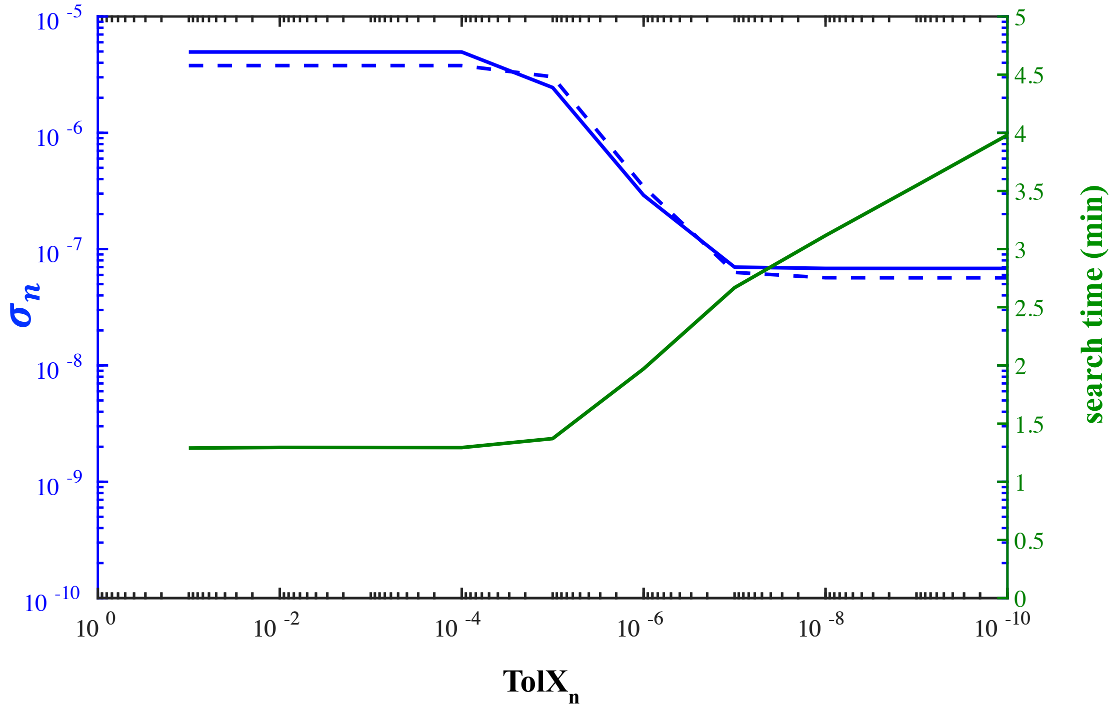

Figure 2.7 Standard deviation, normalized to DFT bin size, of estimated delay times to two reflectors (solid and dashed blue lines) is plotted on the left y-axis. Corresponding mean search time is plotted on the right y-axis. Exit criterion TolX$_n$ *is normalized to DFT bin size.*

This ceiling in performance quality is caused by the NLS search space itself reaching the numerical noise floor for double-precision floating point arithmetic. Figure 2.8 shows a very finely sampled image of the global peak in the NLS search space for two delay times. The asymptotic value of standard deviation estimates is 6.8x10^{-8} of a DFT bin (Figure 2.7). In Figure 2.8, two circles, one with a radius of one standard deviation 1σ and a second with a radius equal to two standard deviations, are plotted on the NLS search space. Within a single standard deviation, the change in the value of the search space due to numerical noise is greater than the change in the value due to variation in the two delay time guesses.

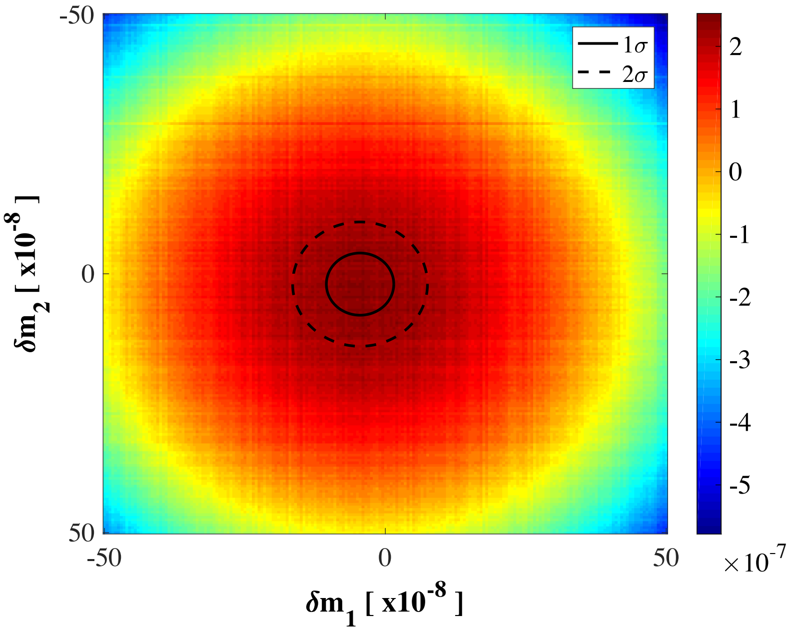

Figure 2.8 NLS search space for a signal containing two reflectors. The average value of the merit function across the portion of the search space plotted here has been subtracted from the all values of the merit function. The centers for the 1σ *and* 2σ *circles are offset by 4.5 x* 10^{-8} *in x and 2 x* 10^{-8} *in y. Both these offsets are within the* 1σ*standard deviation value.*

2.2.3 ESPRIT

ESPRIT was originally developed to solve direction-of-arrival problems [68], but it is also used to estimate the components of sampled signals containing multiple frequencies [69], and here I use it to estimate exact delay times to reflectors. It is a parametric estimation method, asymptotically unbiased and efficient, and generally known to give good results [68]. ESPRIT, along with the similar MUSIC estimator (MUtiple SIgnal Classification) [69] [70], is one of the premier methods from the class of subspace-based estimators [71], recommended by Stoica and Moses [46] as “the first choice in a frequency estimation application.” Its speed depends on both the number of data points in the sampled signal and on the order of the covariance matrix used in the estimation process [71]. However, because ESPRIT is non-iterative, it is, in general, faster than NLS. The mean execution time for ESPRIT, as well as for LLR, NLS, and Candan estimates, is listed in Table 2.1.

Table 2.1 Run times for single estimates. Averages of 5,220 iterations, run using Matlab on Intel® Core™ i7-3770K Processor.

Estimator	**LLR**	**Candan**	**ESPRIT**	**NLS**
Run Time (s)	0.13 ±0.01	0.64 ±0.01	26 ±1	151 ±16

ESPRIT, like NLS, assumes that the sampled signal is a sum of k complex exponentials; that is, the sampled signal $U[m]$ can be represented by

$$U[m] = \sum_{i=1}^{k} \alpha_i e^{j(\omega_i m + \varphi_i)} \, . \tag{2.16}$$

For SWI data, the angular frequency components ω_i are functions of delay times τ_i (Equation (2.12)). Given this assumption, ESPRIT estimates of frequencies ω_i are made in the following way. First, a covariance matrix $\bar{\bar{R}}$ of order A is computed, according to

$$\bar{\bar{R}} = \begin{bmatrix} R_U[0] & R_U[1] & \cdots & R_U[A-1] \\ R_U[1] & R_U[0] & \dots & R_U[A-2] \\ \vdots & \vdots & \ddots & \vdots \\ R_U[A-1] & R_U[A-2] & \cdots & R_U[0] \end{bmatrix} . \tag{2.17}$$

Each component $R_U[a]$ of the covariance matrix $\bar{\bar{R}}$ is given by the expected value of the product of the sampled signal and a delayed version of that same signal—i.e.

$$R_U[a] = E\big[U[m]U[m+a]\big], \ a = \{0,1,\dots,A-1\} \, . \tag{2.18}$$

The singular value decomposition of matrix $\bar{\bar{R}}$ gives

$$\bar{\bar{R}} = \bar{\bar{W}}\bar{\bar{\Lambda}}\bar{\bar{W}}^H \, , \tag{2.19}$$

where superscript H denotes the conjugate transpose. Selecting the first k columns of matrix $\bar{\bar{W}}$ (or the eigenvectors corresponding to the k largest eigenvalues in matrix $\bar{\bar{\Lambda}}$) gives:

$$\bar{\bar{W}}_s = \begin{bmatrix} W_{1,1} & \cdots & W_{A,1} \\ \vdots & \ddots & \vdots \\ W_{A,1} & \cdots & W_{A,k} \end{bmatrix}. \tag{2.20}$$

Matrix $\bar{\bar{W}}_s$ can then be partitioned into matrices $\bar{\bar{W}}_{s1}$ and $\bar{\bar{W}}_{s2}$, according to

$$\bar{\bar{W}}_s = \begin{bmatrix} \bar{\bar{W}}_{s1} \\ \text{last row} \end{bmatrix} = \begin{bmatrix} \text{first row} \\ \bar{\bar{W}}_{s2} \end{bmatrix}, \tag{2.21}$$

and the following equation may be solved for $\bar{\bar{\Psi}}$:

$$\bar{\bar{W}}_{s2} = \bar{\bar{W}}_{s1}\bar{\bar{\Psi}}\,. \tag{2.22}$$

The frequencies estimates $\widehat{\omega_i}$ are then given by

$$\widehat{\omega_i} = -\mathrm{Arg}(\lambda_i)\,, \tag{2.23}$$

where λ_i are the eigenvalues of matrix $\bar{\bar{\Psi}}$.

2.2.4 Local Linear Regression

LLR is the fastest of the three estimators, with a dramatically lower average execution time than either NLS or ESPRIT. This is largely because only a small portion of the signal is used to superresolve delay times of interest [33]. In fact, LLR can be considered a single-frequency estimation method [47], modified to estimate delay times for SWI signals containing returns from multiple reflectors. The estimation process, detailed in [33], is illustrated in Figure 2.9. It consists of extracting a series of points centered on a peak of interest in delay time (Figure 2.9a), multiplying the extracted points by a digital window function, shifting the extracted peak to baseband, taking the inverse Fourier transform of the extracted and windowed data points, and finally, fitting a line to the unwrapped phase of the resulting data (Figure 2.9b). The slope of the unwrapped phase is proportional to the fractional distance δm_i of the peak's center from the nearest sample point (Figure 2.9c). The linear relationship between phase slope in the optical frequency domain and peak shift in the delay time domain is a consequence of the Fourier shift theorem [43].

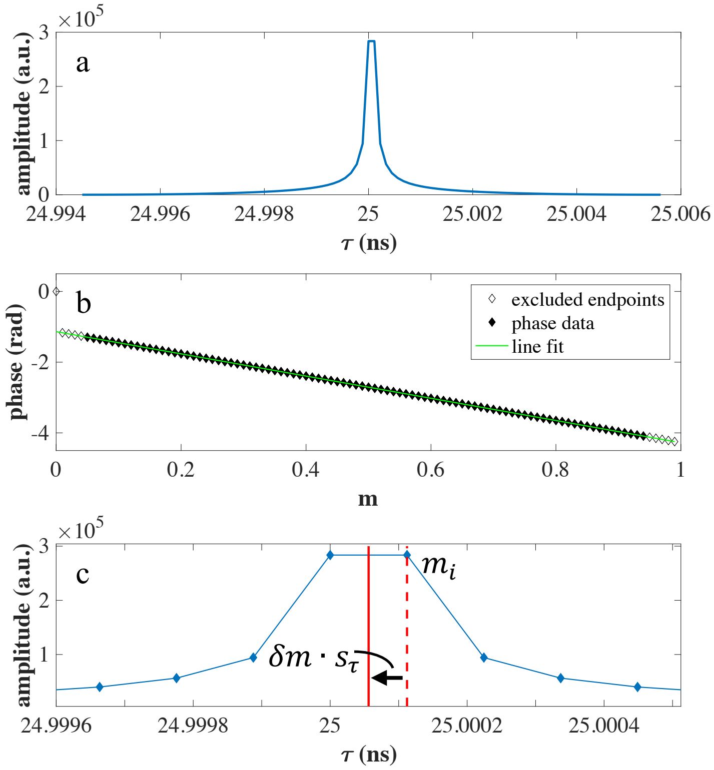

Figure 2.9 (a) One hundred data points, centered about a peak of interest in delay time, are extracted from the entire data set. (b) A line is fitted to the unwrapped phase of the inverse Fourier transform (IFT) of the extracted data points. Five points at each end of the phase data are excluded from the line fit. Before the IFT, the extracted points were multiplied by a Hanning window and shifted to baseband. (c) The fractional distance δm_i *between the peak's true center and the nearest sample point is proportional to the slope of the unwrapped phase.*

The DFT of an SWI signal containing returns from multiple reflectors contains multiple peaks in delay time. LLR relies on the assumption that the extracted points surrounding any peak contain information only about that peak, i.e. spectral leakage is negligible. This assumption is reasonable only if the peaks are sufficiently separated in delay time, meaning the optical path length between any two reflectors is sufficiently large. Consequently, the closer two peaks are in delay time, the fewer points surrounding any one peak may be extracted in the estimation process.

Even when spectral leakage is negligibly small or nonexistent, LLR estimates are biased. The magnitude of this bias depends on several things: the locations of reflectors in the unambiguous range of the system, the number of points included in the extraction step, the choice of window function, and the number of data points included in the line fit to the phase slope. For the case of a single reflector, Figure 2.10 illustrates how LLR bias depends on the fractional location of a delay time peak inside a DFT bin. As the position of the reflector is moved across one DFT bin, the difference between the reflector's true position (used to generate data) and the reflector's recovered position (obtained with an LLR estimate) varies unpredictably.

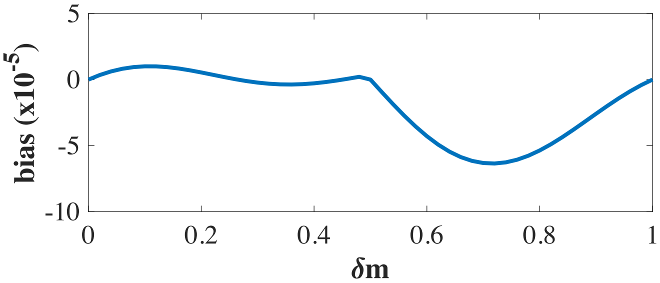

Figure 2.10 Bias, normalized to DFT bin size, in estimated delay time for a single reflector. These LLR estimates were made using a 100 point rectangular window.

In general, bias decreases as the number of points included in the extraction step increases. Applying window functions that decay smoothly to zero at their edges produces bias values that asymptotically approach 10^{-10} of DFT bin size. When peaks are separated in delay time by approximately 200 DFT bins or more, enough points may be included in the extraction step that LLR bias becomes inconsequential. Figure 2.11 shows the dependence of maximum LLR estimate bias on the number of extracted data points, the choice of window function, and the percentage of endpoints excluded from the line fit to phase slope.

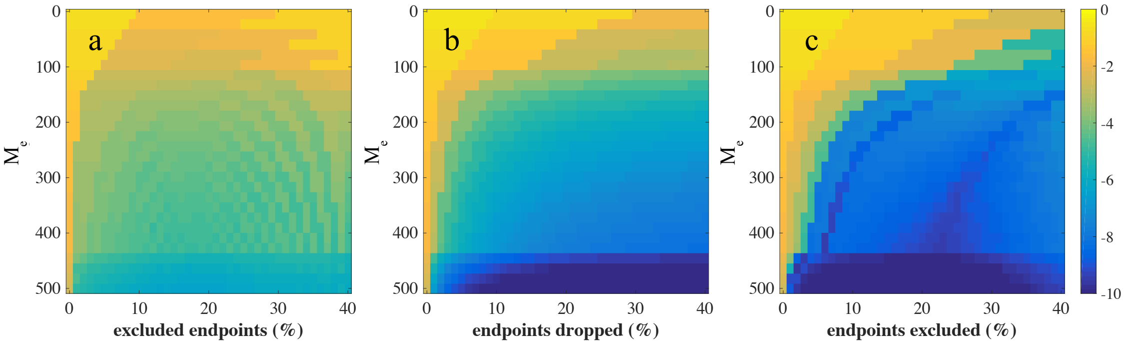

Figure 2.11 Maximum absolute bias, normalized to DFT bin size, of delay time estimates for a single reflector. For any window function, maximum bias depends on both the total number M_e *of extracted data points and on the percentage of endpoints excluded from each end the line fit to phase slope. Results are shown for a (a) rectangular window, (b) Hanning window, and (c) Chebyshev window.*

When a rectangular window is chosen (this is equivalent to leaving the data unwindowed), then the optimal percentage of endpoints to exclude from each end of the phase data is approximately 20% (Figure 2.11a). When the extracted data points are multiplied by a Hanning window, estimate bias decreases in proportion to the percentage of excluded endpoints, although the rate of decrease slows considerably after more than approximately 20% of endpoints are excluded (Figure 2.11b). When a Chebyshev window is applied, the optimal percentage of excluded endpoints varies depending on the number of extracted points (Figure 2.11c). In general, however, excluding approximately 20% of endpoints from the line fit produces good results.

2.2.5 Candan's estimator

Candan's estimator [72] [73] belongs to a small family of parametric, single-frequency estimators that use only three DFT data points to estimate the exact center of a peak in frequency (or in the case of SWI data, in delay time). The oldest and best known of these estimators is the parabolic interpolation method [10]. Other methods using three DFT points have been proposed by Quinn in 1994 [74] [75], MacLeod in 1998 [76], and Jacobsen in 2007 [77]. A similar estimation method using only two DFT points was proposed by Provencher in 2010 [78]. All these estimators produce biased estimates, with older estimators tending to suffer from greater bias than younger versions.

In 2011, Candan proposed a modification of Jacobsen's estimator that demonstrated a significant reduction in estimate bias over previous 3-point estimators [72]. Subsequent work showed that by including an additional bias correction step to the estimation process, estimate bias can be driven below 10^{-8} of one DFT bin [73]. Furthermore, by including a correction factor specific to any given window function, this negligible level of estimate bias may be maintained when data is multiplied by a window function before being Fourier transformed. The additional computational burden imposed by the second bias correction step increases execution time for the Candan estimator (Table 2.1), but for single-reflector data generated using the model described earlier, the maximum bias in delay time estimates is always below 10^{-10} of DFT bin size. For similarly rapid LLR estimates to achieve such low bias, around 500 points must be extracted from around any delay time peak, which reduces the usable unambiguous range of the SWI system (albeit by only a small fraction).

Candan's estimator makes a direct estimate of the DFT bin fraction δm_i separating the true center of a delay time peak from the nearest sample point m_i. In the first step of the estimation process, an estimate $\widehat{\delta_1 m_\imath}$ is made using the following formula:

$$\widehat{\delta_1 m_\imath} = c_M \text{Real}\left\{\frac{\widetilde{U}[m_i - 1] - \widetilde{U}[m_i + 1]}{2\widetilde{U}[m_i] - \widetilde{U}[m_i - 1] - \widetilde{U}[m_i + 1]}\right\}. \tag{2.24}$$

Signal $\widetilde{U}[m]$ is the DFT of signal $U[m]$, and the value of $\widetilde{U}[m_i]$ is given by the complex value of the highest-magnitude point, corresponding to delay time τ_i, in the transformed signal $\widetilde{U}[m]$. Points $\widetilde{U}[m_i - 1]$ and $\widetilde{U}[m_i + 1]$ are to the immediate left and right, respectively, of the highest-magnitude point $\widetilde{U}[m_i]$. The value of the correction factor c_M depends on the number of points *M* in the sampled signal and on the window function $w[m]$ multiplied by signal $U[m]$ before taking the discrete Fourier transform. It is calculated using

$$c_M = \frac{B_0^2}{A_1 B_0 + A_0 B_1}. \tag{2.25}$$

The coefficients A_0, A_1, B_0, and B_1 are given by

$$A_0 = \text{Imag}\left\{\sum_{m-0}^{M-1} w[m]e^{j2\pi mM} - \sum_{m-0}^{M-1} w[m]e^{-j2\pi mM}\right\}, \tag{2.26}$$

$$A_1 = \frac{j2\pi}{M}\sum_{m-0}^{M-1} mw[m]e^{j2\pi\frac{m}{M}} - \frac{j2\pi}{M}\sum_{m-0}^{M-1} mw[m]e^{-j2\pi\frac{m}{M}}, \tag{2.27}$$

$$B_0 = 2\sum_{m-0}^{M-1} w[m] - \sum_{m-0}^{M-1} w[m]e^{j2\pi mM} - \sum_{m-0}^{M-1} w[m]e^{-j2\pi mM}, \tag{2.28}$$

and

$$B_1 = \mathrm{Imag}\left\{\frac{j4\pi}{M}\sum_{m-0}^{M-1} mw[m] - \frac{j2\pi}{M}\sum_{m-0}^{M-1} mw[m]e^{j2\pi\frac{m}{M}} - \frac{j2\pi}{M}\sum_{m-0}^{M-1} mw[m]e^{-j2\pi\frac{m}{M}}\right\} \tag{2.29}$$

respectively.

In the second step of the Candan estimation process, the value $\widehat{\delta_1 m_\iota}$, estimated in the first step, is removed from the sampled signal $U[m]$, giving a modified signal $U_2[m]$, where

$$U_2[m] = U[m]e^{-j\frac{2\pi}{M}\widehat{\delta_1 m_\iota}m} \quad , m = \{0,1,\dots,M-1\}\,. \tag{2.30}$$

Then, a second value $\widehat{\delta_2 m_\iota}$ is estimated from the highest-magnitude point $\widetilde{U_2}[m_i]$ and its two neighboring points $U_2[m-1]$ and $U_2[m+1]$ in the DFT of signal $U_2[m]$, according to

$$\widehat{\delta_2 m_\iota} = c_M \mathrm{Real}\left\{\frac{\widetilde{U_2}[m_i-1] - \widetilde{U_2}[m_i+1]}{2\widetilde{U_2}[m_i] - \widetilde{U_2}[m_i-1] - \widetilde{U_2}[m_i+1]}\right\}. \tag{2.31}$$

Finally, the estimate $\widehat{\delta m_\iota}$ is given by the sum of the estimates $\widehat{\delta_2 m_\iota}$ and $\widehat{\delta_2 m_\iota}$ made in the first and second steps, i.e.

$$\widehat{\delta m_\iota} = \widehat{\delta_1 m_\iota} + \widehat{\delta_2 m_\iota}\,. \tag{2.32}$$

2.3 Uncertainty in Superresolved SWI Measurements

It is apparent from Equation (2.8) that the uncertainty of delay time measurements depends both on uncertainty in DFT bin size $u(s_\tau)$ and on uncertainty in superresolution, $u(\delta m_i)$. In general, uncertainty in DFT bin size depends on the method used to maintain sample spacing in optical frequency. Because tunable laser sweep rates are generally not linear, samples acquired at regular time intervals will be unevenly spaced in optical frequency [52]. Evenly spaced samples can be obtained in several ways, by resampling the signal data [79] [80], linearizing the laser sweep [81] [82], using a nonuniform discrete Fourier transform (NDFT) [83], or using a secondary interferometer to trigger sample acquisition. In each case, the method used to set sample spacing also sets a lower limit on uncertainty in DFT bin size. The system modeled here uses a trigger interferometer, and consequently, DFT bin size uncertainty is ultimately limited by the quality of the wavelength reference gas cell [33] [84].

For Fourier transform-limited SWI measurements, only DFT bin size uncertainty $u(s_\tau)$ contributes to total uncertainty in delay time measurements. However, for superresolved measurements, the process of estimating the fractional location $u(\delta m_i)$ of delay time within a DFT bin may also contribute uncertainty to the measurement. In general, unbiased estimation methods make no additional contribution to total uncertainty; in these cases, the value of $u(\delta m_i)$ is zero. However, estimators that converge to incorrect values of fractional location δm_i, that is, biased estimators, contribute additional uncertainty $u(\delta m_i)$ to the total uncertainty of delay time measurements.

For targets containing multiple reflective surfaces, quantities of interest are not typically the absolute delay times to each surface, but rather the differential delay times between target surfaces. Differential measurements reject common mode fluctuations such as temperature drift in the interferometer, resulting in significant improvements in measurement precision [33]. Here, I examine the two-reflector case, but these results are generalizable to targets containing any number of reflectors.

For two reflectors separated by delay time difference $\Delta\tau$, uncertainty in the measurement of $\Delta\tau$ is given by

$$u(\Delta\tau) = \left[\Delta\tau^2 \frac{u^2(s_\tau)}{s_\tau^2} + 2s_\tau^2 u^2(\delta m)\right]^{1/2} . \tag{2.33}$$

(The derivation of (2.33 assumes the variables $\Delta\tau$, s_τ, and δm are independent [85].) The details of establishing DFT bin size uncertainty $u(s_\tau)$ will be examined in detail in Section 3.1. In this chapter, I will use the calibration procedure described in [33] along with the manufacturer's specifications for a Wavelength References HCN gas reference cell to establish a lower limit on DFT bin size uncertainty.

2.3.1 Spectral leakage and bias for single-frequency estimators

To determine the contribution of estimator bias to overall uncertainty in differential delay time measurements, I begin by revisiting the topic of bias in both Candan and LLR estimates. Since both are single frequency estimators, applying them to data containing multiple delay times requires assuming spectral leakage is negligible. In general, the closer any two delay times are to each other, the more this assumption breaks down. For LLR estimates, this trend is illustrated in the numerical results plotted in Figure 2.12. One reflector is fixed at delay time τ_1, approximately halfway through the unambiguous range of the modeled SWI system. The delay time τ_2 to a second reflector is translated from 10 to 100 DFT bins of separation from delay time τ_1. The number of points extracted around each peak in delay time is equal to the number of DFT bins between the two peaks. As the delay time difference between the two peaks increases, the bias in estimates of both the delay time difference $\tau_2 - \tau_1$ and the individual delay times τ_1 and τ_2 decreases.

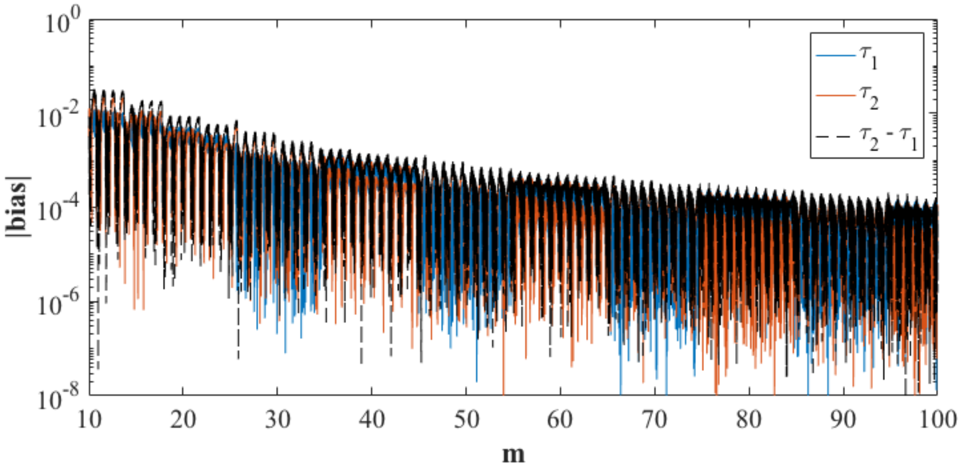

Figure 2.12 Absolute value of bias, normalized to DFT bin size, for LLR estimates of delay time for delay times τ_1, τ_2, *and the difference between them* $\tau_2 - \tau_1$. *The difference* $\tau_2 - \tau_1$ *increases through* m *DFT bins.*

2.3.2 Bias in LLR estimates of delay time differences

In the case of LLR, it is difficult to distinguish the effects of spectral leakage from the effects of estimator bias, as the level of bias for delay times in the two-reflector case (Figure 2.12) is comparable to the level of bias in delay time estimates in single-reflector data (Figure 2.11b).

To reduce the effects of spectral leakage, data may be multiplied by a window function before being Fourier transformed. This will have the general effect of broadening peaks in delay time and reducing their magnitude, while also reducing the magnitude of sidelobes (and thus reducing spectral leakage). Figure 2.13 shows that for LLR estimates of delay time difference $\tau_2 - \tau_1$, the magnitude of estimate bias is significantly reduced by applying a Hanning window to simulated data before taking the Fourier transform. However, applying a Hanning window to the entire data set, in addition to multiplying extracted data points by a Hanning window before taking the inverse Fourier transform, dramatically increases estimate bias.

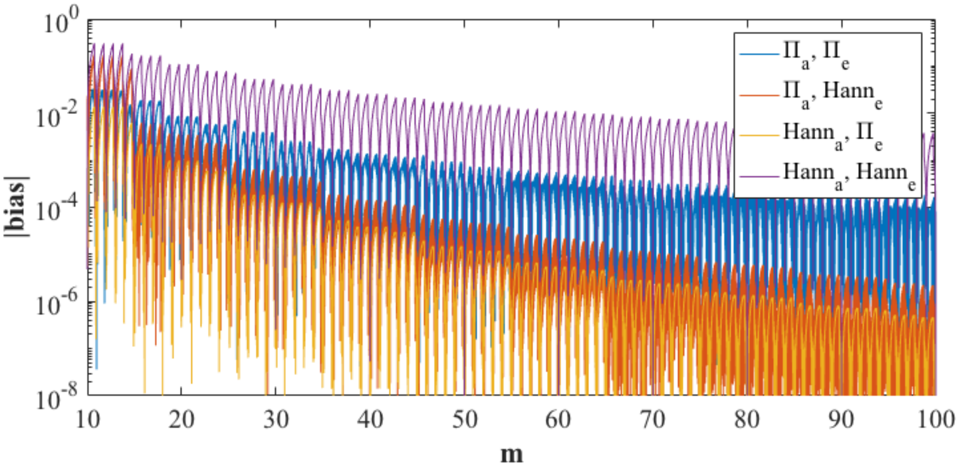

Figure 2.13 Effects of applying a rectangular window function to all data points before the Fourier transform and to extracted data points used for the LLR estimate (blue line); a rectangular window to all data points and a Hanning window to extracted data points (orange line); a Hanning window to all data points and a rectangular window to extracted data points (yellow line); and a Hanning window to all data points and then to extracted data points (purple line).

Consequently, when LLR is used to estimate delay times in multiple frequency data, it is best to modify the procedure originally described in [33]. Extracted points should not be multiplied by a window function; instead, the entire data set should be windowed before the initial Fourier transform. Figure 2.14 shows the magnitude of the bias in LLR estimates of delay time difference $\tau_2 - \tau_1$ when the entire data set has been multiplied by a rectangular (Π), Hanning, or Chebyshev window. The Chebyshev window suppresses sidelobe magnitude to 100 dB relative to the magnitude of the main lobe, and of the three windows, it is the most effective in reducing the effects of spectral leakage. However, both the Hanning and Chebyshev windows raise the noise floor in the delay time domain—this results in reduced estimate precision. Because this processing loss is larger for the Chebyshev window, the Hanning window represents an acceptable (and very common) compromise between sidelobe suppression and SNR loss. In Figure 2.14, a series of selected points shows the maximum bias for reflector separations between 10 and 100 DFT bins when the Hanning window is used.

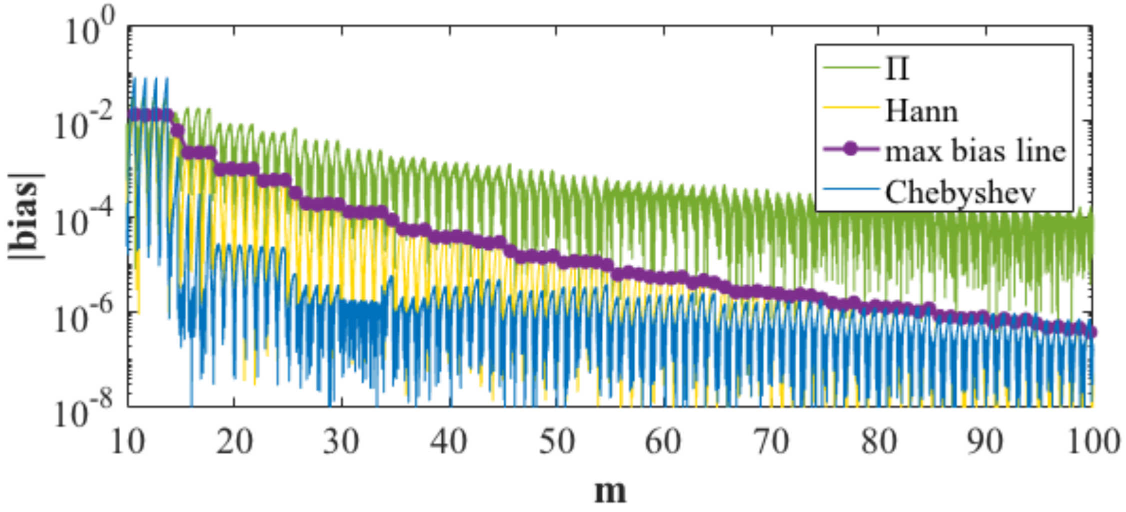

Figure 2.14 Bias in the estimate of delay time difference $\tau_2 - \tau_1$. *Before the Fourier transform, the entire data set was multiplied by a rect, Hann, or Chebyshev window.*

2.3.3 Bias in Candan estimates of delay time differences

2.3.3.1 Reflections of equal amplitude

In comparison to LLR estimates, estimates of delay time differences made using Candan's estimator clearly show the effects of spectral leakage. In single-reflector data generated using the model described in Section 2.2.1, bias is always below 10^{-10} of DFT bin size. By contrast, Figure 2.15 shows that bias in estimates of delay time difference $\tau_2 - \tau_1$ is considerably higher, approaching—even briefly exceeding—one DFT bin when reflector spacing is below five DFT bins. As reflector spacing increases, bias rapidly decreases, falling below 10^{-4} of DFT bin size when reflector spacing exceeds approximately fifteen DFT bins, and dropping below 10^{-6} of DFT bin size for reflector separations greater than about fifty DFT bins. For reflector separations greater than approximately five DFT bins, the power functions

$$|\mathrm{bias}|_{\mathrm{H}} = 3.5m^{-4.1} \tag{2.34}$$

and

$$|\mathrm{bias}|_{\mathrm{C}} = 1.2\times10^{-3}m^{-2.1} \tag{2.35}$$

predict, for estimates made using the Hanning and Chebyshev windows, respectively, the magnitude of maximum bias with high fidelity.

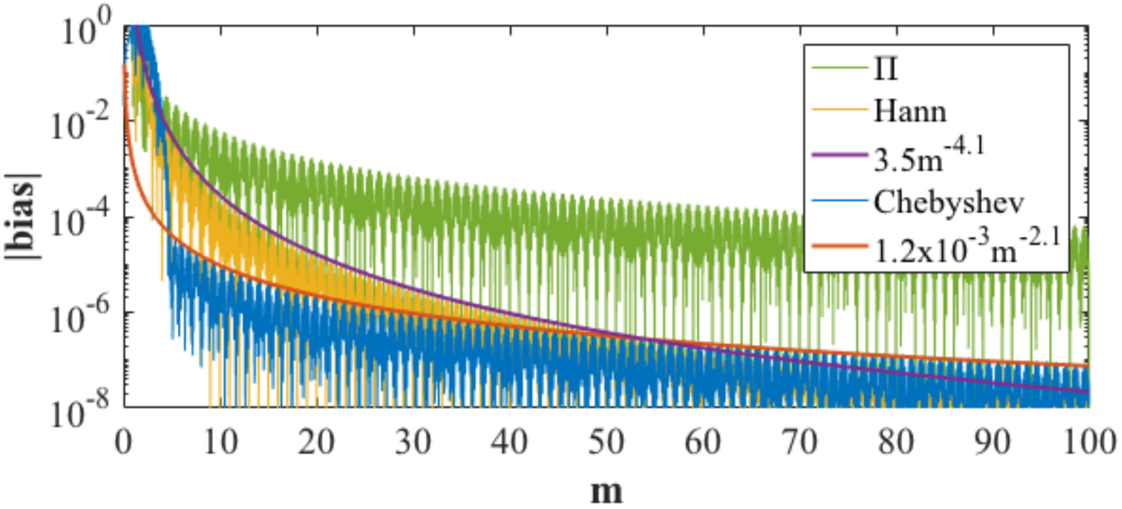

Figure 2.15 Magnitude of bias, normalized to DFT bin size, in Candan estimates of delay time difference $\tau_2 - \tau_1$. Before the Fourier transform, data was multipled by a rect, Hann, or Chebyshev window.

Just as in the case of LLR estimates, the Chebyshev window is more effective than the Hann window in mitigating the effects of spectral leakage between closely spaced reflectors. Because the Hanning window is likely to perform better under a broader range of conditions, I have used it for all the Candan estimates presented in the remainder of this dissertation. However, given sufficient SNR, the Chebyshev window may be better choice for Candan estimates when reflectors are separated by between 5 and 20 DFT bins.

2.3.3.2 Reflections of unequal amplitude

When two reflections have unequal amplitudes, bias in estimates of the delay time between the two reflections is increased in proportion to the difference between reflection amplitudes. While the higher magnitude peak is influenced to a lesser extent than is indicated in Figure 2.15, the lower magnitude peak is influenced to a greater extent. In fact, it is the magnitude difference between the peaks that determines the bias in estimates of differential delay times of two reflectors of unequal reflectivity. This effect is shown for a series of magnitude differences in Figure 2.16.

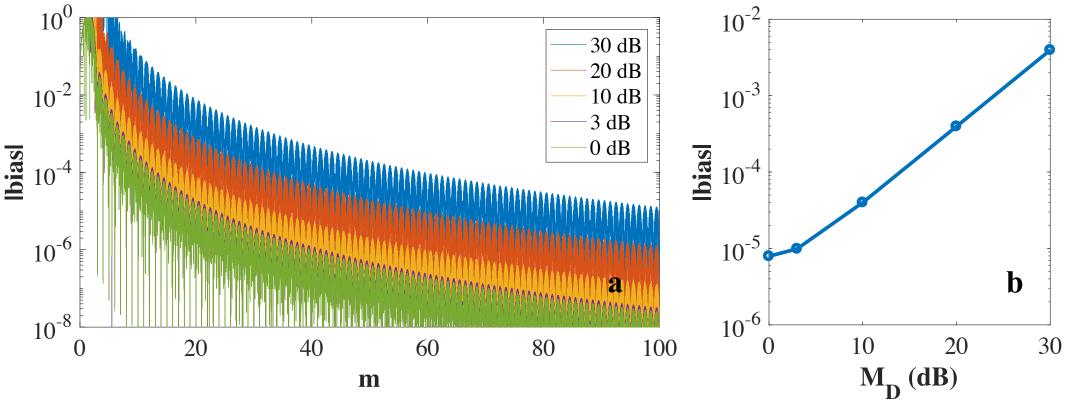

Figure 2.16 (a) Magnitude of bias, normalized to DFT bin size, in the estimated delay time between two reflectors separated by m *DFT bins. The legend gives the relative amplitude difference between the two reflectors. (b) Magnitude of bias, normalized to DFT bin size, of the estimated delay time difference between two reflectors separated by 20.5 DFT bins, and with relative amplitude difference* M_D.

2.3.4 Summary of uncertainty limits for superresolved SWI

Figure 2.17 summarizes uncertainty in estimates of time delay between two equal-amplitude reflectors. In general, as reflector spacing increases, uncertainty also increases, with the rate of increase dependent on uncertainty in delay time step size. In the system modeled here, delay time step size is 112 fs, the inverse of the 8.9 THz laser sweep bandwidth. Uncertainties in the wavelengths of HCN absorption lines determine uncertainty in delay time step size s_τ. Consequently, using a Wavelength References Hydrogen Cyanide gas reference cell with 0.08 pm and 0.15 pm uncertainty on R_{20} and P_{18} absorption lines, respectively, results in a 2σ uncertainty of 1.2 as in delay time step size. I assume a 2σ uncertainty of one fringe period in the trigger interferometer calibration.

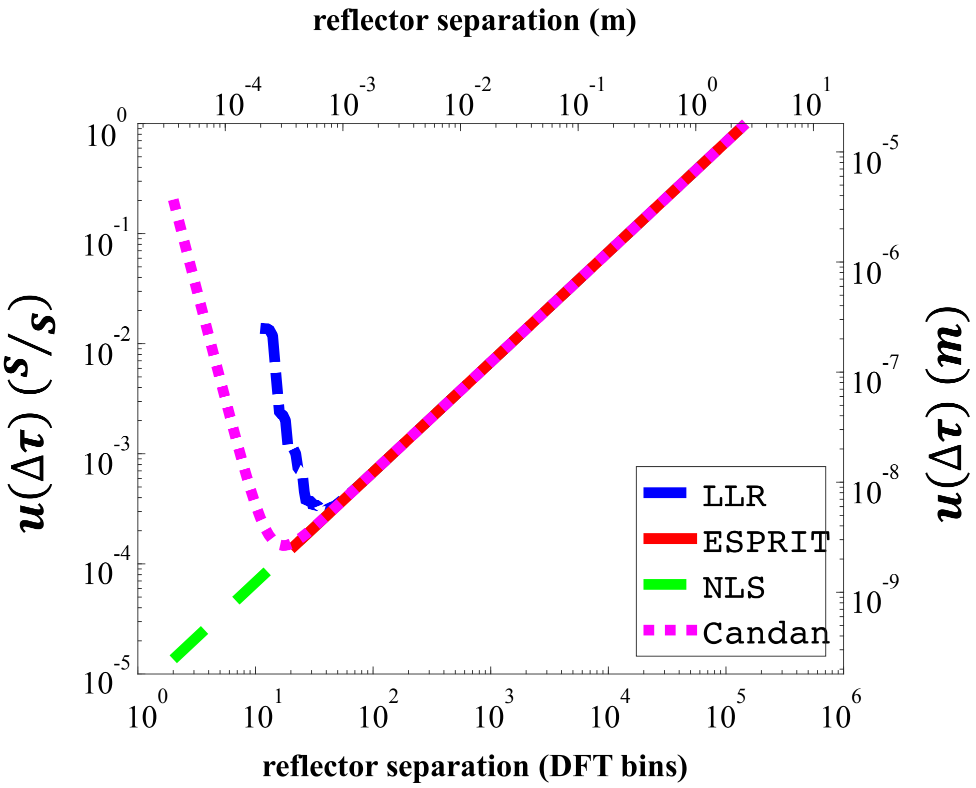

Figure 2.17 2σ uncertainty for distance measurement between reflectors separated by free space. The lower x-axis shows the separation between reflectors measured in DFT bins; the upper x-axis shows the same reflector separation measured in meters of free space. The left y-axis shows uncertainty normalized to the system's Fourier transform-limited resolution, while the right y-axis shows the corresponding distance value in free space. The highest value on the left axis is 1; when normalized uncertainty is equal to DFT bin size, superresolution no longer provides meaningful information.

When reflector spacing drops below approximately 20 DFT bins, ESPRIT estimates become unstable, with small changes in reflector positions causing widely varying errors in estimated delay times. Increasing the order of the covariance matrix enables estimates of delay times between more closely spaced reflectors, but also increases computation time for each estimate. For LLR estimates, when reflectors are separated by approximately 100 DFT bins or fewer, uncertainty $u(\delta m)$ from estimator bias becomes the dominate contributor to overall uncertainty $u(\Delta\tau)$

(Equation (2.33)). And although Candan estimates show lower bias than LLR estimates at equivalent reflector separations, for reflector separations below approximately 20 DFT bins, spectral leakage begins to contribute significantly to estimate bias and consequently degrade the overall estimate uncertainty.

In Figure 2.17, uncertainty $u(\delta m)$ from estimator bias is given by maximum estimate bias for both LLR and Candan estimators. For LLR, maximum estimate bias for any given reflector spacing was obtained by interpolating the maximum bias line from Figure 2.14. For Candan estimates, maximum bias was obtained from the exponential fit to the Hanning-windowed data shown in Figure 2.15.

For reflectors that are more widely spaced, by 100 DFT bins or more, the uncertainties of LLR, ESPRIT, NLS, and Candan estimates are nearly identical, and the computational speed of LLR makes it the preferred superresolution method. When reflector spacing is wide enough—in free space approximately 2.65 meters—uncertainty equals the size of a DFT bin. This places an upper limit on the useful range of superresolved SWI.

2.4 Precision of Superresolved SWI measurements

The precision of estimates of delay time difference is determined by estimator variance—that is, by the noise tolerance of the estimator used to establish any given delay time difference. Estimator variance is a statistical quantity, and each of the four estimators examined here—LLR, ESPRIT, NLS, and Candan's estimator—demonstrate varying degrees of success in estimating delay time differences from noisy data. Here, I compare the performance of each of these estimators across a range of signal-to-noise ratios (SNRs) and reflector separations.

2.4.1 Cramér-Rao bound

For any deterministic parameter, the Cramér-Rao bound (CRB) establishes the lowest possible variance for any unbiased estimator of that parameter [86] [87]. Consequently, the CRB gives the lowest variance, or highest precision, for estimates of delay times from noisy data. Unfortunately, for signals composed of a summation of complex exponentials, as is the case for the signal described by Equation (2.9), there is typically no analytical solution for the CRB [88]. However, if the signal's parameters are known, the CRB may be estimated, or, as I have done here, calculated, using the procedure described in [60].

Figure 2.18 shows the CRB for the signal $U(\nu[t]))$ across a wide range of reflector separations and SNRs. For data composed of reflections from two reflectors, the maximum precision for a measure of the delay time difference between reflectors may be several orders of magnitude below DFT bin size. This rather dramatic prediction has been corroborated by several experimental results reported in the literature [33] [21] [34], most notably in [33], in which a system operating with an estimated SNR of 90 dB [51] was used to measure the group refractive index and thickness of a fused silica plate with a reported 1σ precision of 5x10^{-5} of DFT bin size.

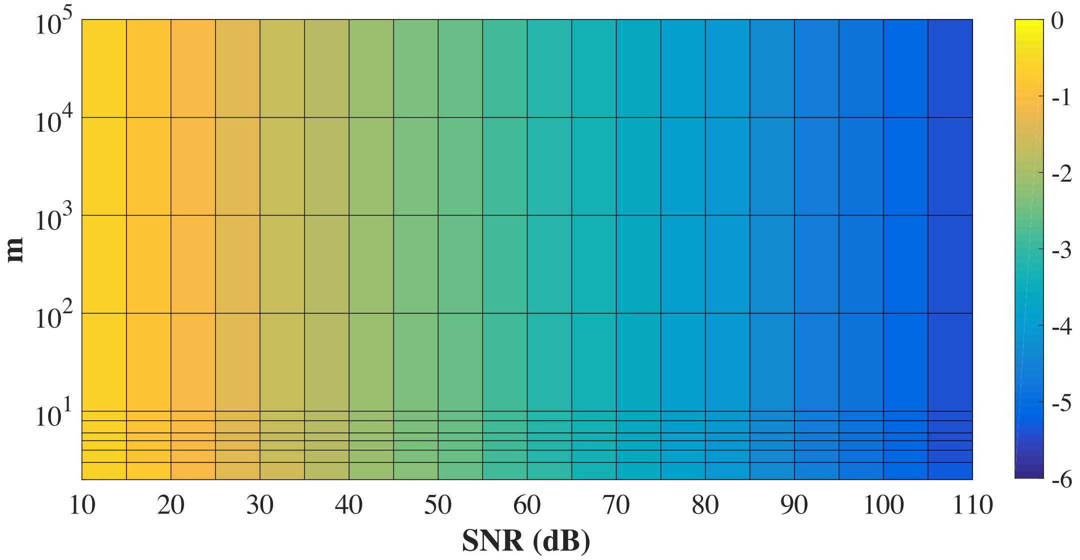

Figure 2.18 Cramér-Rao bound (CRB) for a signal composed of two reflectors separated in delay time by m *DFT bins. The SNR plotted here are values are from the optical frequency domain. Here, the square root of the CRB is normalized to DFT bin size and plotted on the common logarithmic scale.*

In general, for any given reflector spacing, the CRB decreases as SNR increases. For the most part, reflector separation has no effect on the CRB; however, as reflector separation grows very small, the CRB does increase slightly any given SNR. This is shown in Figure 2.19.

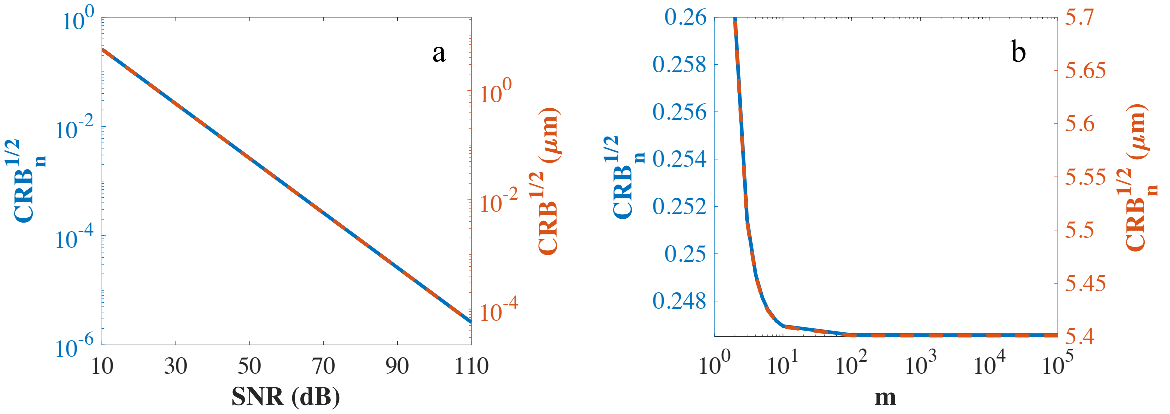

Figure 2.19 (a) Dependence of CRB on SNR for a reflector separation of 2 DFT bins. (b) In general, the CRB depends only on SNR, but it does increase for very small reflector separations. The line here shows CRB as a function of reflector separation at a SNR of 10 dB. The left axes show the square root of CRB normalized to DFT bin size, while the right axis shows, for the model described in Section 2.2.1, the equivalent distance in free space.

2.4.2 Comparison of precision for frequency estimation methods

To examine the variances of LLR, ESPRIT, NLS, and Candan’s estimator, I have simulated two scenarios based on the model described in Section 2.2.1. The two reflectors in the measurement interferometer are the front and back surfaces of a fused silica window at 25 °C, 0.5 mm thick in one scenario, and 5 mm thick in the other. At a series of SNRs, 510 simulations were run, 10 simulations each at 51 reflector locations spaced evenly across the length of one DFT bin. In Figure 2.20, the standard deviations of recovered reflector positions are plotted along with the square root of the CRB.

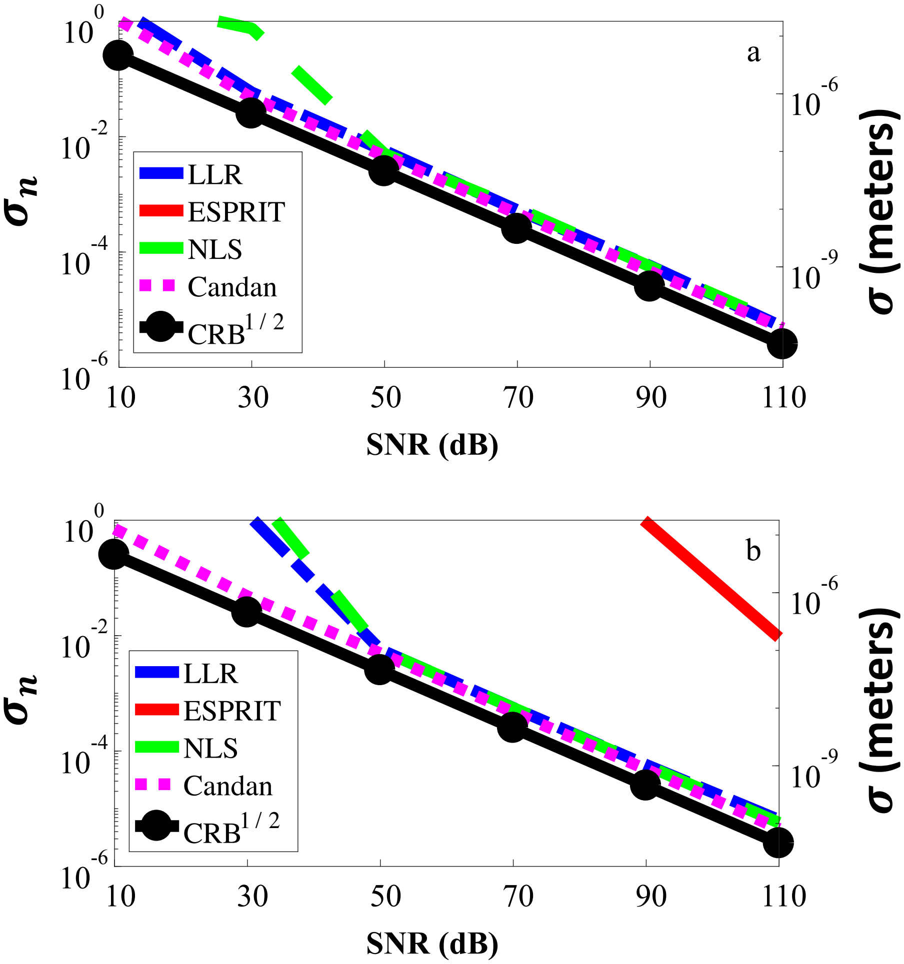

Figure 2.20 Standard deviations of delay time estimates for reflectors separated by (a) 0.5 mm and (b) 5 mm of fused silica at 25 °C. The left y-axis shows standard deviation normalized to DFT bin size; the right y-axis shows the corresponding distance in free space. ESPRIT estimates were made using an order 100 covariance matrix.

ESPRIT is decidedly the least precise estimator. Its variance quickly rises as reflector spacing decreases. In fact, for reflectors separated by 0.5 mm of fused silica, the standard deviation of ESPRIT estimates is larger than the size of one DFT bin for all the SNRs shown in Figure 2.20. The poor tolerance of ESPRIT to closely spaced frequencies (or here, to closely spaced delay times), has been noted in the literature, and a modified version of ESPRIT can be used to increase the precision of ESPRIT estimates for closely spaced reflectors [89]. Artificially increasing reflector spacing by downsampling the sampled signal $U(\nu[t])$ and interleaving the downsampled snapshots into a modified covariance matrix may increase the precision of ESPRIT estimates of closely spaced delay times. Unfortunately, this also decreases the unambiguous range of the SWI system in proportion to the downsampling rate. (For example, a downsampling rate of 2 halves unambiguous range, and a downsampling rate of 10 reduces unambiguous range to 10% of its original value.) Furthermore, the variances of these modified ESPRIT estimates are still higher than the variances of LLR and NLS estimates for the model used here. This is shown in Figure 2.21.

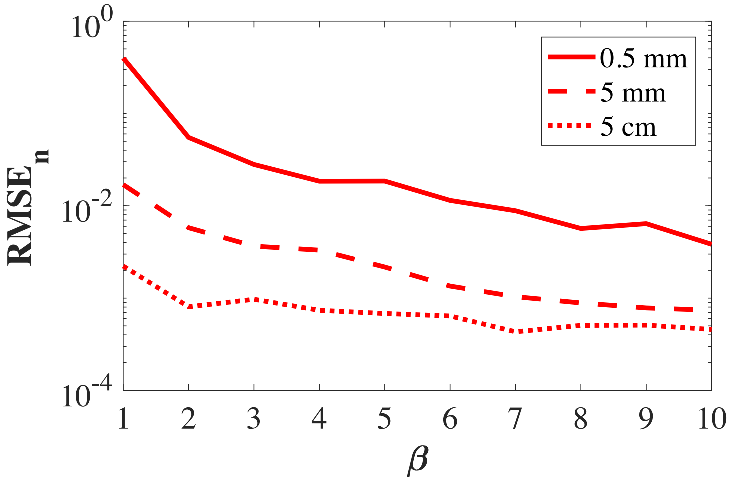

Figure 2.21. Standard deviation, normalized to DFT bin size, in modified ESPRIT estimates of the delay times between reflectors separated by 0.5 mm, 5 mm, and 5 cm of fused silica at 25°C. When reflectors are more closely spaced, increasing the downsampling rate (or interleaving factor) β increases estimate precision.

Above 50 dB of SNR, LLR, NLS, and Candan estimates have comparable precision. Below 50 dB, however, Candan's estimator exhibits the highest precision. LLR estimates, perhaps counterintuitively, show higher precision in the 0.5 mm case than in the 5 mm case. These results can be explained by carefully considering the difference in SNR between the optical frequency and delay time domains.

In the optical frequency domain, signal-to-noise ratio (SNR) is given by

$$SNR_{\nu} = 10\log_{10}\left(\frac{P_s}{P_N}\right), \tag{2.36}$$

where P_N is the noise power, and the signal power P_S is given by

$$P_s = \frac{1}{N}\sum_{k=1}^{N} |u[k]|^2 \,. \tag{2.37}$$

The signal u is composed of N total sample points. Parseval's relation for the DFT [90] gives the following relationship between signal power in the optical frequency domain and signal power in the delay time domain:

$$\frac{1}{M}\sum_{k=1}^{M} |u[k]|^2 = \sum_{m=1}^{M} |U[m]|^2 \,. \tag{2.38}$$

Consequently, the signal-to-noise ratio in the delay time domain (SNR) is given by

$$SNR_{\tau} = 10\log_{10}\left(\frac{P_s}{P_N}\right) + 10\log_{10}(M) \,. \tag{2.39}$$

This may be considered intuitively by recalling that after the Fourier transform, signal power is confined to only a few DFT bins, while noise power is distributed evenly across all M sample points, provided that the noise is white.

During the LLR estimation process, M_e points are extracted from around a peak of interest in the delay time domain. After a shift to move the peak to baseband, the extracted points are multiplied by a window function and inverse Fourier transformed. Parseval's relation predicts that after the inverse Fourier Transform is applied, the SNR for the extracted signal will be given by

$$SNR_{v,W} = 10\log_{10}\left(\frac{P_s}{P_N}\right) + 10\log_{10}(M) - 10\log_{10}(M_e) . \tag{2.40}$$

This leads to the conclusion that extracting fewer points around a peak of interest leads to a more precise LLR estimate. Unfortunately, extracting fewer points also degrades the accuracy of LLR estimates (Figure 2.11). By contrast, Candan's estimator uses only the three highest-magnitude points about a peak of interest and may therefore be expected to give even more precise estimates than LLR without suffering a corresponding degradation in accuracy.

2.4.3 Estimator root-mean-square error comparison

In any measurement scenario, DFT bin size uncertainty, estimator bias, and estimator precision all combine to determine the overall reliability of SWI measurements. The combined contributions of these three measures can be quantified by evaluating the root-mean-square error (RMSE) for each estimator. For an estimate $\widehat{\Delta\tau}$ of differential delay time, the mean-square-error (MSE) of the estimate is the expectation value of the square of the difference between delay time estimate $\widehat{\Delta\tau}$ and the true differential delay time $\Delta\tau$ [91], i.e.

$$MSE\left(\widehat{\Delta\tau}\right) = E\left[\left(\widehat{\Delta\tau} - \Delta\tau\right)^2\right] . \tag{2.41}$$

This is equivalent to the sum of the estimator variance and the square of estimator bias, so

$$MSE\left(\widehat{\Delta\tau}\right) = \sigma^2 + B^2 . \tag{2.42}$$

For the SWI model used here, DFT bin size uncertainty may be considered as a potential source of systematic error, and therefore a contributor to overall measurement bias. Bias in estimates of differential delay time $\widehat{\Delta\tau}$ is consequently given by

$$B = B_e + B_{HCN} , \tag{2.43}$$

where estimator bias B_e is determined by bias in the estimate of the fractional location δm of a delay time within a DFT bin, and potential systematic error in DFT bin size B_{HCN} is determined by the gas reference cell calibration. For the numerical model used here, DFT bin size is approximately 112 fs, 1σ uncertainty in DFT bin size 0.6 as, and DFT bin size bias B_{HCN} is approximately equal to $5.36\times10^{-6}\ {}^{s}/_{\Delta\tau}$.

Figure 2.22 shows RMSE for differential delay time estimates across a range of SNRs and reflector separations. For all four estimators, RMSE decreases as SNR increases. ESPRIT estimates are dominated by estimator variance, and show a RMSE minimum for wider reflectors separations of approximately 10^3 to 10^4 DFT bins. LLR and Candan estimates show the lowest RMSE when estimate bias B_e is roughly equal to DFT bin size bias B_{HCN}. For NLS estimates, neither estimator bias nor variance increase at small reflector separations, and consequently, RMSE in NLS estimates is primarily determined by only SNR and DFT bin size bias. For each the four estimators, RMSE may be compared to the Cramér-Rao lower bound (Figure 2.18), as the CRB is equal to MSE for an unbiased estimator with the lowest possible variance.

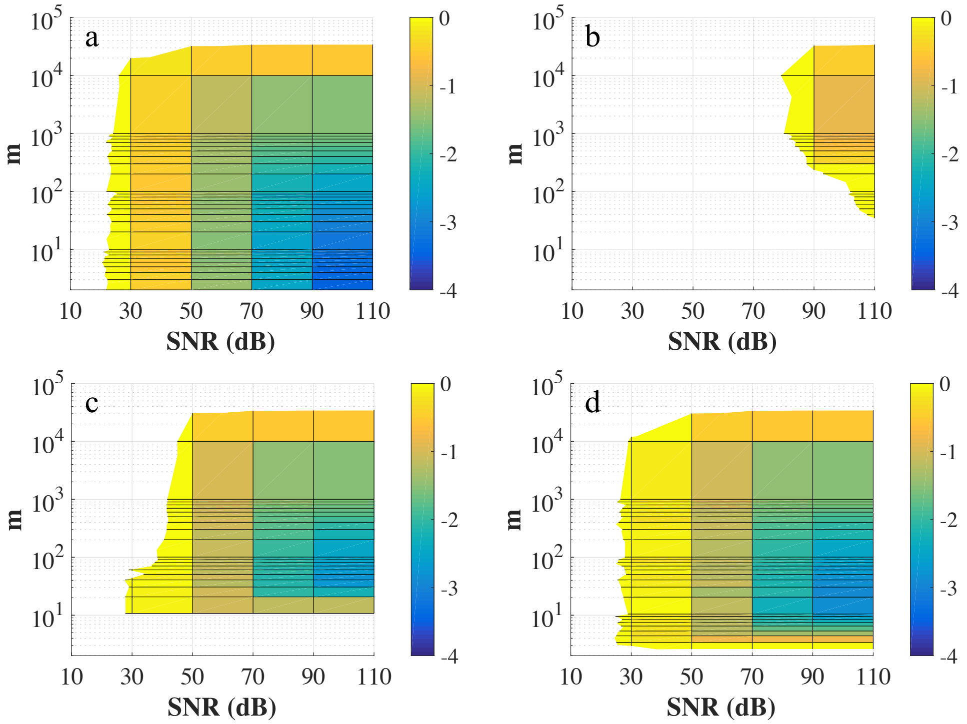

Figure 2.22 RMSE for estimates of the delay time between two reflectors separated by m *DFT bins. Estimates were made using (a) NLS, (b) ESPRIT, (c) LLR, and (d) Candan's estimator. RMSE is normalized to DFT bin size and plotted on the common logarithmic scale. Values greater than 1 DFT bin are excluded from the figures because they are outside the realm in which superresolved measurements are meaningful.*

2.5 Conclusions

All the estimators examined here offer resolution limits significantly below the traditional Fourier transform limit. However, there is no universal best estimator for superresolved SWI measurements. Rather, the best choice of estimator is determined by measurement hardware and conditions. The ideal estimator would be fast, unbiased, and noise tolerant, and none of the estimators examined here fulfill these requirements under all circumstances. For example, ESPRIT satisfies only one of these requirements. While ESPRIT estimates are asymptotically unbiased, their noise tolerance suffers greatly when target reflectors are closely spaced.

Additionally, for the system modeled here, which contains many points per data set and requires the computation of a large covariance matrix, ESPRIT is far slower than either LLR or Candan's estimator.

In terms of both uncertainty and precision, NLS and Candan's estimator emerge as the superresolution estimators of choice. NLS estimates are both asymptotically unbiased and noise tolerant. Additionally, NLS estimates suffer no increase in uncertainty when reflectors are closely spaced. However, because NLS is an optimization method, it is comparatively slow. Additionally, with the exception of data containing reflections from only two target surfaces, the required quality of the initial guesses used to seed the optimization process is unknown. Furthermore, omitting any reflection—even a spurious reflection—from the optimization process will alter the search space and degrade results.

Candan's estimator is both faster and more noise tolerant than NLS. Although it is not an unbiased estimator, its bias in estimates of isolated delay times is inconsequentially small. Because it is a single frequency estimator, estimates of delay times in multi-reflector data may suffer bias as a consequence of spectral leakage. However, when reflectors are spaced by more than approximately 20 DFT bins—equivalent to approximately 0.34 mm of free space in the SWI model used for the numerical work presented here—the bias of Candan estimates can be negligibly small. Among the four estimators compared here, Candan's estimator offers the greatest practical utility. It is the estimator I have used for all the experimental work described in Chapters 3 and 4.

Chapter 3

Experimental Limits of Superresolved Swept-Wavelength Interferometry

In Chapter 2, I showed that frequency estimation methods can be used to superresolve SWI measurements, and that the resulting measurements may have RSME values below 10^{-3} of the Fourier-transform limited resolution of the SWI instrument. These results were obtained through numerical simulation and delineate the theoretical limits of superresolved SWI.

As a predictor of precision, my results are in excellent agreement with experimental high-precision SWI measurements reported in the literature [33] [34] [20]. However, the experimental accuracy of superresolved SWI is much more difficult to evaluate. The accuracies of the optical frequency domain reflectometer used in [33] and the spectral-domain optical coherence tomography system used in [34] were evaluated by comparing measured optical path lengths (OPLs) with the known OPLs of dielectric reference samples. These accuracies were reported as $2.5\text{x}10^{-3}$ of DFT bin size (or ±61 nm) in the first case, and 0.6 nm in the second. However, establishing accuracy by comparing measurements of a single OPL to a reference value is problematic for two reasons. First, even very slight temperature fluctuations in either the SWI or the sample will cause the measured OPL of the reference to change on the nanometer level due to thermal expansion of the standard, temperature-dependent changes in its refractive index, or both. Second, even if the temperature of the instrument and the sample are well-controlled, it is possible for a measurement of a single OPL to be unbiased, when a measurement of a slightly different

OPL, made with the same instrument and estimation method, would be more biased and therefore less accurate.

In this chapter, I present what I believe is the most rigorous demonstration to date of the experimental accuracy of superresolved SWI across the range of a single DFT bin. I first discuss the effects of six potential sources of systematic error—non-Gaussian noise, spurious delay times, laser power fluctuations, dispersion mismatch, temperature drift in the instrument, and laser sweep rate nonlinearity—on the accuracy of SWI measurements, and show how these effects may be controlled. I then present an experimental measurement of the accuracy of an SWI system, demonstrating superresolved accuracy of approximately $2\mathrm{x}10^{-3}$ of the system's transform-limited resolution in 101 measurements across a range of approximately 3 sequential DFT bins.

3.1 Experimental Sources of Bias

In Chapter 2, the numerical model used to determine the limits of uncertainty and precision for superresolved SWI included a DC term, two oscillatory terms, and an additive white Gaussian noise term (Equation (2.9)). The tractable nature of Gaussian random variables makes additive Gaussian noise an attractive and sensible choice for a numerical modeling study, but real-world SWI measurements will include many non-Gaussian noise sources. Additionally, real-world systems will be exposed to other environmental factors, such as mechanical vibrations or temperature fluctuations, that may degrade measurement accuracy and precision. In general, any noise or environmental variation that cannot be represented as additive white noise has the potential not only to degrade measurement sensitivity, but to introduce systematic error, or bias, into superresolved SWI measurements.

3.1.1 Non-Gaussian noise

All SWI systems are subject to the effects of at least four non-Gaussian noise sources: relative intensity noise (RIN) from the tunable laser source, phase noise arising from the finite coherence length of tunable laser sources, quantization noise arising from the digitization of the detected optical signal, and shot noise arising from the quantized nature of light. All four of these noise sources are known to degrade SWI measurement sensitivity, but their effects on measurement bias in superresolved SWI measurements are unknown.

3.1.1.1 Relative intensity noise (RIN)

RIN has been identified a potential [92] or known [93] limiting noise term in a number of SWI experiments, although in the system used for the experiments described in this chapter, it is not expected to be the limiting noise term. Nevertheless, it is important to note that the frequency spectrum of RIN is not white, but has a 1/f character that asymptotically approaches a constant value at high frequencies. To the best of my knowledge, no model for RIN in a SWI system currently exists, and any contribution that RIN makes to bias in superresolved SWI measurements must be determined experimentally.

3.1.1.2 Phase noise

Both the amplitude and frequency spectrum of phase noise depend on the specific instrument and sample characteristics in SWI systems. The amplitude of phase noise depends on sample reflectivity and laser coherence time, and its frequency distribution depends on laser coherence time and tuning rate, as well as the path length difference between reference and sample arms [94]. Shorter path length differences correspond to wider, flatter frequency spectra for phase noise [51]. The path-length difference dependency of phase noise becomes noteworthy for SWI measurements of samples containing multiple and widely separated reflectors (such as in the multi-channel system described in Chapter 4). The delay time spacing between the DC term and the highest delay time cross-term is equivalent to the maximum delay time separation of sample reflectors. Consequently, the usable unambiguous range of the system is reduced by the maximum delay time separation of sample reflectors, and measurements of interest are confined, in the worst-case, to the second half of the system's unambiguous range. This raises the maximum amplitude of phase noise and decreases the flatness of the phase noise frequency spectrum.

3.1.1.3 Quantization noise

In the SWI system used for the experiments described in this chapter, quantization noise is expected to be the dominant noise source. Fortunately, given sufficient bit depth, the spectrum of quantization noise approaches that of an additive white Gaussian noise source [95] [96] [97]. It should still be noted, however, that quantization noise is not stochastic, and when the underlying signal is periodic, the deterministic nature of quantization noise may add to measurement bias.

3.1.1.4 Shot noise

Shot noise, or Poisson noise, is a direct and unavoidable consequence of the quantized nature of light. Poisson random variables have variance (or noise power) equal to the square root of the distribution mean (or signal power) [98] [99]. Consequently, deterministic signal oscillations cause noise fluctuations and possible noise correlations [100] [101]. As is the case for RIN, phase noise, and quantization noise, the exact contributions of correlated shot noise to measurement bias are unknown, difficult to analytically determine with sufficiently useful generality, and demonstrate the necessity of experimental verification for superresolved SWI.

3.1.2 Spurious delay times

Perhaps the most obvious potential source of measurement bias is spectral leakage from unwanted, or spurious, peaks in delay time. Spurious peaks may find their way into SWI data in a number of ways, the two most common being through mechanical vibrations of the SWI system or as a result of unwanted reflections at fiber connections or components in the SWI system.

Mechanical vibration is a particularly insidious source of spurious delay times—the extreme sensitivity of SWI systems to vibration is evidenced in the large number of publications describing OFDR vibration measurements, for example: [19] [18] [102] [103] [104]. In general, mechanical vibration causes sidelobes to appear on either side of all delay time peaks present in an SWI measurement [19]. The magnitude of these sidelobes depends on the vibrational amplitude, and their distance from the center peak depends on both the laser sweep rate and the vibrational frequency. These effects can be expressed quantitatively, according to:

$$\begin{aligned}\widetilde{U}[\tau] = {} & \{I_0 + R_S I_0 [J_0^2(A) + 2J_1^2(A)]\}\delta(0) \\ & + \sqrt{R_S}\, J_0(A) I_0\, \delta(\tau - \tau_0) \\ & + \sqrt{R_S}\, J_1(A) I_0 \left\{ e^{j2\pi f_m \frac{\nu_c}{\gamma}} \delta\left[\tau - \left(\tau_0 - \frac{f_m}{\gamma}\right)\right] \right. \\ & \left. + e^{-j2\pi f_m \frac{\nu_c}{\gamma}} \delta\left[\tau - \left(\tau_0 + \frac{f_m}{\gamma}\right)\right] \right\}\end{aligned} \tag{3.1}$$

In Equation (3.1), a signal with a single reflector of reflectivity R_S, located at delay time τ_0, is perturbed by a vibration with amplitude A and frequency f_m. The positive sideband of the delay time signal $\widetilde{U}[\tau]$ contains a DC peak, a peak centered at delay time τ_0, and two sidelobes spaced at delay times $\pm\frac{f_m}{\gamma}$ on either side of the delay time peak. The constant γ represents the sweep rate of the laser; ν_c is the center frequency of the laser sweep; and J_0 and J_1 are the zeroth and first order Bessel functions of the first kind. (The derivation and assumptions included in Equation (3.1) are detailed in Appendix A).

The bias that mechanical vibration may induce in estimates of any given delay time can be expected to increase with increasing vibration amplitude and with decreasing vibrational frequency. Using the numerical model from Section 2.2.1, I quantified these effects for Candan's estimator. The results are shown in Figure 3.1. The bias in estimates of the delay time to a single reflector that is caused by a pair of vibrational sidelobes (Figure 3.1c,d), is considerably less than the bias caused by the presence of a single neighboring reflector (Figure 3.1a,b).

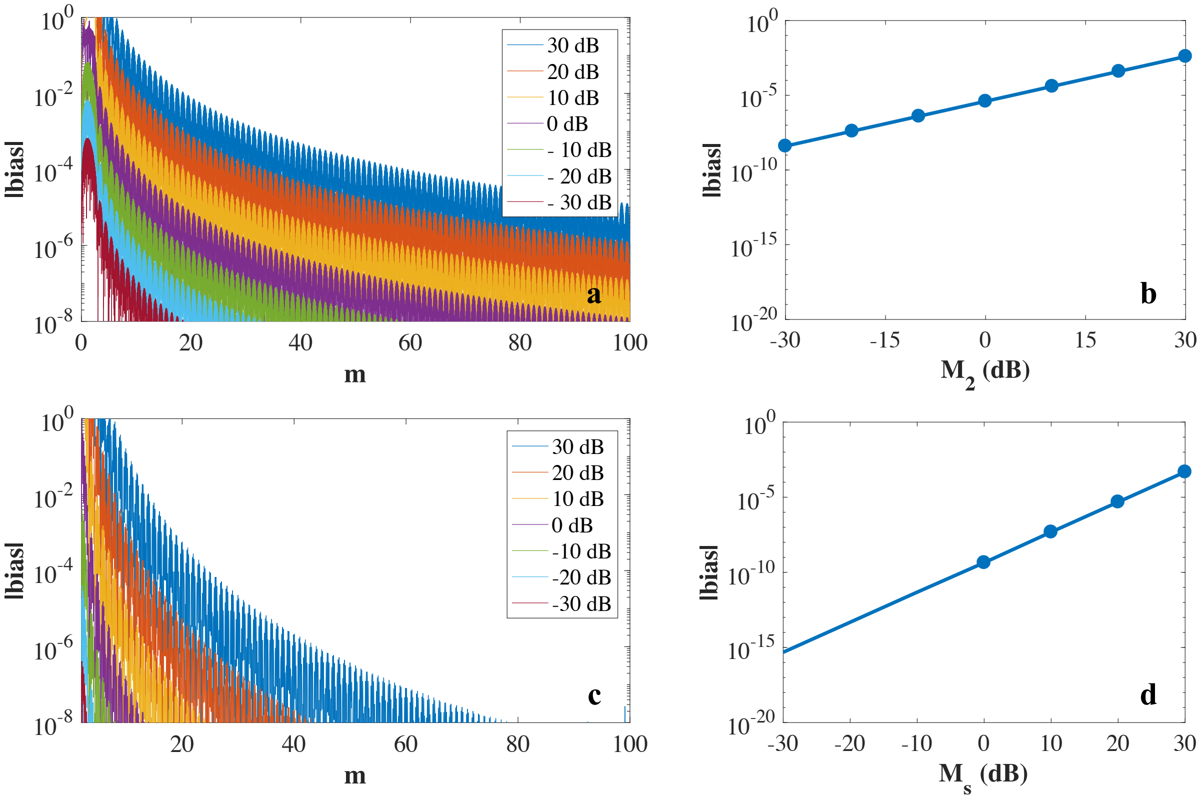

Figure 3.1 (a) Magnitude of bias, normalized to DFT bin size, in the estimated delay time of a reflector separated by m *DFT bins from a second reflector. The amplitude of the second reflector, relative to the first, is noted in the legend. (b) Magnitude of bias, normalized to DFT bin size, in the estimated delay time of a reflector separated by 20.5 DFT bins from a second reflector with relative amplitude* M_2. *(c) Magnitude of bias in the estimated delay time of a reflector flanked by two vibrational sidelobes, each separated by* m *DFT bins from the main peak. The legend notes the amplitude of the sidelobes relative to the main lobe. (d) Magnitude of bias in the estimated delay time of a reflector separated by 20 DFT bins from two vibrational sidelobes of amplitude* M_s.

3.1.3 Laser power fluctuations

In an ideal SWI system, laser power would be constant as a function of wavelength. In such a case, laser power may be represented by a rectangular, or rect, function—outside of the sweep bandwidth, laser power is zero, and inside laser power is always equal to a constant value (Equation (2.5)). While small deviations from this assumption are unlikely to affect accuracy or precision in a transform-limited SWI system, the differences in estimate bias for Candan estimates made using different window functions [61] suggests that estimate bias may be affected by laser power fluctuations. This is also suggested by the differences in LLR estimate bias when the estimation procedure includes windowing by either rect or Hanning windows (Figure 2.13).

Laser power fluctuations may, in fact, be considered as an undesirable window function for SWI data. This is illustrated in Figure 3.2, where the measured power *P* of an Agilent 81680A external cavity tunable laser is compared to the rect and Hanning window functions. The product of the Hanning window and measured laser power variation *P* is also shown.

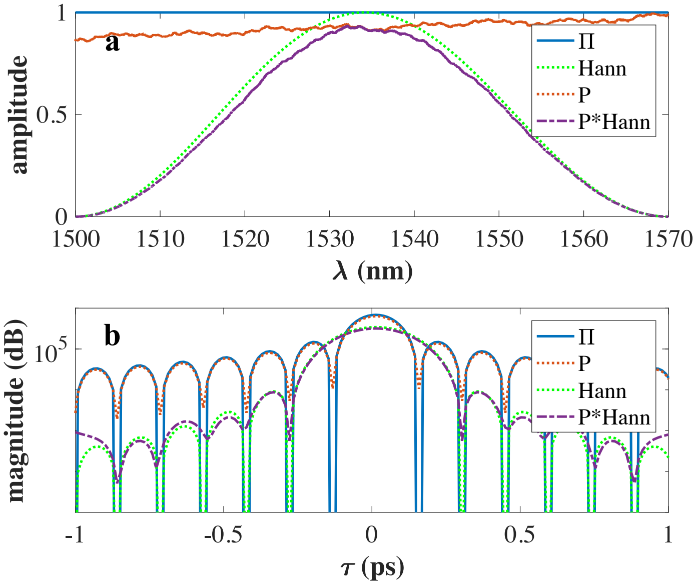

Figure 3.2 (a) Laser power P *changes as a function of output wavelength λ during the course of a laser sweep. This power fluctuation is compared to the rectangular (Π) and Hanning window functions. (b) Delay time spectra of rectangular and Hanning window functions. The differences in spectra between these functions and the spectrum of laser power fluctuation are slight but distinct.*

The exact effect of laser power fluctuation on estimate bias is not generalizable: it is as unique as the power fluctuations of any laser source during any given sweep. Nevertheless, looking at a single example will provide some general insight into the form and scale of the bias that laser power fluctuation may induce in differential delay time measurements. Here, I look at the effect of power fluctuations in the output of an Agilent 81680A tunable laser, as this laser was used for both the experiments described in the later parts of this chapter and those in Chapter 4.

Noise-free signal data $U(\nu)$ was generated using the numerical model described in Section 2.2.1. Before being Fourier transformed, this signal was multiplied by measured laser power output $P(\nu)$ (Figure 3.2a) and by either a rect or Hanning window (Figure 3.3). Measured signal power $P(\nu)$ was normalized to a maximum value of 1. After the signal was Fourier transformed, Candan's estimator was used to estimate the differential delay time between the two equal amplitude reflectors. The bias in these estimates is plotted in Figure 3.3 as a function of reflector separation.

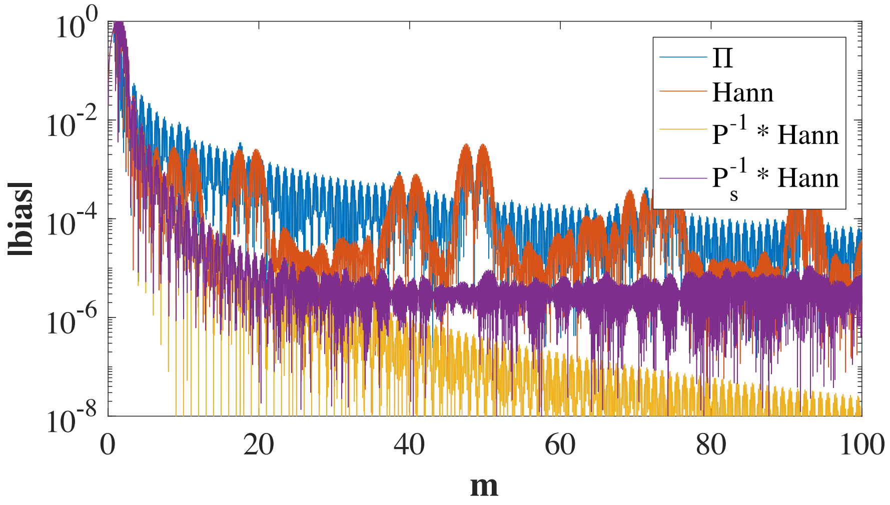

Figure 3.3 Magnitude of bias, normalized to DFT bin size, in the estimated delay time difference between two equal amplitude reflectors separated by m *DFT bins. Appling a rectangular (blue line) or Hanning window (orange line) to the data without correcting for power fluctuations allows occasional unexpected increases in bias. Applying a Hanning window and perfectly (yellow line) or imperfectly (purple) line correcting for laser power fluctuation significantly reduces the negative impact of laser power fluctuations.*

Figure 3.3 shows that laser power fluctuation may indeed increase bias in differential delay time estimates. Two specific features of this bias increase are worth noting. First, the magnitude of estimate bias varies unpredictably as a function of reflector spacing *m*; this is due to the non-periodic variation of laser power as a function of optical frequency. Second, the use of a Hanning window instead of a rect window does not mitigate the increases in estimate bias caused by laser power fluctuation. In fact, the effects of laser power fluctuation are more noticeable when a Hanning window is used. With a rect window, the bias from spectral leakage overshadows bias from laser power fluctuation. However, when a Hanning window is applied, the increase in bias caused by laser power fluctuation is shown to be quite large, over two orders of magnitude for some reflector separations.

In a physical SWI system, the increase in estimate bias caused by laser power fluctuation could be eliminated by using balanced detection to measure the signal $U(\nu)$. Mathematically, this is equivalent to multiplying the corrupted signal $U(\nu) \cdot P(\nu)$ by the inverse values $P^{-1}(\nu)$. Unfortunately, perfect correction may only be achieved with perfect path length matching between the two inputs to the balanced detector. However, even with imperfect path length matching, balanced detection can still greatly reduce estimate bias caused by laser power variation.

To estimate the effect of imperfect path length matching in a balanced detection system, I examine the effect of a one-sample shift in power correction. Mathematically, this is equivalent to multiplying the corrupted signal by inverse values P_s^{-1}, where

$$P_s^{-1}(\nu[m]) = P^{-1}(\nu[m-1]) \tag{3.2}$$

Allowing for a shift of at most one sample restricts the path length mismatch Δd between the two inputs of the balanced detector to

$$\Delta d \leq \frac{c_0 \Delta\lambda}{\gamma n_g M} \tag{3.3}$$

where c_0 is the speed of light in vacuum, $\Delta\lambda$ is the laser sweep bandwidth, γ is the laser sweep rate, n_g is the average group index of the paths in the SWI system, and M is the total number of samples in sampled signal $U(\nu[m])$. The following values for these constants are representative of the experimental work described later in this thesis:

$$\Delta\lambda = 70\ \mathrm{nm}\ ,$$

$$\gamma = 40\ {}^{\mathrm{nm}}/_{\mathrm{s}}\ ,$$

$$n_g = 1.44486\ ,$$

$$M = 900{,}000\ .$$

For these constants, the maximum path length mismatch Δd is equal to 403 m, a constraint that may easily be satisfied. For measured laser power variation $P(\nu)$ (Figure 3.2), Figure 3.3 shows the difference between power correction with perfect path length matching and power correction that is shifted by one sample. Without perfect path length matching, laser power fluctuation still enforces a lower limit on estimate bias. For the numerical model examined here, this lower limit is approximately 10^{-5} of one DFT bin. In this model, fractional DFT bin size uncertainty has a 1σ value of approximately $5\text{x}10^{-6}$, meaning that only for NLS estimates of reflector separations of less than about 10 DFT bins will laser power variation make any significant contribution to measurement RMSE.

3.1.4 Dispersion mismatch

To explain the effects of dispersion mismatch in SWI, I begin with a brief overview of the use of a secondary interferometer to trigger sample acquisition in the primary measurement interferometer. Because sweep rates of tunable lasers are, in general, not constant in optical frequency, sampling the output of SWI systems at equal intervals in lab time t will result in the signal $U(\nu[t])$ being sampled unevenly in optical frequency. This can cause significant broadening of peaks in delay time [52], since uniform sampling is an underlying assumption in the discrete Fourier transform. The use of an auxiliary interferometer to linearize samples in optical frequency was introduced by Brinkmeyer and Glombitza in 1991 [105], and the concept has found widespread use since then, either as a method to measure and later correct for sweep rate nonlinearities, or as a method to trigger the acquisition of evenly spaced samples in the measurement interferometer [106]. Here, I consider the latter case.

The signal from the trigger interferometer is periodic and, provided the slow-tuning approximation holds—i.e. the product of the laser sweep rate and the square of the delay time difference between arms of the trigger interferometer is much less than one—linear in optical frequency [52]. In this case, the signal $U_t(\nu)$ is given by

$$U_t(\nu) = U_0[1 + \cos(\, 2\pi\nu\tau_t(\nu)\,)]\,, \tag{3.4}$$

where τ_t is the delay time difference between arms of the trigger interferometer. Each period of signal $U_t(\nu)$ triggers the acquisition of a sample in the measurement interferometer (typically at upward zero-crossings of the trigger signal).

In a fiber-based SWI system, trigger delay time τ_t is not constant; dispersion in the optical fiber means that trigger delay time is a function of optical frequency and changes during the course of a laser sweep. This has two significant implications. First, the measurement and trigger interferometers must be dispersion matched for the signal from the measurement interferometer to be evenly sampled in optical frequency. Second, dispersion in the trigger interferometer may increase DFT bin size uncertainty $u(s_\tau)$ (Equation (2.33)).

3.1.4.1 Dispersion matching

To understand the dispersion matching requirements for the trigger and measurement interferometers, consider a simple form of the signal $U_{ms}(\nu)$ from the measurement interferometer:

$$U_{ms}(\nu) = U_0[1 + \cos(\, 2\pi\nu\tau_{ms}(\nu)\,)]\,. \tag{3.5}$$

The period of this signal is equal to the delay time difference τ_m, and is sampled at optical frequencies ν, where

$$\nu = \nu_0 + m \cdot \delta\nu_{ms}\,, \qquad m = \{0,1,\dots,M-1\}\,. \tag{3.6}$$

For the signal $U_{ms}(\nu)$ to be sampled at even intervals, either $\tau_{ms}(\nu)$ and $\delta\nu_{ms}$ must both be constant, or their product $\tau_{ms}(\nu)\cdot\delta\nu_{ms}$ must be constant. Since dispersion causes τ_{ms} to change as a function of optical frequency, then the requirement

$$\tau_{ms}(\nu)\cdot\delta\nu_{ms} = \mathrm{C} \tag{3.7}$$

stands, and each frequency sampling interval $\delta\nu_m$ must also change during the course of a laser sweep in order to maintain even sampling.

Provided the trigger and measurement interferometers are correctly path matched[2], then

$$\delta\nu_t = \delta\nu_{ms} \quad \forall \quad \delta\nu\,; \tag{3.8}$$

that is, the frequency interval $\delta\nu_t$ between upward zero-crossings of the trigger signal is equal to the frequency interval $\delta\nu_{ms}$ between samples acquired in the measurement interferometer, for all such frequency interval pairs across the laser sweep bandwidth.

Consequently, if the signal from the measurement interferometer is to be evenly sampled, the phase spacing between measured samples is given by

$$2\pi\delta\nu_t\tau_{ms}(\nu) \;= 2\pi\frac{\tau_{ms}(\nu)}{\tau_t(\nu)}. \tag{3.9}$$

Rewriting Equation (3.9) as a function of optical path length instead of delay time gives

$$2\pi\delta\nu_t\tau_{ms}(\nu) = 2\pi\frac{d_{ms}}{d_t}\frac{n_{ms}(\nu)}{n_t(\nu)}, \tag{3.10}$$

where d_{ms} and d_t are the lengths of the path length mismatches in the measurement and trigger arms, respectively, and $n_{ms}(\nu)$ and $n_r(\nu)$ are the group refractive indices of the measurement and

---

[2] Here, correct path length matching means that the total time delay between the trigger signal times and measurement acquisition times is equal to half the time delay between the arms of the trigger interferometer (trigger delay time). Total time delay is equal to the sum of electronic delay, which is intrinsic to the data acquisition system, and optical delay, which can be controlled by adjusting the path length between trigger and measurement interferometers. See [52] and Section 3.1.6 for a more detailed discussion.

trigger interferometers. The phase change between samples in the measurement interferometer is constant—i.e. the measurement signal is evenly sampled—only if the group indices of the materials comprising the path length differences in both the measurement and trigger interferometers are the same for all frequency intervals $\delta\nu_t$.

When this condition is not satisfied, peaks in delay time become broadened and distorted. This is illustrated by the experimental data shown in Figure 3.4. When both the trigger and measurement interferometers are composed of Corning SMF-28 optical fiber, the dispersion matching condition of Equation (3.10) is met (Figure 3.4a). Breaking this condition by including a length of dispersion compensating fiber (Thorlabs DCF38) in the trigger interferometer dramatically distorts delay time peaks (in Figure 3.4b). (In Figure 3.4a, 311,522 samples were collected across a laser sweep from 1525 nm to 1564 nm, while in Figure 3.4b 524,288 samples were collected across a laser sweep from 1500 nm to 1564.17 nm. The x-axes in Figure 3.4 have been scaled accordingly to allow accurate visual comparison of peak widths.)

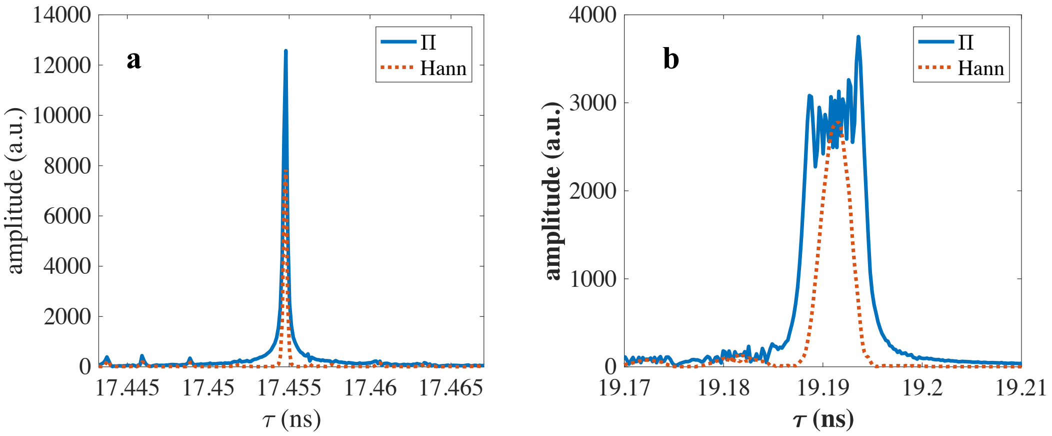

Figure 3.4 (a) Delay time measured in an SWI system with dispersion-matched trigger and measurement interferometers. (b) Breaking the dispersion matching requirement results in broadened and distorted delay time peaks. Results are shown for measurement signals multiplied by both rect and Hanning windows.

The SWI system used to collect the data shown in Figure 3.4 is illustrated in Figure 3.5. The tunable laser used here is an Agilent 81680A external cavity laser. The trigger interferometer uses a Michelson geometry and Faraday rotator mirrors to prevent polarization fading of the trigger signal and eliminate the need for polarization control in the trigger interferometer. In the measurement interferometer, a polarization diverse detection scheme is used to prevent fringe fading. The entire trigger interferometer, as well as the majority of the measurement interferometer, was housed in a machined aluminum enclosure to stabilize the temperature of the SWI system.

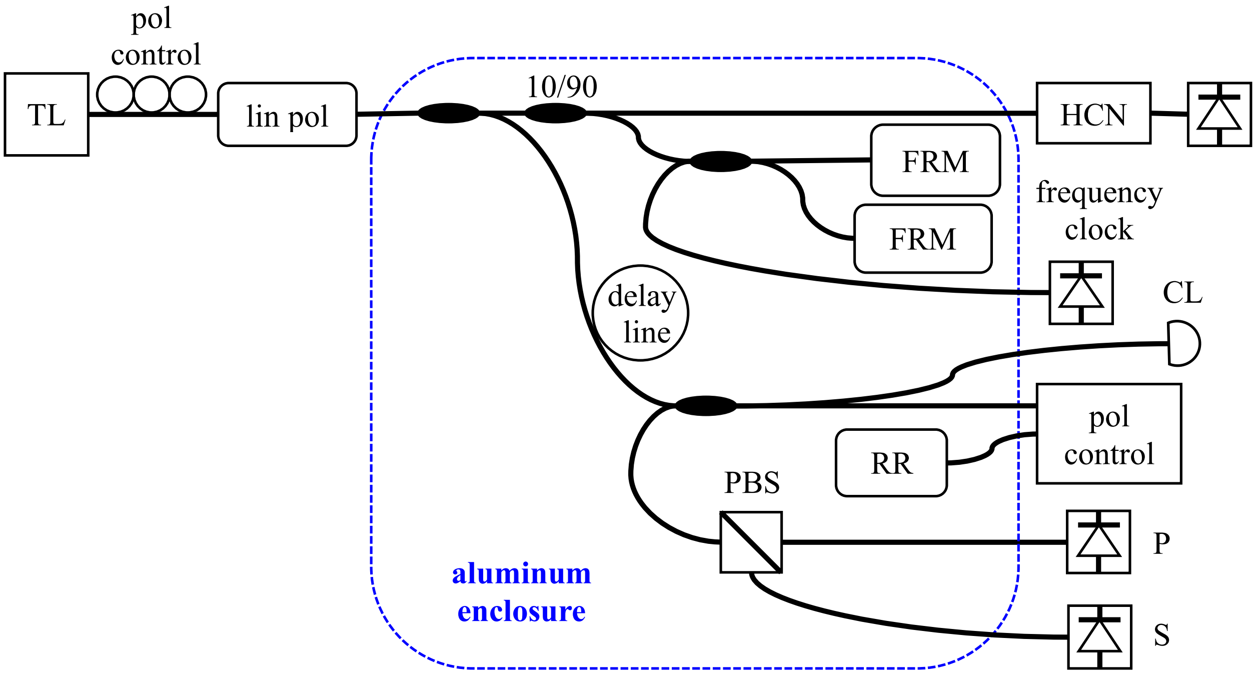

Figure 3.5 System diagram for the SWI experiments described in Section 3.1. All couplers are 3 dB unless otherwise noted. TL = tunable laser, FRM = Faraday rotator mirror, CL = collimating lens, RR = retroreflector, PBS = polarization beam splitter.

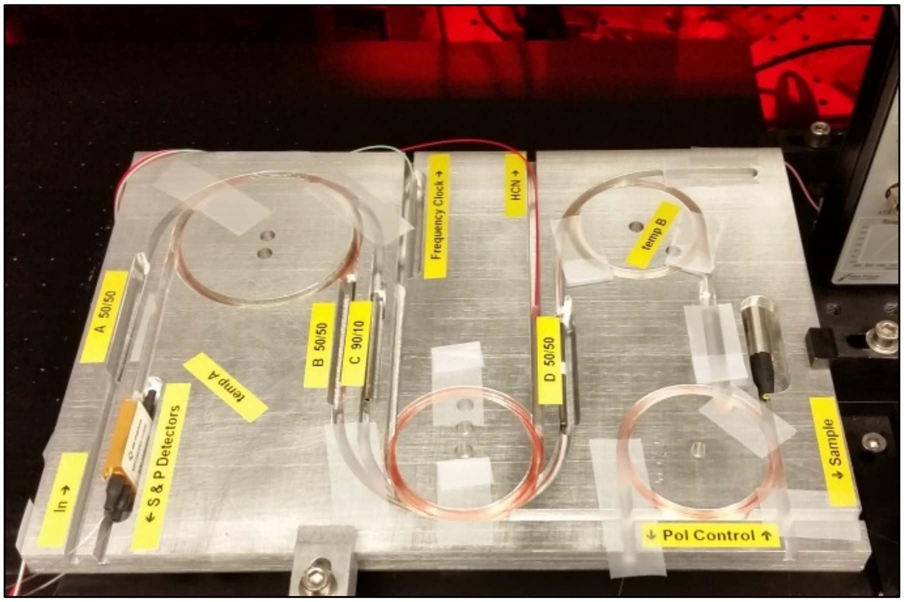

Figure 3.6 Custom-machined aluminum enclosure for the SWI system used for the experiments described in Section 3.1.

When the data shown in Figure 3.4a was collected, both the measurement and trigger interferometers were composed of Corning SMF-28 optical fiber, which has a maximum dispersion value of $18\ \mathrm{ps/nm\cdot km}$ at 1550 nm. For the data shown in Figure 3.4b, approximately one-third of the physical path length difference in the trigger interferometer was replaced with Thorlabs DCF28 dispersion compensating fiber, which has a dispersion value of $-38\ \mathrm{ps/nm\cdot km}$ at 1550 nm. This combination of optical fibers resulted in the cumulative dispersion of the trigger interferometer being near zero, while the dispersion of the measurement interferometer remained near $18\ \mathrm{ps/nm\cdot km}$.

3.1.4.2 Dispersion and DFT bin size uncertainty

In the analysis of Chapter 2, uncertainty in superresolved SWI measurements is determined by two quantities: uncertainty in DFT bin size and estimate bias (Equation (2.33)). Section 2.3.4

briefly described the trigger interferometer calibration method that is used both to determine DFT bin size and establish DFT bin size uncertainty. I will now describe this method in more detail before going on to discuss the implications of dispersion in the trigger interferometer on DFT bin size uncertainty.

In general, DFT bin size s_τ is given by the inverse of laser sweep bandwidth, or equivalently, by

$$s_\tau = (M\delta\nu)^{-1}\,, \tag{3.11}$$

as the exact sweep bandwidth is equal to the product of the total number of samples M and the optical frequency interval $\delta\nu$ between samples. Because one sample is acquired at each upward zero-crossing of the trigger interferometer signal $U_t(\nu)$ (Equation (3.4)), the optical frequency spacing between samples is equal to the inverse of trigger delay time. That is,

$$\delta\nu = \tau_t^{-1}\,, \tag{3.12}$$

and DFT bin size is thus given by

$$s_\tau = \frac{\tau_t}{M}\,. \tag{3.13}$$

Consequently, since DFT bin size is set by trigger delay time, uncertainty in DFT bin size is set by the method used to measure trigger delay time. The method I used for this measurement exactly follows the procedure described in [33]. Trigger delay time is measured by counting number of trigger signal fringe periods p that occur within the frequency spacing $\Delta\nu_{HCN}$ between two hydrogen cyanide absorption lines. This frequency spacing is measured by passing a portion of the laser sweep through a HCN gas cell. Thus

$$\tau_t = \frac{p}{\Delta\nu_{HCN}}\,, \tag{3.14}$$

and uncertainty in the measurement of trigger delay time $u(\tau_t)$ is given by

$$u(\tau_t) = \frac{\tau_t}{\Delta\nu_{HCN}}\left[\frac{u^2(p)}{\tau_t^2} + u^2(\Delta\nu_{HCN})\right]^{1/2}, \tag{3.15}$$

where $u(p)$ is uncertainty in the number of fringe periods between two HCN absorption lines, and $u(\Delta\nu_{HCN})$ is uncertainty in frequency spacing between those two absorption lines.

In Figure 3.7a, the measured absorption spectrum of HCN is shown as a function of laser wavelength λ. In Figure 3.7b, the Lorentizian fit to the R_{20} line is shown as a function of fringe period count p. The 1σ uncertainty in the fit is less than 0.04 of a fringe period.

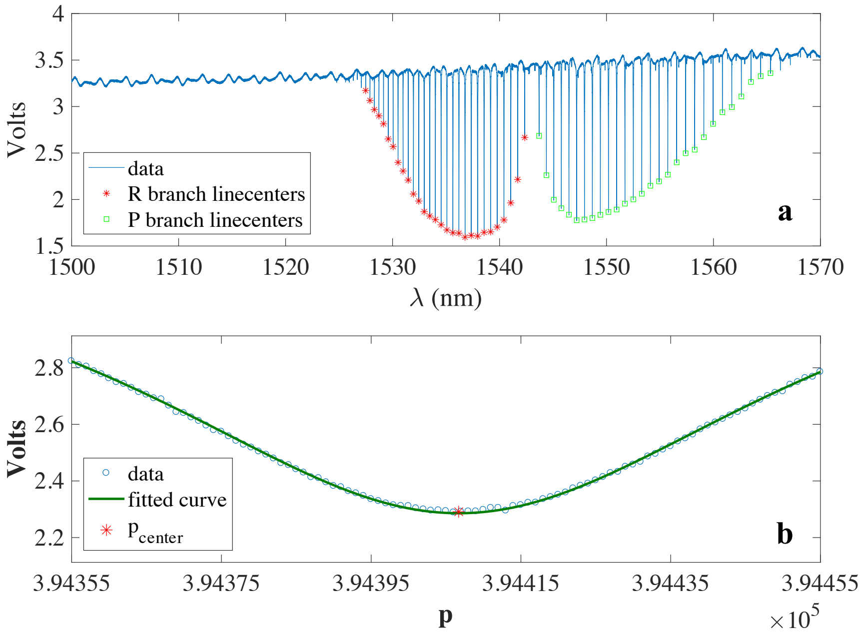

Figure 3.7 (a) Measured absorption spectrum from a Wavelength References HCN reference gas cell. (b) Lorentizian fit to R20 absorption line has an uncertainty of less than 0.04 fringe periods.

Dispersion in the trigger interferometer causes trigger delay time to vary as a function of optical frequency, gradually increasing over the course of a laser sweep. This effect can be observed by measuring the trigger delay time using a sequence of HCN absorption line pairs.

Figure 3.8 shows the same physical path length difference between arms of the trigger interferometer, measured using the following line pairs: $R_{25} - R_{24}$, $R_{25} - R_{23}$, $R_{25} - R_{22}$, …, $R_{25} - P_{24}$. As the frequency spacing between line pairs increases, measured trigger delay time increases. This is due to the increase in the average group index of SMF-28 optical fiber as the center wavelength of the frequency band defined by each absorption line pair increases.

In Figure 3.8, measured trigger delay time is plotted at the center of a 2σ confidence interval obtained from Equation (3.15), meaning that true trigger delay time lies somewhere within the span of the error bars with 95% probability [107]. When the trigger interferometer is composed entirely of SMF-28 optical fiber, the change in trigger delay time over the course of a single laser sweep can be easily observed (Figure 3.8a). By contrast, when one-third of the physical path length difference in the trigger interferometer was replaced with Thorlabs DCF28 dispersion compensating fiber, trigger delay time became near-constant as a function of optical frequency (Figure 3.8b).

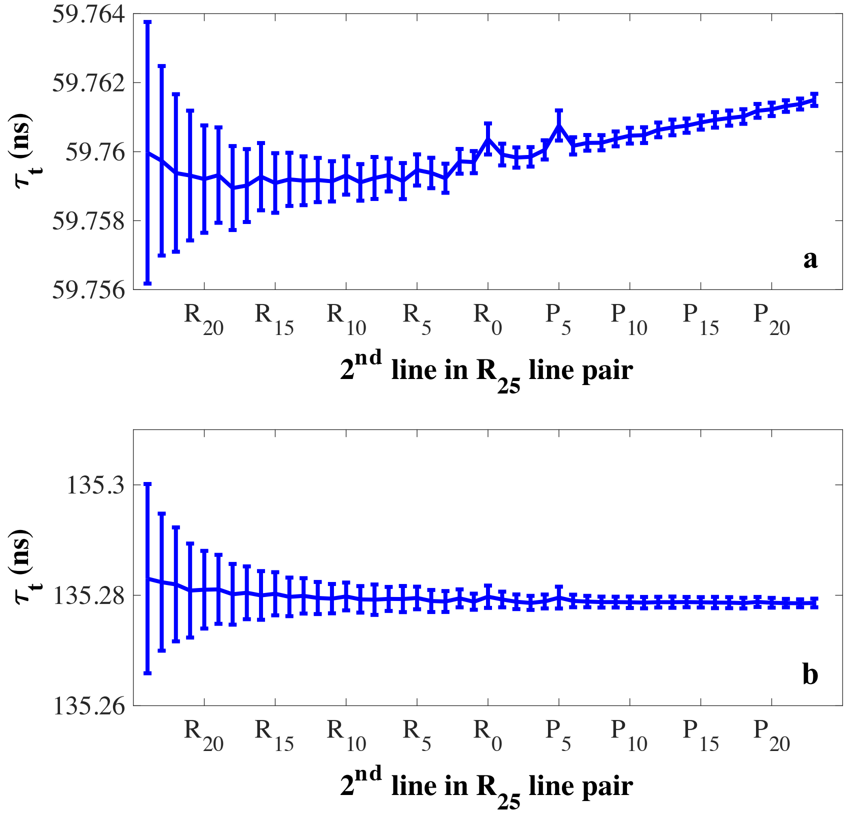

Figure 3.8 (a) Trigger delay time measured using a series of HCN absorption line pairs (a) in a trigger interferometer comprised entirely of SMF-28 optical fiber and (b) in a trigger interferometer in which the physical path length difference is one-third dispersion-compensating fiver and two-thirds SMF-28. Error bars represent 2σ uncertainty.

In a trigger interferometer with non-zero dispersion, DFT bin size is proportional to the mean value of trigger delay time $\overline{\tau_t}$ over the course of the entire laser sweep—

$$s_\tau = \frac{\overline{\tau_t}(\nu)}{M}. \tag{3.16}$$

Unfortunately, hydrogen cyanide absorption lines only span the 1528 nm to 1564 nm wavelength range, while the laser sweeps used for the experimental work described in this chapter use wavelengths from 1500 nm to 1570 nm. With exact knowledge of the mean group refractive index of SMF-28 over a given wavelength range, the value of DFT bin size may still be obtained from

$$s_\tau = \overline{\tau_t}(\Delta\nu_{HCN}) \frac{\overline{n_g}(\Delta\nu_{meas})}{\overline{n_g}(\Delta\nu_{HCN})}, \tag{3.17}$$

where $\overline{\tau_t}(\Delta\nu_{HCN})$ is the mean value of trigger delay time between two HCN absorption line wavelengths, $\overline{n_g}(\Delta\nu_{HCN})$ is the mean group refractive index of optical fiber between those two wavelengths, and $\overline{n_g}(\Delta\nu_{meas})$ is the mean group refractive index over the wavelength range of the SWI measurement.

Mean group refractive indices for fused silica can be calculated [51] using Sellmeier coefficients for SMF-28 [108], wavelength and temperature dependent thermo-optic coefficients for fused silica [109], and a computational model for the group refractive index of air. Reliable models for calculating the refractive index of air have been developed by Ciddor [110] and Edlén [111] [112] [113], although Ciddor's model is considered more accurate over a wider range of atmospheric conditions [114]. However, the exact uncertainties of these calculations are unknown, meaning that the uncertainty analysis of Equation (3.15) may cease to be reliable for a trigger interferometer with non-zero dispersion.

To qualitatively evaluate the accuracy of Equation (3.17), I used the measured trigger delay times plotted in Figure 3.8a to calculate the physical path length difference between the arms of the trigger interferometer. For any trigger delay time τ_t measured using a single pair of HCN absorption lines, the physical path length difference d_t is given by

$$d_t = \tau_t \frac{c_0}{\overline{n_g}(\Delta\nu_{HCN})}. \tag{3.18}$$

The value of $\overline{n_g}(\Delta\nu_{HCN})$, the mean group refractive index of SMF-28 between wavelengths of the HCN absorption line pair, was calculated Sellmeier coefficients for SMf-28, thermo-optic coefficients for fused silica, and Ciddor's model for the refractive index of air. The resulting values of d_t are plotted in Figure 3.9. For all but the R_0 absorption line, the 2σ uncertainty bars overlap, providing convincing, albeit qualitative, confirmation that Equation (3.17) may be used to obtain an accurate measure of DFT bin size, despite the effects of dispersion in the trigger interferometer.

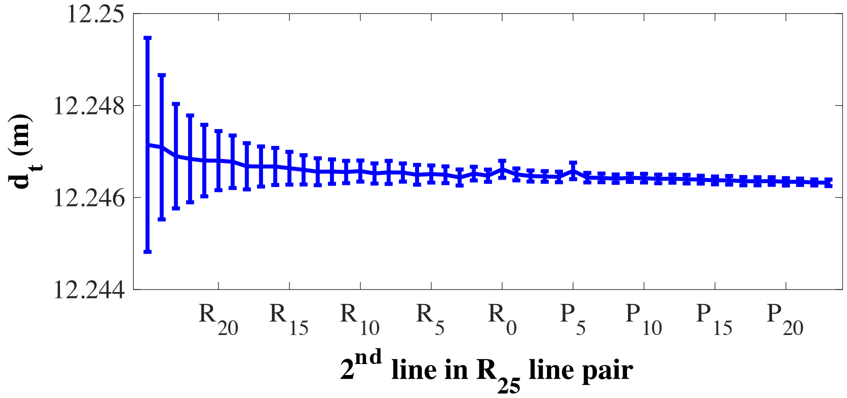

Figure 3.9 Physical path length difference d_t *of the trigger interferometer, measured using a series of HCN absorption line pairs. Physical path length was obtained from measured trigger delay time by calculating the mean group refractive index of SMF-28 between HCN line pairs. Error bars represent* 2σ *uncertainty.*

3.1.5 Temperature drift

Fiber-based SWI systems are extremely sensitive to changes in temperature—this has allowed them to be used as high precision temperature sensors in fiber networks [16] [13] [115] [17] [116], as well as in more exotic environments, such as in extreme low-temperature [117] or radioactive environments [118] [119]. Unfortunately, the same sensitivity that renders the measurement interferometer such an effective temperature sensor can also degrade measurement accuracy if temperature variations are allowed to affect the trigger interferometer.

If the temperature of the trigger interferometer is constant, the contribution $u(p)$ to uncertainty from the fringe period count is comparatively small, and uncertainty in trigger delay time is dominated by the uncertainty $u(\Delta\nu_{HCN})$ in frequency spacing between the absorption line pair chosen for calibration. However, trigger delay time is extremely sensitive to temperature fluctuations in the trigger interferometer. For small temperature changes, the temperature dependent change Δp in fringe period count is given by

$$\Delta p \approx \tau_t \Delta\nu_{HCN} \Delta T \left(\alpha_L + \frac{1}{n_g} \frac{dn}{dT} \right), \tag{3.19}$$

where $\alpha_L = 0.52\times10^{-6}$ is the coefficient of thermal expansion for Corning SMF-28 fiber, $n_g = 1.462893$ is the fiber's group index at 1550 nm, $dn/dT = 7.97\times10^{-6}$ is the fiber's thermo-optic coefficient, and ΔT is the change in temperature from 25 °C. If this temperature dependent change in trigger delay time is not eliminated or otherwise accounted for, it adds uncertainty to the fringe count p, according to

$$u(p) = u_{fit}(p) + \Delta p\,, \tag{3.20}$$

where $u_{fit}(p)$ is the uncertainty in the Lorentzian fits to HCN absorption lines, and Δp is the temperature dependent change in the fringe period count, given by Equation (3.19).

Figure 3.10 shows the temperature dependent change in 1σ DFT bin size uncertainty $u(s_\tau)$. A 0.02 °C temperature increase causes a 0.3% increase in uncertainty, and a 0.1 °C increase results in a 2.9% increase in uncertainty. Consequently, temperature change during any single measurement (i.e. during any one laser sweep) must be minimized in order to minimize overall measurement uncertainty.

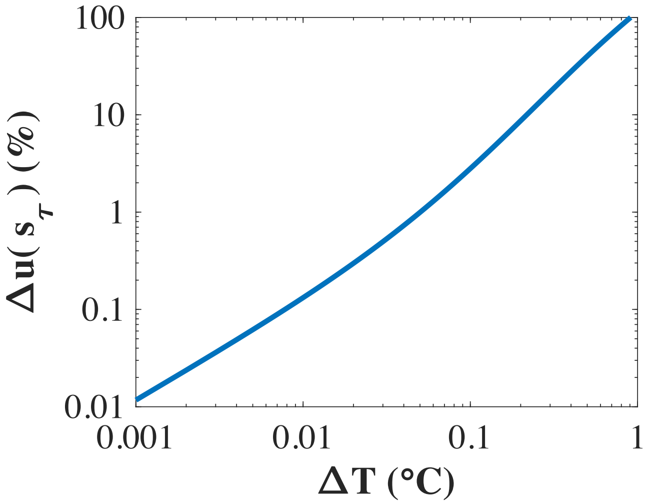

Figure 3.10 Temperature change in the trigger interferometer increases uncertainty in DFT bin size. For this figure, uncertainty in absorption line spacing was derived from the 40 fm and 75 fm 1σ *wavelength uncertainties of the R20 and P18 absorption lines of a Wavelength References HCN gas reference cell.*

Figure 3.11 shows a series of 4,400 measurements of trigger delay time in the SWI system from Figure 3.5. During the 4.5 hour measurement period, the temperature of the aluminum block housing the trigger interferometer was monitored and recorded. The aluminum housing was clamped to a hot plate which was stepped in temperature in two 0.5 °C increments. Both the temperature of the aluminum block and the trigger delay time rapidly increased when the hot plate temperature was increased.

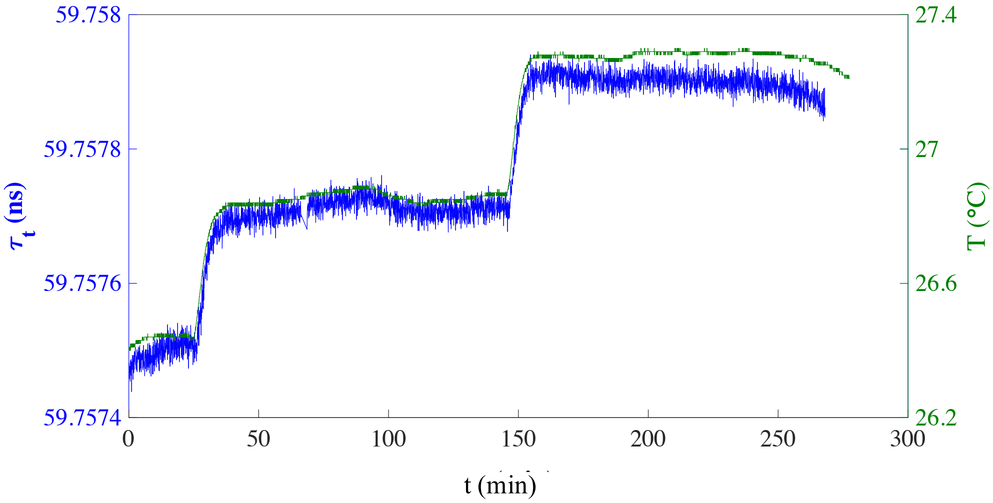

Figure 3.11 A series of 4,400 measurements of trigger delay time taken over a 4.5 hour period illustrate the strong temperature-dependence of trigger delay time. The left y-axis shows measured trigger delay time, and the right y-axis shows the measured temperature of the aluminum housing.

During the entire series of measurements, the maximum rate of temperature change during a single laser sweep was less than 0.02 °C, resulting in a maximum temperature-dependent change in the number of fringe periods of less than 0.02 periods. The maximum fringe period uncertainty $u(p)$, from both the temperature change and line fit uncertainty, is therefore less than 0.06.

The mean rate of temperature change during the series of measurements was $4.3\text{x}10^{-5}$ °C/s. Excluding measurements immediately following a temperature step, 1σ variation in measured trigger delay time was approximately 11.5 fs, consistent with the 10 fs variation predicted using Equation (3.15), the average uncertainty of all 8,800 HCN line fits, and the mean fringe period uncertainty due to temperature variation in the trigger interferometer. These results are consistent with the prediction from Equation (3.19) that for the SWI measurements to reach theoretical uncertainty limits, the temperature of the trigger interferometer must be stabilized at the 0.01 – 0.1 °C level for at least the duration of each measurement.

3.1.6 Sweep nonlinearity

For the numerical work in Chapter 2, I assumed that samples of the signal $U(\nu[t])$ were evenly spaced in optical frequency. For a triggered system, this assumption is quite good if the slow-tuning approximation holds. However, the trigger interferometer can, in general, only compensate zeroth and first order variation in the laser sweep rate [52]. When trigger delay time is carefully matched to electronic delay time (the time delay between the upward zero-crossings of the trigger signal, which I will call trigger signal times, and the times of sample acquisition in the measurement interferometer), second order variations may also be compensated [52].

Here, I examine the effect that laser sweep nonlinearity has on both the accuracy and precision of superresolved SWI measurements in a triggered system. I am indebted to the excellent analysis of Dr. Eric Moore on the effects of sweep nonlinearity on measurement precision [51] [52]; it is his work that I build upon in this section.

First, I examine a simplified example that illustrates how sweep nonlinearity can degrade measurement accuracy. Consider a laser sweep in which the rate of change of optical frequency $d\nu/dt$ equal to a monotonically increasing or decreasing function. A common example is a laser sweep rate that is constant as a function of wavelength, i.e.

$$\frac{d\lambda}{dt} = constant\,. \tag{3.21}$$

In this case, the sweep rate as a function of frequency is not constant (Equation (3.27)), but rather

$$\frac{d\nu}{dt} = -\frac{\nu^2}{c}\frac{d\lambda}{dt}, \tag{3.22}$$

and optical frequency as a function of lab time is not linear:

$$\nu(t) = \left[\frac{1}{\nu_0} + \frac{1}{c}\frac{d\lambda}{dt}t\right]^{-1}. \tag{3.23}$$

Here c is the speed of light, and ν_0 is optical frequency at the start of the laser sweep. A simplified form of this same equation is

$$\nu(t) = \frac{1}{1+t}, \tag{3.24}$$

and its inverse is

$$t(\nu) = \frac{1-\nu}{\nu}. \tag{3.25}$$

In Figure 3.12a, a series of trigger signal times are plotted in blue. The corresponding values of optical frequency are all equally spaced (left y-axis). A 0.1 s delay between trigger signal times and sample acquisition times, plotted in red, causes acquired samples to be unevenly spaced in optical frequency (right y-axis). Additionally, the mean value of optical frequency spacing for acquired samples is changed (reduced, in this example). The longer the delay between trigger signal times and sample acquisition times, the more dramatic these effects become (Figure 3.12b).

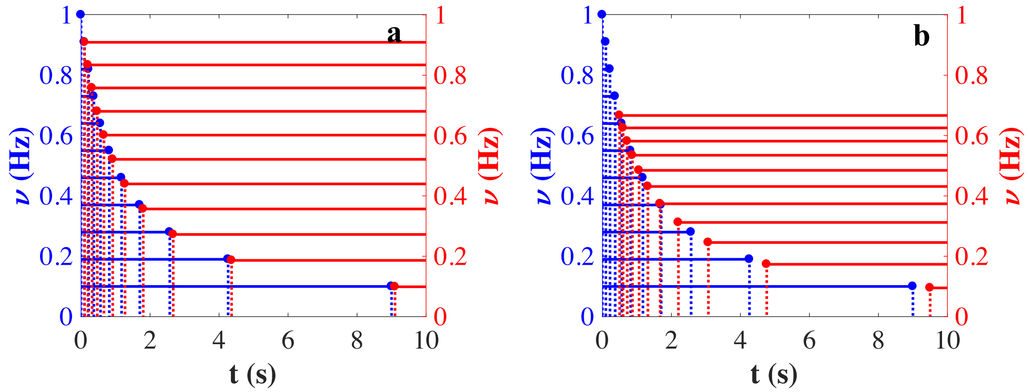

Figure 3.12 Effects on optical frequency spacing for (a) 0.1 s of electronic delay and (b) 0.5 s of electronic delay.

Even in this simplified example, the expression of Equation (3.16) for DFT bin size fails to hold, and the analysis of [52] shows that this expression for DFT bin size is always approximate (although as the results of Figure 3.14 will show, the approximation can be a very good one). A more exact expression for DFT bin size can be obtained by noting that laser sweep bandwidth is equal to the sum of all the frequency sampling intervals $\delta\nu_m$ across a laser sweep. The exact value of DFT bin size is then given by the mean value of the following inverse probability distribution function (pdf):

$$f_{s_\tau}(s_\tau) = \frac{1}{Ms_\tau^2} f_{\delta\nu}\left(\frac{1}{Ms_\tau}\right) \ , I_{(0,\infty]}(s_\tau) \,. \tag{3.26}$$

Here the pdf for DFT bin size f_{s_τ} is a function of the pdf $f_{\delta\nu}$ for sample spacing in optical frequency and is defined on the interval $(0,\infty]$. Unfortunately, the pdf for optical frequency spacing is unknown (and is likely to be unique for each tunable laser source and perhaps even to each laser sweep). The mean μ_{s_τ} and variance $\sigma_{s_\tau}^2$ of DFT bin size can, however, be obtained approximately from estimates as

$$\overline{\mu_{s_\tau}} = \frac{1}{\sum_{m=1}^{M} \delta\nu_m} \tag{3.27}$$

and

$$s_{s_\tau}^2 = \frac{1}{M-1}\sum_{m=1}^{M}\left(\frac{1}{M\delta\nu_m} - \overline{\mu_{s_\tau}}\right)^2 \,. \tag{3.28}$$

Following the analysis in [52], the frequency spacing intervals $\delta\nu_m^t$ between trigger times are given by

$$\delta\nu_m^t = \tau_t^{-1} + \eta_m^I \,, \tag{3.29}$$

where η_m^I, the intrinsic errors in the frequency intervals between trigger times due to laser tuning rate variation, are given by

$$\eta_m^I = -\sum_{a=2}^{\infty} \frac{\tau_t^{a-1}}{a!}\left[\nu^{(a-1)}(t_m) - \nu^{(a)}(t_m)\right] . \tag{3.30}$$

The frequency intervals between samples in the measurement interferometer are given by

$$\delta\nu_m^{meas} = \tau_t^{-1} + \eta_m^I + \eta_m^D \,. \tag{3.31}$$

The additional error term η_m^D comes from electronic delay and is given by the infinite series

$$\eta_m^D = \sum_{a=1}^{\infty} \frac{\tau_D^a}{a!}\left[\nu^{(a)}(t_{m+1}) - \nu^{(a)}(t_m)\right], \tag{3.32}$$

where τ_D is electronic delay time.

The values of $\delta\nu_m^t$ and $\delta\nu_m^{meas}$ depend uniquely on laser sweep rate and trigger delay time, and it is not possible to obtain a general solution for the mean and variance of DFT bin size, or for bias in DFT bin size, for all tunable laser sources. Instead of a general solution, I present a numerical method for obtaining these values for any measured laser sweep rate, and demonstrate this method for the measured sweep rate of an Agilent 81680A tunable laser.

Figure 3.13 shows the measured sweep rate of an Agilent 81680A tunable laser from 1500 nm to 1570 nm. The laser sweep rate is nominally 40 nm/s, or approximately -5 THz/s, and the laser sweep was sampled at a 1 MHz sampling rate, resulting in an average frequency spacing between samples of approximately 5 MHz.

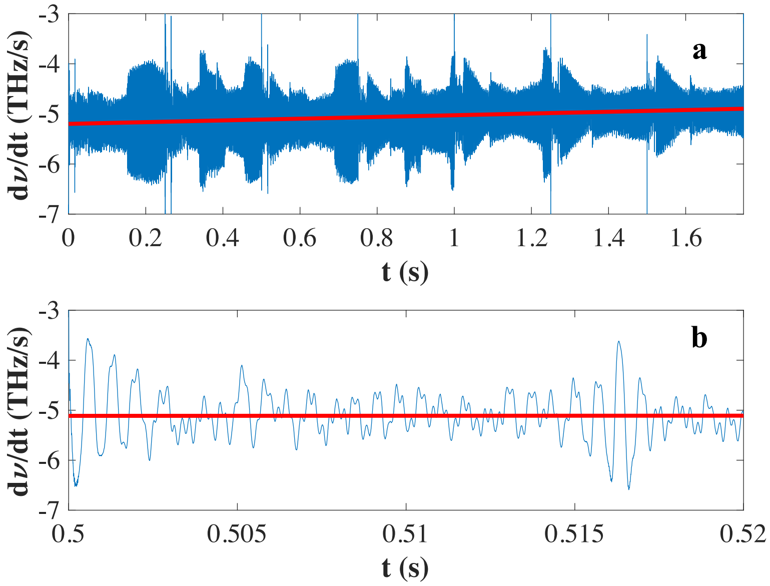

Figure 3.13 Measured frequency sweep rate (blue lines) of an Agilent 81680A tunable laser. The mean sweep rate is plotted in red. (a) The sweep rate was measured from 1500 nm to 1570 nm in 10 nm sections. The large variations in sweep rate at the beginning and end of each of these sections would not be present in a continuous sweep. (b) Close-up view of a small portion of the laser sweep.

Using the measured sweep rate of the laser, the phase of the output of the trigger interferometer is given by numerically evaluating the expression (again, from [52])

$$\phi(t+\tau_t)-\phi(t)=2\pi\nu(t)\tau_t+2\pi\sum_{a=2}^{\infty}\frac{\tau_t^a}{a!}\nu^{(a-1)}(t) \tag{3.33}$$

up to sixth order. (Note that sampling density in measured laser rate must be high enough that errors are not accumulated by interpolating or by taking numerical derivatives.) This expression is then interpolated and solved for the trigger signal times t_m when phase is equal to an integer multiple of 2π. The frequency intervals $\delta\nu_m^t$ between trigger signal times are obtained by evaluating Equation (3.29) and Equation (3.30) up to sixth order. Finally, the frequency intervals $\delta\nu_m^{meas}$ between samples in the measurement interferometer are obtained from evaluating

Equation (3.31), Equation (3.30), and Equation (3.32) up to sixth order. (For the measured tuning rate from Figure 3.13, third and higher order terms make negligible contributions to these computations, but additional orders add little computational burden to the computational method.)

From the computed measurement interferometer frequency intervals $\delta\nu_m^{meas}$, values for the mean and variance of DFT bin size can be obtained from Equation (3.27) and Equation (3.28), respectively. Normalized bias in DFT bin size is then given by

$$b = \frac{\left|\overline{\mu_{s_\tau}} - \tau_t^{-1}\right|}{\tau_t^{-1}}. \tag{3.34}$$

For the laser sweep rate from Figure 3.13, Figure 3.14 shows the normalized values of standard deviation and bias in DFT bin size for a range of trigger delay times and electronic delay times. When trigger delay time is twice electronic delay time, second order error terms cancel, and both standard deviation and bias are minimized [52].

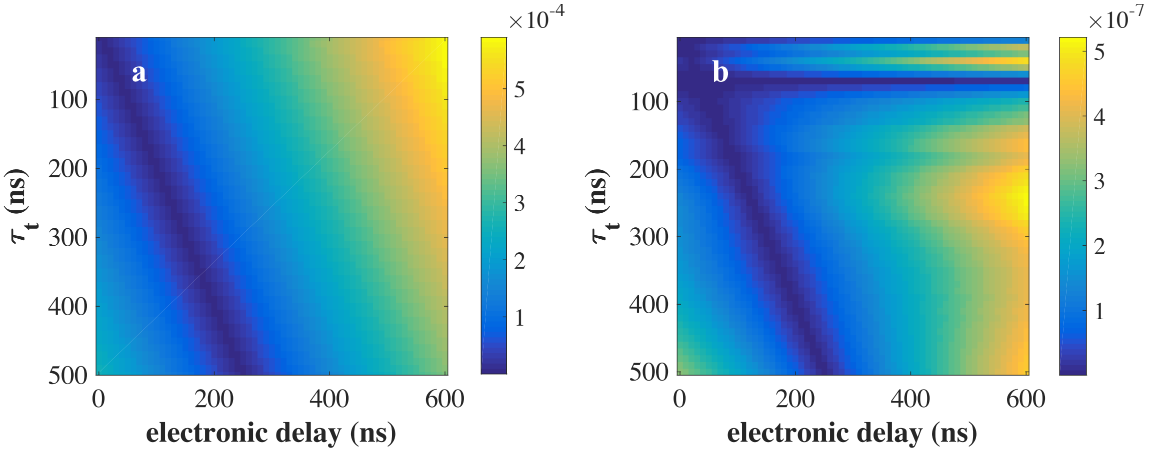

Figure 3.14 (a) Normalized standard deviation in DFT bin size as a function of trigger delay time τ_t and electronic delay time. (b) Normalized bias in DFT bin size.

3.2 Experimental Accuracy of Superresolved Swept-Wavelength Interferometry

The analysis and experimental work from this chapter suggest that the theoretical limits delineated in Chapter 2 may be obtainable under properly controlled experimental conditions. Specifically, laser power fluctuations must be compensated, trigger and measurement interferometers must be dispersion-matched, dispersion in the trigger interferometer must be included in the calibration of trigger delay time, the temperature of the trigger interferometer must be stabilized, and trigger delay time should equal roughly twice the value of any electronic delay in order to control the effects of laser sweep rate nonlinearity. An SWI system designed to meet these conditions is depicted in Figure 3.15.

The tunable laser used here is an Agilent 81680A external cavity laser, set to sweep from 1500 nm to 1570 nm at a 40 nm/s sweep rate. The first optical coupler in the SWI system delivers 5% of the laser output to a photodetector set to monitor and record laser power during the sweep. The trigger interferometer is composed entirely of SMF-28 fiber. With approximately 10 m of additional fiber in the longer arm of the interferometer, trigger delay time is around 100 ns. Before the measurement interferometer, 8 m of fiber provide enough additional electronic delay to cancel the effects of laser sweep nonlinearity.

In the measurement interferometer, a polarization diverse detection scheme is used to prevent fringe fading[3]. Instead of a collimating lens, the sample arm of the measurement interferometer is terminated by a cleaved fiber end, polished at a 0° angle. This fiber end is the

---

[3] The polarization diverse detection system depicted in Figure 3.15 could be further improved by the addition of a polarization controller in the reference arm of the measurement interferometer. By using a polarization controller to ensure equal power levels of S and P polarizations in the reference arm, polarization fringe fading can be minimized, rather than simply mitigated.

terminus of one channel in a 32-channel silicon v-groove array manufactured by Oz Optics Ltd. The aluminum housing that enclosing the majority of the SWI system is clamped to a hot plate which is set to maintain a temperature of 29 °C, a few degrees C above the ambient temperature in the laboratory.

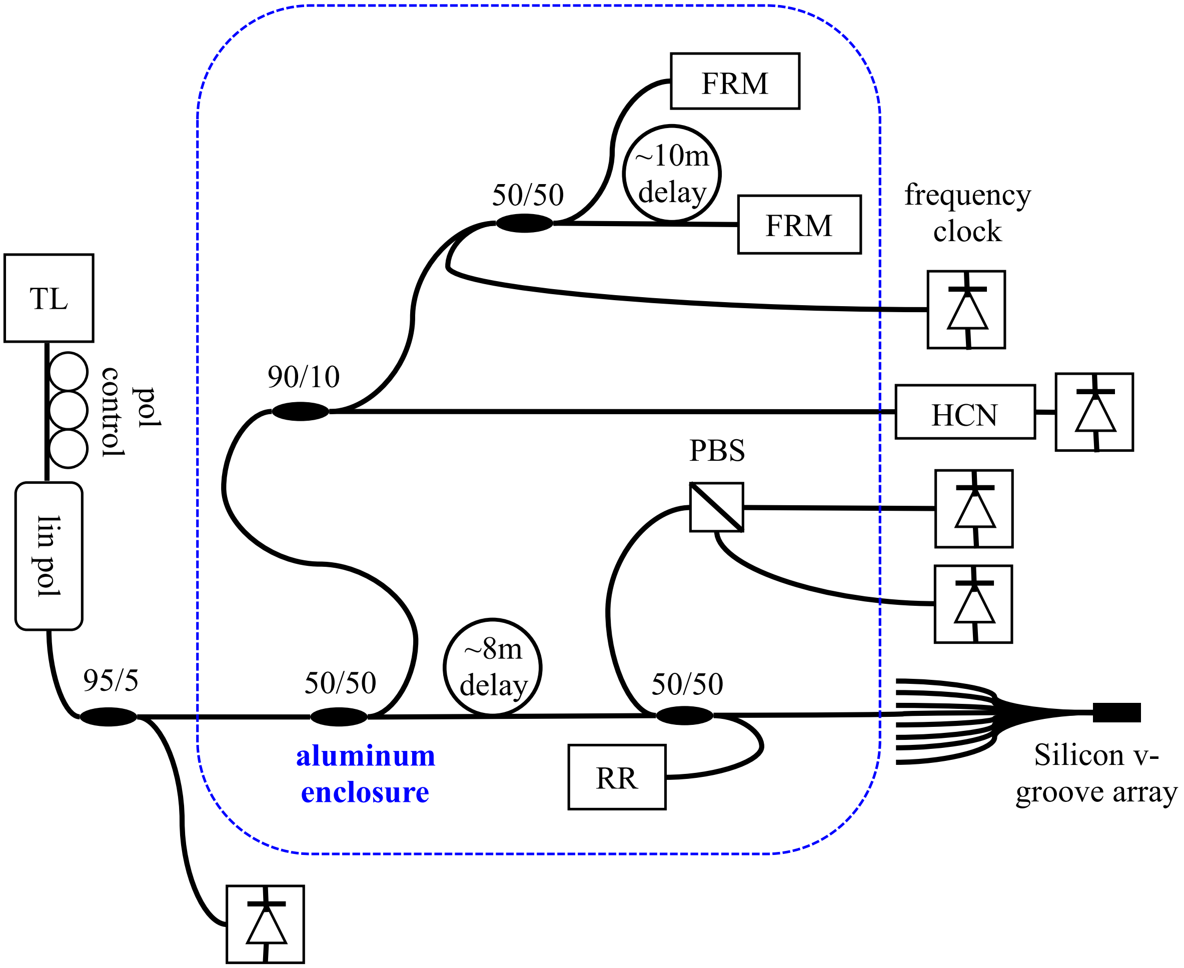

Figure 3.15 System diagram for the SWI experiments described in Section 3.2.. For coupling ratios noted in this figure, the first number gives the percentage of power delivered to the upper of the two output fibers. TL = tunable laser, FRM = Faraday rotator mirror, lens, RR = retroreflector, PBS = polarization beam splitter.

In Chapter 2, the uncertainty limit for estimates of the delay time between two equal amplitude reflectors was shown to be a function of DFT bin size uncertainty, reflector separation, and estimator bias (Figure 2.10). The precision limit for delay time estimates is determined by SNR and, for some estimators, by reflector separation (Figure 2.20). While the precision limits predicted in Chapter 2 are in good agreement with a number of earlier experimental results ([33] [21] [34]), to my knowledge, no similarly convincing experimental work confirms the accuracy[4] of superresolved SWI across a DFT bin.

The experimental work presented here quantifies the magnitude of measurement bias across the span of approximately three DFT bins. Experimentally confirming the accuracy of the DFT bin size calibration is a much more difficult problem, requiring a reference standard with optical path length both known and temperature stable at the nanometer level. Here, the reference standard is the surface of a 2-inch diameter, $\lambda/20$ ($\pm 15.8\,\text{nm}$) aluminum mirror with a ZERODUR substrate. This mirror was placed at a 1° tilt angle on the polished ends of three 120 threads-per-inch stainless steel adjustment screws and mounted on an x-y-z stage stack (Newport XMS160, XMS100, GTS30V). The silicon v-groove array in the sample arm of the measurement interferometer was suspended by a steel scaffold above the surface of the reference mirror. Translating the mirror in x changes the spacing between the polished fiber end in the silicon v-groove and the surface of the reference mirror (Figure 3.16). The manufacturer specified maximum stage pitch error of 100 μrad gives a maximum 6 pm distance error from the stage stack.

---

[4] A clarification on accuracy and uncertainty: uncertainty is a prediction of how likely a measured quantity is to be within some range of the true value of that quantity. For example, 2σ uncertainty provides the 95% confidence interval for the quantity of interest. Accuracy, however, is a measure of how close a measured quantity comes to the value of a reference standard. Depending on the reference standard, accuracy and uncertainty may be related or even equivalent, but in general, this is not the case.

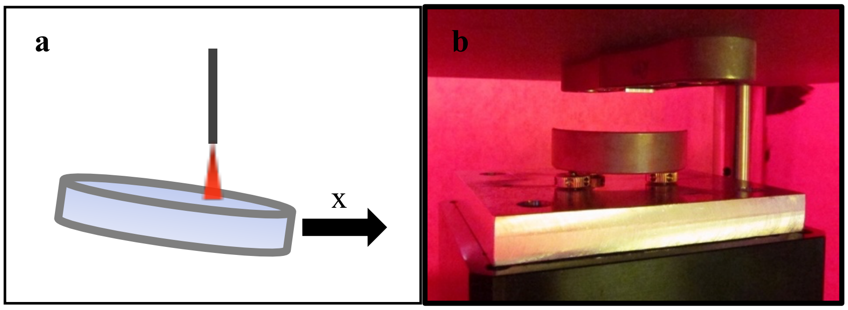

Figure 3.16 (a) Moving a tilted mirror in x *gradually reduces the distance between a polished fiber end and the mirror surface. (b) The fiber end, one channel in a 32-channel silicon v-groove array, is suspended in a steel scaffold above the mirror surface.*

The reference mirror was stepped across 3 mm in 30 µm increments. At each of the 101 *x*-locations, a single SWI measurement of the delay time between the fiber endface reflection and the mirror surface was obtained. This measurement process was then repeated 50 times. A surface-mounted resistance temperature detector affixed to one of the steel scaffold legs recorded the temperature throughout the experiment. Although the OPL of the ~0.5 mm air gap between the silicon v-groove array and the mirror surface is stable to less than 2 nm within a 0.2 °C temperature range, the physical lengths of the ~12 inch tall stage stack and ~14 inch tall steel scaffold certainty are not. Therefore, to minimize the effect of temperature-dependent variation in the air gap between the fiber endface and mirror surface, the distances between the fiber endface and mirror surface were measured in 50 repeated sets of 101 sequential distances, rather than in a series of 101 sets of 50 measurements at each distance.

Figure 3.17 shows mean values for the measured distances between the fiber endface and mirror surface as a function of mirror position *x*. Physical distance *d* was obtained by multiplying the measured time delays by half the vacuum speed of light.

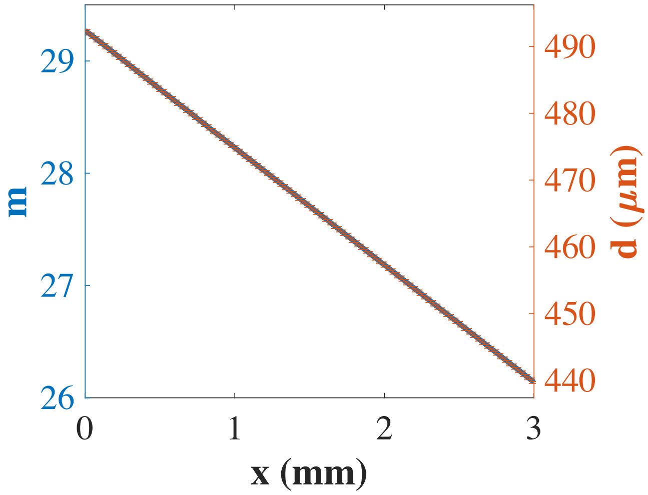

Figure 3.17 Measured times and distances from mirror surface as a function of mirror position x. The left y-axis shows delay time in DFT bins, while the right y-axis shows the corresponding physical distance d. *Physical distance is half the measured round-trip distance between the polished fiber end and the mirror.*

To evaluate the accuracy of sequential distance measurements, a line was fitted to the mean values of measured distances. The residuals between the line fit and mean measured distances are plotted in Figure 3.18. The range of the residuals shown is 62 nm, or 1.8x10^{-3} of a single DFT bin, roughly one order of magnitude larger than the 2σ uncertainty value of 4 nm for two reflectors separated by approximately 30 DFT bins (Figure 2.17).

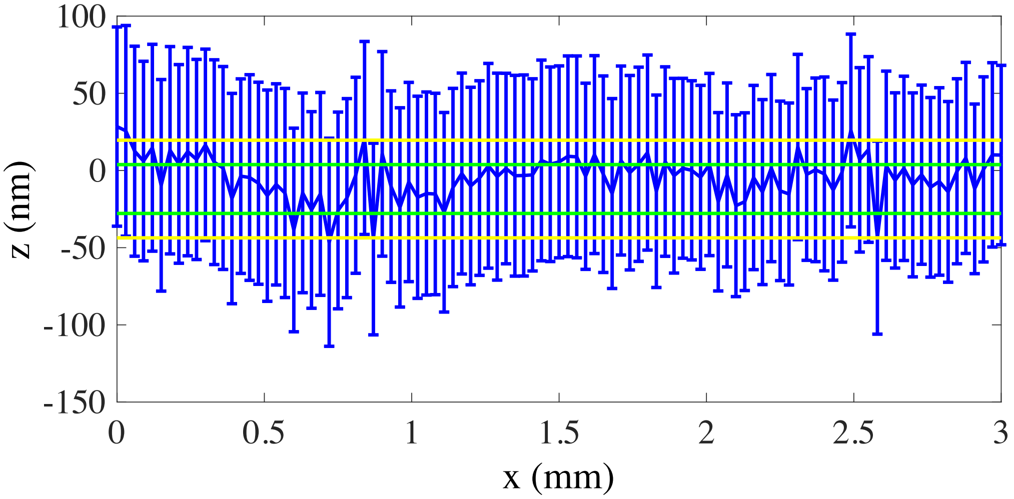

Figure 3.18 Mean and standard deviation of line fit residuals. Green lines show the tolerance for a $\lambda/20$ *result* ($\pm 15.8\ nm$)*, and the yellow lines show the tolerance for a* $\lambda/10$ *result* ($\pm 31.6\ nm$).

The error bars in Figure 3.18 show the 1σ standard deviation of all measured distances at a single *x*-location. The mean value of standard deviation is 135 nm, considerably larger than the ~1 nm theoretical limit (Figure 2.20). This discrepancy is largely due to temperature variation during the experiment. Figure 3.19 shows the line fit residuals for every measurement taken during the experiment along with the measured temperature of the leg of the steel scaffold. The two are clearly correlated. The mean standard deviation for each set of sequential distance measurements (down columns in Figure 3.19) is only 17 nm, considerably closer to the theoretical limit.

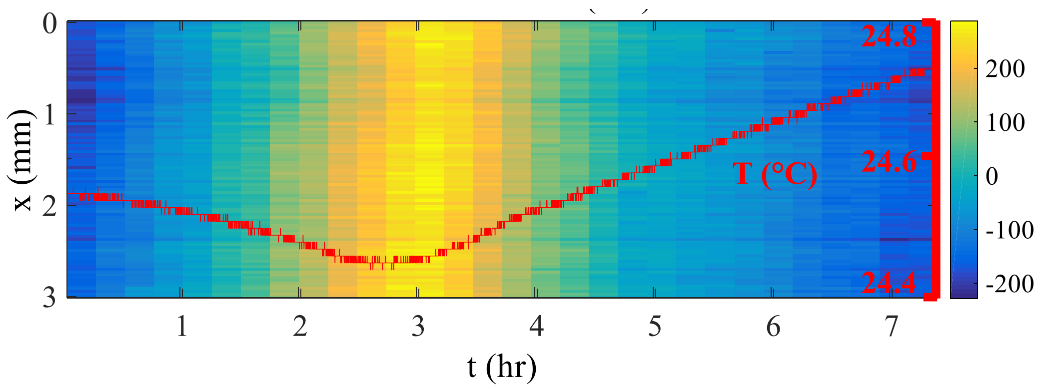

Figure 3.19 Line fit residuals (nm) shown as a function of mirror position x *and approximate measurement time* t*. Temperature of the scaffold leg, a function of time* t*, is overlaid in red.*

3.3 Conclusions

In this chapter, I discussed how six potential sources of systematic error—non-Gaussian noise, spurious delay times arising from unwanted reflections or mechanical vibration, laser power fluctuations, dispersion mismatch between measurement and trigger interferometers, temperature drift in the trigger interferometer, and laser sweep nonlinearity—may prevent superresolved SWI measurements from achieving theoretical accuracy limits. I quantified the effects of mechanical vibration, dispersion mismatch, and temperature drift, and presented methods to quantify the effects of laser power fluctuation and sweep nonlinearity for any measureable laser sweep. Finally, I described a series of experimental SWI measurements of 101 distances, spaced equally through a range of 3 DFT bins. This measurement series had a maximum bias of 62 nm, or $1.8\text{x}10^{-3}$ of the SWI system's transform-limited resolution, roughly one order of magnitude larger than the measurement's limiting uncertainty of 4 nm.

Chapter 4

Three-Dimensional Surface Characterization Using Time-Multiplexed, Superresolved Swept-Wavelength Interferometry

4.1 Background

In this chapter, I present a unique application of superresolved SWI: time-multiplexed three-dimensional (3D) surface metrology. The use of SWI as a surface metrology tool is, of course, not unique. OFDR [51], SS-OCT [120], SD-OCT [121], and FMCW ladar [20] systems have all been used successfully to characterize a variety of three-dimensional surfaces, both specular and diffuse, and ranging in size from microns to meters. These are scanning measurements[5] and rely on stages or scanning mirrors to acquire a succession of 1D measurements that are then agglomerated into full three-dimensional surface measurement. The need for scanning necessarily increases measurement time and may also increase measurement error through errors in stage motion or mirror scanning. By taking advantage of the long coherence lengths available from certain tunable laser sources, time-multiplexed SWI can decrease measurement time [51] and reduce or eliminate the need for scanning in measurements of 3D surfaces.

---

[5] The very similar technique known as wavelength scanning interferometry (WSI) does not rely on mechanical scanning. It is a static swept-wavelength surface measurement technique capable of achieving nanometer-level accuracy across a micron-scale field-of-view [161] [163] [162]. However, it suffers from 2π phase ambiguities at surface steps, and is currently not ideally suited for measurements of steeply-sloped surfaces.

The nanometer-level accuracy and precision of superresolved SWI make a time-multiplexed version of this measurement technique amenable to a difficult and high-interest metrology problem: the 3D characterization of steeply-sloped freeform and aspheric optical surfaces. Freeform and aspheric optics are increasingly being incorporated into optical systems and lens designs [122] [123], yet no completely satisfactory technology exists for measuring the surface profiles of these optics, particularly when they are steeply sloped. Contact measurement systems include mechanical profilometers and coordinate measuring machines (CMMs) [124] [125] [126], but producing a high-resolution surface profile with these systems is relatively slow and can be costly. Non-contact methods include stitching interferometry [127] [128], phase measuring deflectometry [129] [130] or other structured illumination methods [131] [132] [133] [134], optical profilometry [135], and various combinations of these techniques [136] [137]. Among these, optical profilometry provides the highest-accuracy measurements of steeply sloped and arbitrarily shaped surfaces, but it is a scanning measurement and thus limited in measurement speed.

Interferometric systems incorporating computer generated holograms (CGHs) [138] [139] [140] have also been used to characterize both aspheric and freeform optical surfaces, with recent systems reporting peak-to-valley wavefront errors on the order of $\lambda/10$ [141] to $\lambda/20$, or even less [142]. However, the accuracy of these systems is generally limited by the quality of the CGH null corrector; as the maximum slope of the measured surface increases, the spatial frequency content of the CGH must also increase, with corresponding increases in manufacturing costs and potential decreases in CGH accuracy [143].

A novel system designed to measure the interior surfaces of small, concave objects used an array of optical fibers—a single-mode emitter and 8 multi-mode collectors—to measure reflected power as a function of angle and thus deduce the surface shape [144]. Preliminary experiments have demonstrated the feasibility of such a system but, so far, have not demonstrated the capability of such a system to make high precision measurements of complex surfaces [145].

Finally, a SS-OCT system used to measure the surface profiles of machined metal spheres [146] and aspheric lenses [147] demonstrated lateral resolution of 18 μm, axial resolution of 12 μm, and most importantly, the ability to measure sample surface slopes of up to approximately 83 degrees. This was a scanning system with transform-limited axial resolution, but it demonstrates the capability of SWI to measure 3D surface profiles of steeply-sloped and aspheric objects.

In this chapter, I begin with an analysis of system design considerations for a time-multiplexed, superresolved SWI system. I then describe the calibration and resolution limits of such a system. Next, I present an algorithm for surface reconstruction from an array of measured delay times. After presenting and analyzing experimental results from an 8-channel, time-multiplexed SWI system, I conclude with a discussion of the needs for further development of both the SWI system and the surface reconstruction algorithm.

4.2 System Design

4.2.1 Time multiplexing

Time-multiplexed SWI is conceptually straightforward. The unambiguous range of the SWI system is distributed among several channels; this allows simultaneous, parallel SWI measurements from each channel in the system. Experimentally, this is accomplished by splitting the sample arm of the measurement interferometer into separate channels and constructing each channel from different physical lengths of optical fiber. This is depicted in Figure 4.1. Only the second half of the total unambiguous range τ_{max} (equal to half the trigger delay time[6] τ_t) of the system can be assigned to measurement channels, since the maximum separation between reflections in delay time sets the delay time spacing between DC and the cross-term with the highest delay time.

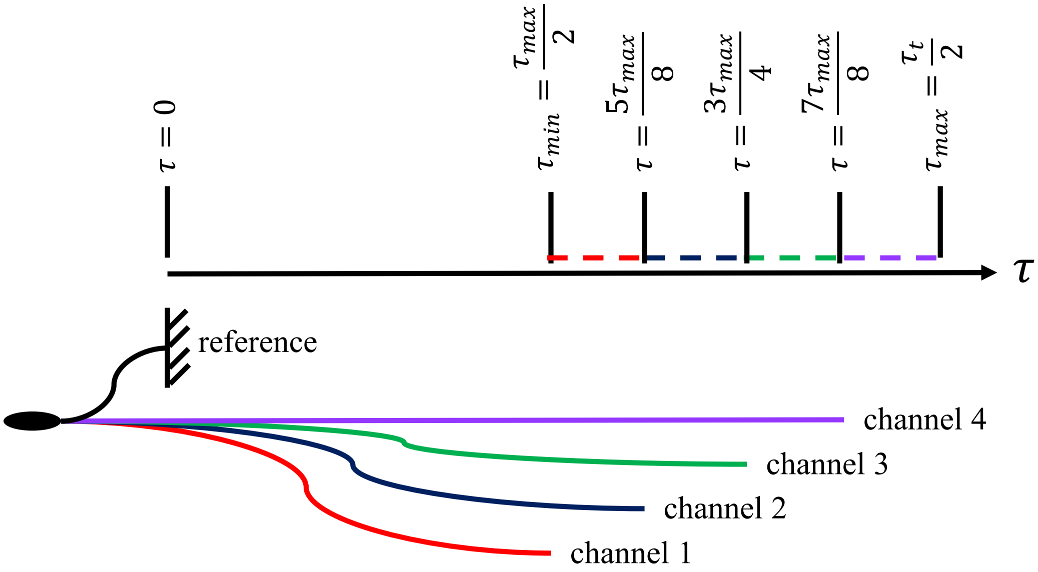

Figure 4.1 In a 4-channel time-multiplexed SWI system, the signal in the measurement interferometer is split into a reference arm and four channels in the sample arm. The minimum physical path length mismatch between the reference arm and each sample channels sets the minimum delay time that can be measured by that channel.

Figure 4.2 shows the system diagram for the time-multiplexed SWI system used for the experiments described in this chapter. The tunable laser source is an Agilent 81680A external cavity laser, set to sweep from 1525 nm to 1580 nm at a sweep rate of 40 nm/s. The effective

---

[6] In an SWI system using a trigger interferometer, trigger delay time sets the spacing between samples in optical frequency, and therefore, through the Fourier transform relation, the maximum measurable (unaliased) delay time.

linewidth of this laser is roughly 100 kHz, giving a coherence time of approximately 10 μs [148], substantially longer than the approximately 50 ns unambiguous range set by the trigger delay time.

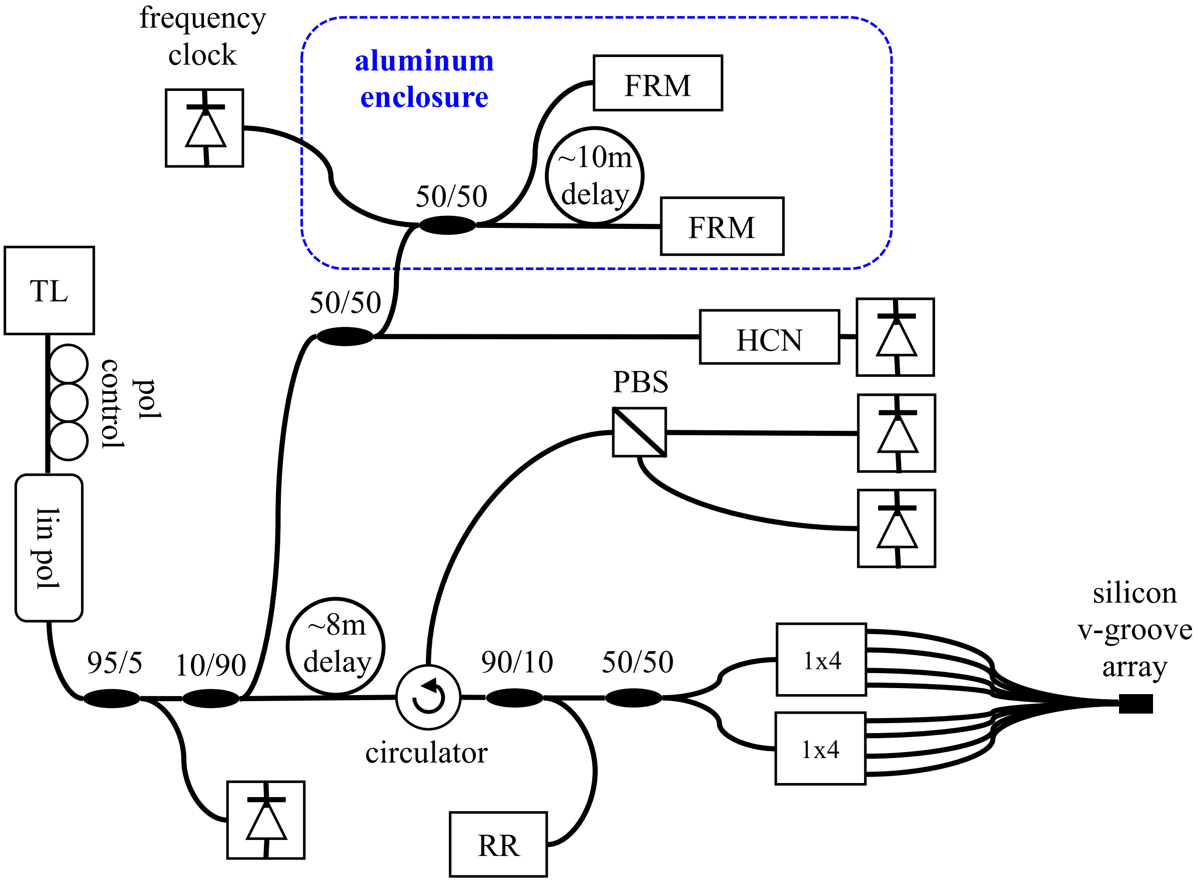

Figure 4.2 System diagram for the SWI experiments described in Chapter 4. For coupling ratios noted in this figure, the first number gives the percentage of power delivered to the upper of the two output fibers. TL = tunable laser, FRM = Faraday rotator mirror, PBS = polarization beam splitter, RR = retroreflector.

The sample arm of the measurement interferometer is divided into eight channels, each terminated at a cleaved fiber end polished at a 0° angle. These fiber ends are housed in a 32-channel silicon v-groove array (shown in Figure 4.3) with 500 μm spacing between each fiber core. The aluminum housing enclosing the trigger interferometer was clamped to a hot plate which was set to maintain a temperature of 27 °C.

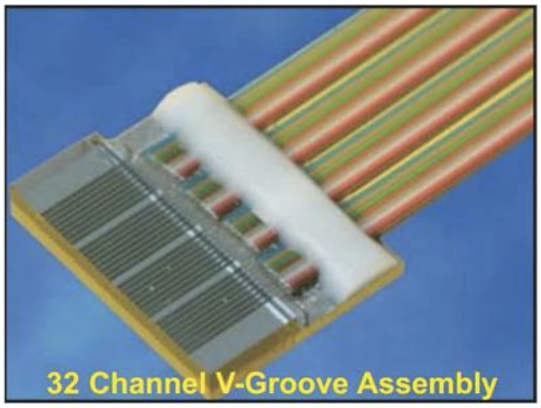

Figure 4.3 32-channel silicon v-groove assembly from Oz Optics, Ltd [149]. Spacing between fiber cores is 250 μm, or 500 μm between sets of 8 fibers.

Data from a single laser sweep is plotted in Figure 4.4. The eight peaks at delay times between 25 ns and 50 ns correspond to reflections from each of the polished fiber ends in the silicon v-groove array. The minimum delay time between any two channels is 1.29 ns, meaning the maximum unambiguous range of this time-multiplexed SWI system is approximately 19 cm.

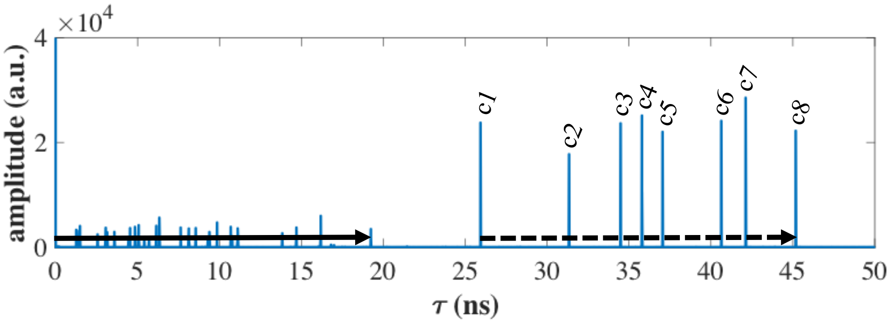

Figure 4.4 Reflections from the polished fiber ends of each channel in the 8-channel, time-multiplexed SWI system appear at different delay times τ. The maximum delay time for any cross term (solid arrow) is equal to the maximum delay time difference between any two reflectors (dashed arrow).

4.2.2 Maximizing SNR

Because the power returned from each channel in a time-multiplexed system is equal to the inverse of the total number of channels, maintaining adequate SNR is a primary concern in the design of a time-multiplexed SWI system. In the SWI system used for the experiments described in Chapter 3, power in the measurement interferometer was split evenly between reference and sample arms of the interferometer (Figure 3.15), meaning that the maximum power returned from the sample arm of the interferometer is one-fourth of the input power.

In an 8-channel system, each channel will return a maximum of one sixty-fourth of the power input to the sample arm. Based on the analysis in [51], the SNR limit for the SWI system used here is set by quantization noise. Consequently, maximizing interference fringe contrast is more necessary than maximizing total power in the interferogram[7].

---

[7] Section 4.2.2.1 describes how to maximize contrast by adjusting the coupling ratio between sample and reference arms of the measurement interferometer. An alternative, and likely superior, approach would be to first maximize total signal power by using 50:50 coupling ratio between arms of the interferometer, and to subsequently maximize contrast by removing the DC offsets from the electronic signals immediately following the S and P photodetectors.

4.2.2.1 Maximizing contrast

Figure 4.5 shows a system diagram for a simplified SWI system. The input electric field amplitude E_0 is constant as a function of optical frequency, and the polarization of the input field remains unchanged as it propagates through the system. A fiber coupler with power coupling ratio a separates the input electric field into reference and sample arms, with electric field amplitudes

$$E_r = \sqrt{a}E_0 \tag{4.1}$$

and

$$E_S = \sqrt{1-a}E_0 \tag{4.2}$$

respectively. In the reference arm, a mirror reflects 100% of the electric field E_r back to the optical coupler. The sample arm contains a single reflector with reflectivity R_s.

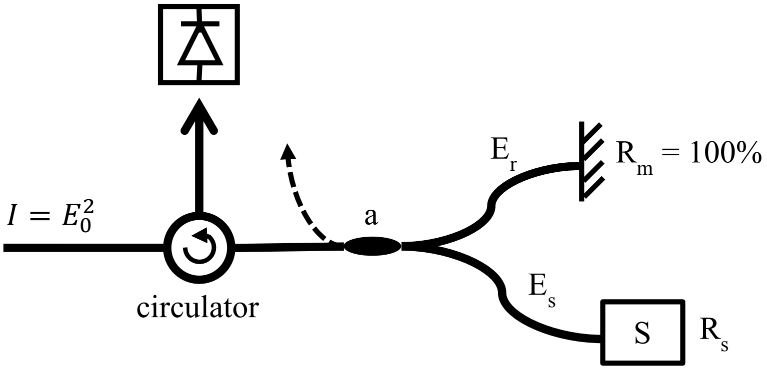

Figure 4.5 Simplified SWI system diagram. Input intensity electric field E_0 *is constant as a function of optical frequency. Reference reflectivity* R_m *is 100%. A single reflector in the sample arm of the interferometer has reflectivity* R_S. *The unused output port of the optical coupler is depicted as a dashed line.*

At the photodetector, the contrast C of the detected interferogram is given by

$$C = \frac{2a(1-a)\sqrt{R_s}}{a^2 + (1-a)^2 R_s} \tag{4.3}$$

and is a function of both[8] the optical coupling ratio *a* and sample reflectivity R_s [148]. This is shown in Figure 4.6.

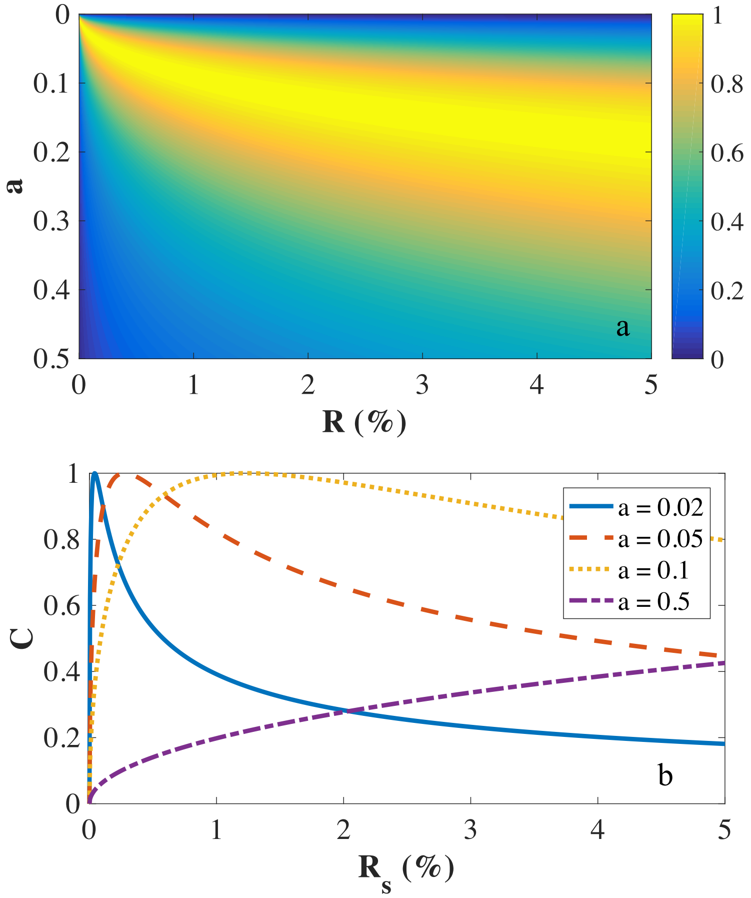

Figure 4.6 (a) Contrast C *as a function of coupling ratio* a *and sample reflectivity* R_S. *(b) Contrast as a function of sample reflectivity at four common coupling ratios.*

---

[8] Here, because the same port of the optical coupler is used for both input and output, contrast is a function of both coupling ratio and sample reflectivity. If the unused output port of the coupler delivered the interference pattern to the photodetector, contrast would be a function only of sample reflectivity, and the best possible choice of coupling ratio *a* would be 0.5.

Establishing an arbitrary minimum contrast value of 80% gives the minimum and maximum sample reflectivites for any coupling ratio *a*. These values are listed in Table 4.1 for a range of common coupling ratios.

Table 4.1 Maximum and minimum sample reflectivity R_S *that provide at least 80% contrast at coupling ratio* a.

a	**min R_S (%)**	**max R_s (%)**
0.02	1.0×10^{-2}	1.6×10^{-1}
0.05	7.0×10^{-2}	1.1
0.1	0.3	4.9
0.5	25.0	100.0

4.2.2.2 Experimental measurement of SNR as a function of coupling ratio

SMF-28 optical fiber has a numerical aperture (NA) of approximately 0.14, meaning that the Rayleigh range of the beam emitted from a cleaved fiber end is approximately 25 µm at 1550 nm, and the divergence half-angle of the beam is approximately 8° [148]. In the time-multiplexed SWI system of Figure 4.2, each channel is terminated at a cleaved, polished fiber end. Consequently, the apparent reflectivity of any sample will decrease as a function of the distance between the cleaved fiber end and the sample; and in many measurement scenarios, the reflections from the polished fiber ends are higher in magnitude than reflections from the sample.

In an 8-channel system, the maximum power returned from any one channel is $1/64$ of the input power (about 1.6%). The power returned from any one fiber end reflection is therefore approximately 6.25×10^{-2} % (4% of $1/64$) of the input power. Consequently, no choice of coupling ratio will be optimal for all possible reflectivities in the 8-channel system. However, a coupler that diverts 10% of input power to the retroreflector in the reference arm of the measurement interferometer can be expected to maximize the contrast of detected interference patterns over a broad range of sample reflectivities, and to provide better measurement precision than a 50% coupler for all possible sample reflectivites. To experimentally confirm this prediction, I used the system from Figure 4.2 to acquire two sets of measurements of the OPL between the cleaved fiber end of one channel and a BK7 glass flat located approximately 0.5 mm from the silicon v-groove array housing the fiber endface. In the first set of measurements, the coupling ratio between reference and sample arms was 0.5. In the second set, the coupling ratio was 0.1 (The coupler in question appears to the immediate right of the circulator in the measurement interferometer in Figure 4.2.)

In each set of measurements, the distance between the fiber endface and the BK7 flat was measured 4,000 times, once every 10 s over 11 hours. To minimize the influence of temperature variations, the 100-point moving standard deviation for each data set was averaged. (The time to acquire 100 measurements was about 17 min.) In the first set, the mean of the 100-point moving standard deviation of the data set was 15 x 10^{-3} of a DFT bin, and in the second, 3 x10^{-3} of a DFT bin. This threefold improvement in measurement precision confirms the importance of the selecting the proper coupling ratio between reference and sample arms in a power-limited SWI system, and also confirms that a 10/90 coupling ratio was an acceptable choice for the SWI system used for the experiments described here.

4.3 Calibration

In the time-multiplexed SWI system used for the experiments described in this chapter, the eight channels in the sample arm of the measurement interferometer are cleaved fiber ends, spaced equidistantly along a line, and housed in a silicon v-groove chip (Figure 4.3). I chose this sample arm arrangement because silicon v-groove fiber assemblies are readily available and have excellent manufacturing tolerances (±1 μm in fiber core positions). Other sample arm configurations, such as two-dimensional fiber arrays, lensed fiber ends, or fiber ends terminated by gradient-index (GRIN) lenses are certainly possible and could offer improvements over the 8-channel system presented here. No matter which sample arm configuration is chosen, however, measurement accuracy and resolution depend on both the accuracy and resolution of the SWI system itself and on the positional accuracy and resolution of the array of fiber ends in the sample arm of the measurement interferometer. In this section, I first present an analysis of the transverse resolution and accuracy of the 8-channel system of Figure 4.2. I then describe a calibration procedure to establish the axial accuracy for each of the eight channels and for the 8-channel system as a whole.

4.3.1 Transverse resolution

In the 8-channel SWI system use for the experiments described in this chapter, each channel is terminated at a cleaved fiber end, polished at a 0° angle. The beam emitted from single mode step-index fiber is very nearly Gaussian [150], so SMF-28 fiber, with a NA of 0.14, has a Rayleigh range of approximately 25 μm at 1550 nm. Because the minimum superresolvable reflector separation is 2 DFT bins—approximately 88 μm in air—for a laser sweep from 1525 nm to 1580 nm, the distance between any fiber endface and the sample surface must be at least 44 μm.

This is nearly twice the Rayleigh range of the beams emitted from each channel, and consequently, the transverse resolution of the SWI system cannon be obtained from the waist diameter of emitted Gaussian beams.

Instead, the area of the sample surface that returns light into any fiber channel can be determined using a ray optics approach. For a flat sample surface, transverse resolution is equal to the diameter of the fiber core[9], 9 μm in the case of SMF-28 fiber. This is illustrated in Figure 4.7. Although returned power decreases as the distance between the fiber endface and the sample surface increases, or as the angle between the surface and the fiber endface increases, the area of the sample surface that returns light to the fiber core remains constant.

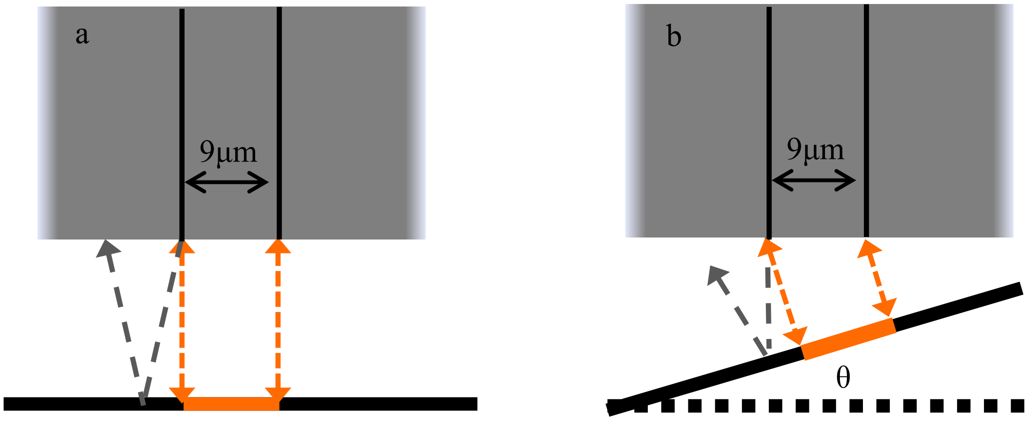

Figure 4.7 For a flat surface, transverse resolution is equal to fiber core size, regardless of (a) the distance between the fiber endface and the sample or (b) the angle between the fiber endface and the sample surface.

When the sample surface is curved, however, transverse resolution becomes a function of surface curvature, surface position, and the distance between the fiber endface and the sample

---

[9] Note that in this ray-optics based approach, it is the physical diameter of the fiber core, not the mode field diameter, that sets the transverse resolution of the system.

surface, as shown in Figure 4.8. For a convex surface, the sample surface area that reflects light back into the fiber core decreases relative to a flat sample surface, and transverse resolution consequently increases, while for a concave surface, transverse resolution decreases.

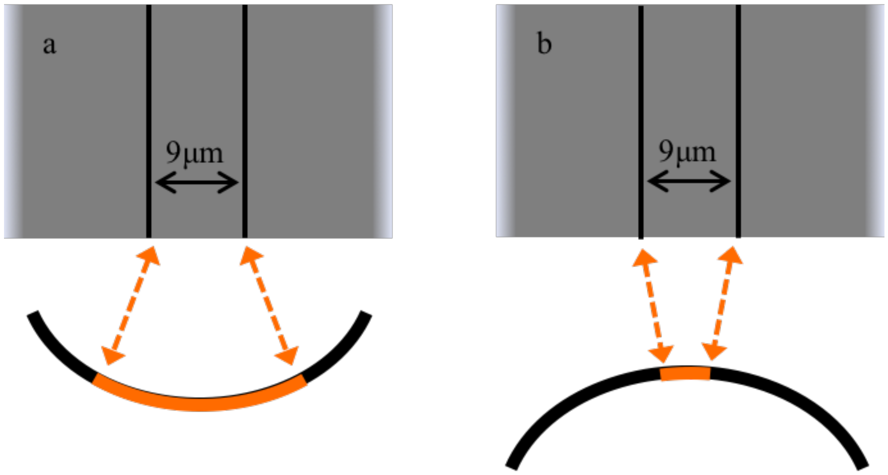

Figure 4.8 Transverse resolution depends on surface curvature and (a) decreases for concave surfaces or (b) increases for convex surfaces.

4.3.2 Transverse accuracy

In a time-multiplexed SWI system capable of completely static measurements of a sample surface (i.e. measurements which no mechanical scanning), transverse accuracy depends entirely on the accuracy with which the transverse locations of fiber cores are known. In the 8-channel system used for experiments here, the spacing of fiber cores in the silicon v-groove array is accurate to ±1 μm. The error this may introduce to surface measurements depends on the shape of the sample surface and cannot be determined for a general case. For a flat surface, transverse error in fiber core positions causes no error whatsoever in the surface measurement, but for a steeply-sloped surface, measurement error may be significant.

In the SWI system used for the experiments described in this chapter, the ends of the eight sample arm channels are spaced across a line in a silicon v-groove chip (Figure 4.3), and the SWI system relies on mechanical scanning of the sample in order to acquire measurements across a 3D sample surface. Consequently, the transverse accuracy of the system also depends on stage accuracy. The same x-y-z stage stack (Newport XMS160, XMS100, GTS30V) and steel scaffold structure that were used for experiments in Chapter 3 was also used here. The x-stage, used to translate the sample perpendicular to the line of fiber channel ends (Figure 3.16), has on-axis accuracy of 1.5 μm and bidirectional repeatability of 80 nm, giving a combined limit of $\pm$ 2.5 μm in the transverse position accuracy of each channel location.

4.3.3 Axial offset in channel positions

The axial offsets of each of the 8 fiber enfaces were determined by measuring the distances between each of the fiber endfaces and the surface of a 2-inch diameter, $\lambda/20$ (± 15.8 nm) aluminum mirror with a ZERODUR substrate. At each of six separate (presumably uncorrelated) locations on the mirror surface, 100 measurements of the delay time between fiber endfaces and the mirror surface were obtained. The offsets of each of the fiber cores are given by the residuals between the mean delay time measurements in each channel and the line fit to all mean measured delay times as a function of channel position y. This is shown in Figure 4.9. The maximum slope of all six line fits was less than 0.12°, meaning that the maximum axial calibration error from potential ± 1 μm transverse fiber core position errors is 27 as, or approximately 4 nm.

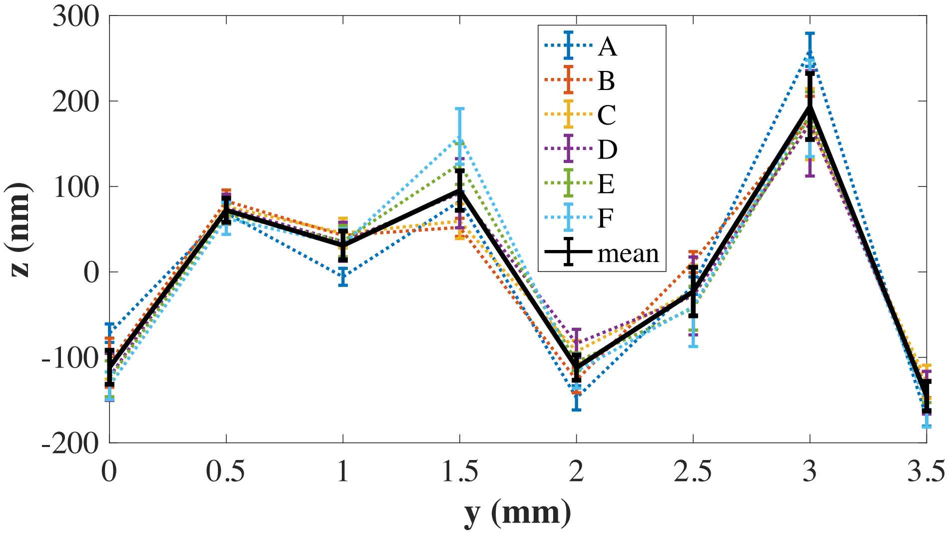

Figure 4.9 Axial calibration results for 8-channel SWI system. The results from six different mirror locations (A through F) are plotted along with the mean of all six measurements. Errorbars show measured 2σ standard deviation. An air index value of 1 was assumed in the conversion of measured delay time residuals to distance residuals (plotted here).

4.3.4 Axial accuracy the SWI system

The axial accuracy of the 8-channel SWI system is determined by the level of bias in superresolved SWI measurements. To quantify measurement bias for the system as a whole, I used a calibration procedure similar to the one described in Section 3.2. Once again, the reference standard was the surface of a 2-inch diameter, $\lambda/20$ $(\pm 15.8\,\text{nm})$ aluminum mirror with a ZERODUR substrate. This mirror was placed at an approximate 1° tilt angle on the polished ends of three 120 threads-per-inch adjustment screws, and mounted on the x-y-z stage stack beneath the silicon v-groove array. The reference mirror was translated in x across 3 mm in 30 µm increments. At each of the 101 x-locations, each of the 8 channels of the time-multiplexed SWI system measured a delay times between a fiber endface and the mirror surface. This measurement process was repeated 50 times.

Figure 4.10 shows mean values for the measured distances between fiber endfaces and the mirror surface as a function of mirror position *x* and channel location *y*. Physical distance *d* was obtained by multiplying the measured time delays by half the vacuum speed of light.

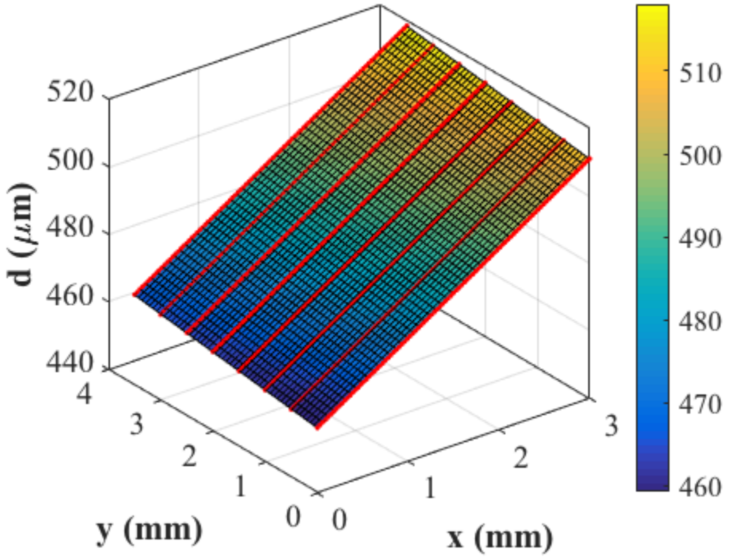

Figure 4.10 Measured distances d *(red dots) to the surface of a* $\lambda/20$ *mirror as a function of channel position* y *and stage position* x*. The planar surface fit is also shown.*

To evaluate the accuracy of 3D distance measurements, a first-order polynomial surface was fitted to the mean values of measured distances. The residuals between the surface fit and mean measured distances are plotted for each channel in Figure 4.11. Including the axial offsets (Figure 4.9) for each channel in the surface fit significantly reduces the range of the measured residuals.

The range of the residuals shown in Figure 4.11b is 224 nm, or $5.1\text{x}10^{-3}$ of a DFT bin, somewhat larger than the $1.8\text{x}10^{-3}$ residual range measured with the SWI system in Section 3.2, and substantially larger than the 2σ uncertainty value of 3 nm for two reflectors separated by approximately 20 DFT bins (Figure 2.17). The average standard deviation of all distance measurements was 117 nm, or $2.7\text{x}10^{-3}$ of a DFT bin, comparable to the mean standard deviation value of 135 nm for the measurements described in Section 3.2.

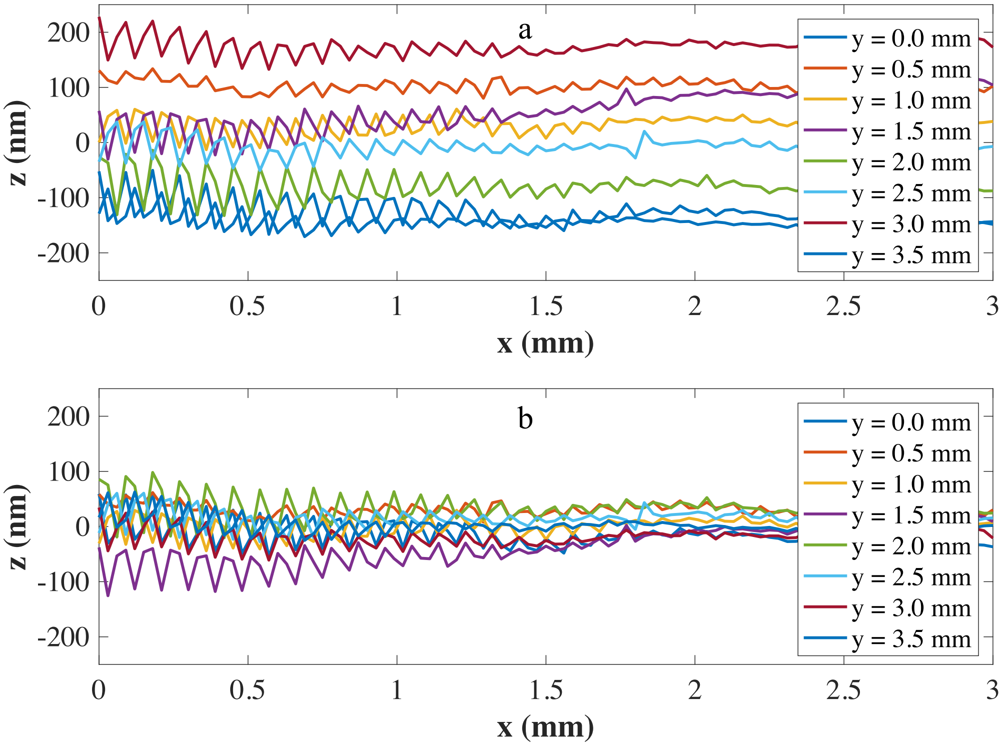

Figure 4.11 Surface fit residuals z *as a function of stage position* x *for each of the eight channels (a) without correction for axial positions of channels and (b) with correction for axial positions of channels.*

Some of the larger range of the measurement residuals shown in Figure 4.11 can be attributed to the obvious oscillation in the residuals observed between x = 0 mm and x = ~1.5 mm. This oscillation is likely the result of estimator bias, as its frequency matches the oscillation frequency of the bias in Candan estimates of the distance between two reflectors. This is shown in Figure 4.12.

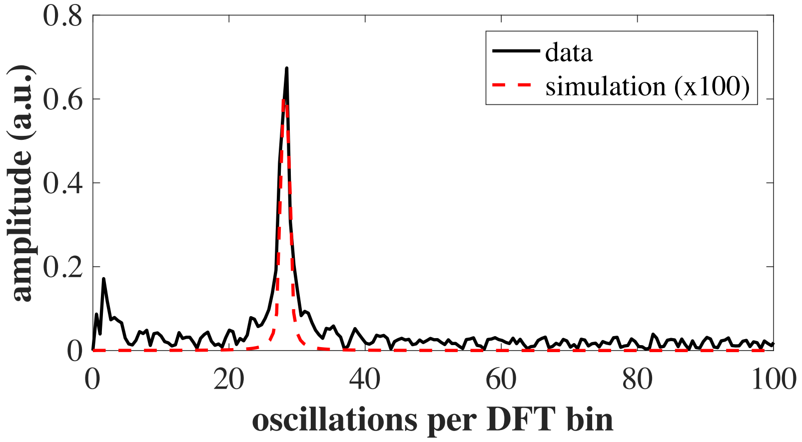

Figure 4.12 Magnitude of the discrete Fourier transform of a surface fit residual plotted along with the magnitude of the discrete Fourier transform of the bias in Candan estimates of distance between two simulated reflectors with a 3 dB difference in their relative amplitudes.

The difference in the measured peak heights[10] of fiber end reflections and mirror surface reflections is roughly 3 dB. (The relative heights of these two peaks are illustrated in Figure 4.13.) For peaks separated by about 20 DFT bins, and having a 3 dB difference in their relative amplitudes, the numerical model developed in Chapter 2 predicts a bias magnitude of just over 10^{-5} of a DFT bin (Figure 2.16). However, the magnitude of the oscillation observed in Figure 4.11 is approximately $3.5\text{x}10^{-3}$ of a DFT bin, roughly two orders of magnitude larger than the predicted value. The cause for this discrepancy is not immediately apparent. It may be due to the differences between the time-multiplexed SWI system and the numerical model, or to spectral leakage from additional mirror surface reflections due to an etalon effect (such an effect would be

---

[10] For peaks with the same shape function, relative peak heights are linearly proportional to relative peak areas, which can generally be measured with greater accuracy. Here, the relative heights of delay time peaks were calculated by multiplying the measured interferogram by a flattop window [159] [158], and, after taking the discrete Fourier transform of the windowed data, estimating peak areas using the trapezoidal method [157].

expected to diminish nonlinearly as a function of the distance between the silicon v-groove array and the mirror surface), or to some other, unknown, cause.

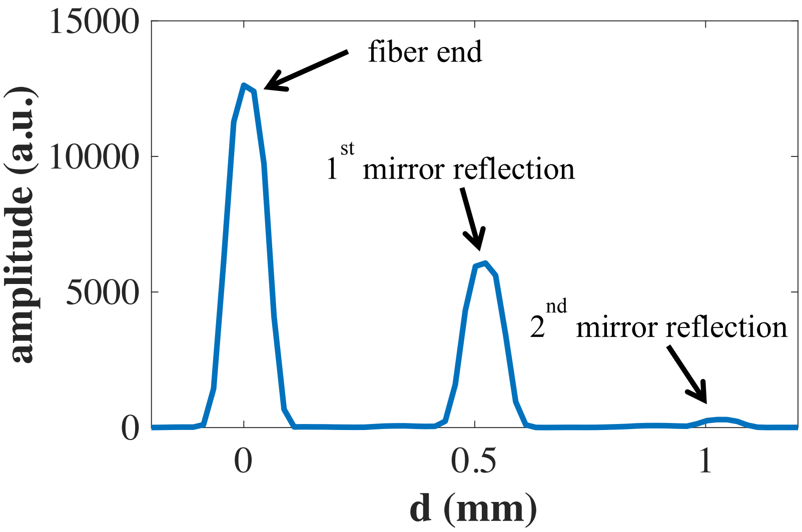

Figure 4.13 The measured height of the first reflection peak from the mirror surface is approximately half the height of the fiber endface reflection peak.

4.4 Surface Reconstruction

4.4.1 Reconstruction problem

Using diverging beams to measure distances between fiber endfaces and the sample surface creates a unique surface reconstruction problem. Although optical path length can be measured with great precision and accuracy, the angle at which any given optical path length is measured is unknown. This is illustrated in a two-dimensional example in Figure 4.14. Eight equally spaced channels in the sample arm of a time-multiplexed SWI system measure the distance between fiber endfaces and a circular sample surface. These measured distances are perpendicular to the sample surface. If these measured distances are assumed to have all been measured at the same angle (relative to the linear array of fiber endfaces), then the reconstructed surface may differ significantly from the true, measured surface.

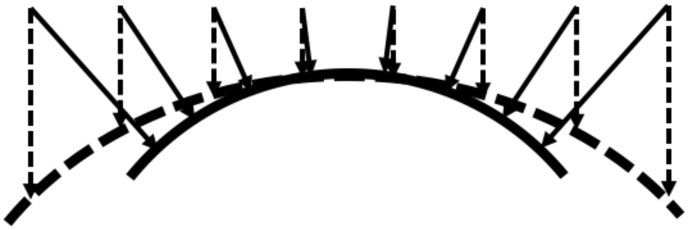

Figure 4.14 Eight equally spaced channels measure distances normal to a circular surface (solid line). Assuming that all measured distances are vertical causes error in the reconstructed surface (dashed line).

As the curvature or complexity of the measured surface increases, the potential magnitude of surface reconstruction error also increases, up to some limit imposed by the acceptance angle of the optical fiber. Although both the structure and magnitude of reconstruction errors depend uniquely on the measured sample surface, an example case can provide insight into the potential magnitude of surface reconstruction error. Here, I consider a circular surface measured with the 3-channel SWI system depicted in Figure 4.15. (I chose this case because there is an analytical solution for radius of curvature of a circle passing through three points[11] [151]; in the 8-channel example illustrated in Figure 4.14, the erroneously reconstructed surface would not be truly circular.) In this example, three equally spaced channels, each separated from the next by distance d, measure perpendicular distances a, b, and c to a circular surface with radius of curvature R.

---

[11] This problem is a special case of Apollonius' problem, first solved over 2,000 years ago!

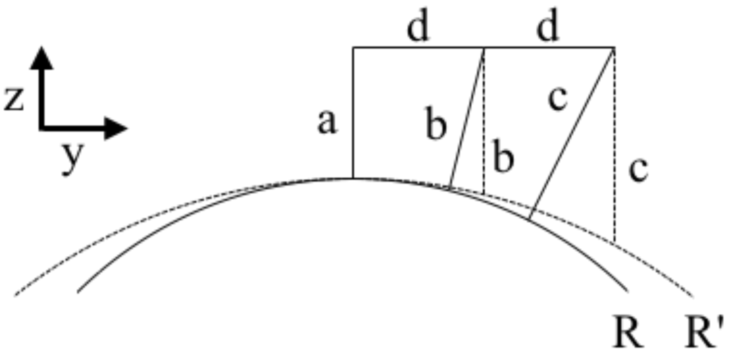

Figure 4.15 Assuming that measured distances are vertical causes error in the reconstruction of a circular surface with radius of curvature R. *The difference between the true radius of curvature* R *and the radius* R' *of the reconstructed surface is determined by the spacing* d *between channels, the distances a, b, and c between the channel ends and the surface, and the true radius of curvature* R.

Given some radius of curvature *R*, a channel spacing *d*, and a perpendicular measured distance *a*, measured distances *b* and *c* are given by

$$b = \sqrt{(R+a)^2 + d^2} - R \tag{4.4}$$

and

$$c = \sqrt{(R+a)^2 + 4d^2} - R\,. \tag{4.5}$$

respectively. Assuming that all measured distances are vertical, i.e. perpendicular to the linear channel array, the reconstructed circle must pass through points (0,-a), (d,-b), and (2d,-c). Choosing values for distances *a* and *d* and radius of curvature *R* to be similar to experimental values from Section 4.5.1 gives the following:

a = 500 µm,

d = 500 µm,

$$R = 25.8 \text{ mm}.$$

With these values, the radius of curvature R' of the reconstructed circle is approximately 26.6 mm. This represents an error of approximately 3% in the reconstructed radius of curvature, an error roughly four orders of magnitude larger than the limiting accuracy of the 8-channel SWI system used for the experiments of this chapter.

4.4.2 Reconstruction assumptions

In a fiber-based time-multiplexed SWI system, the minimum spacing between channels is fundamentally limited by the physical size of optical fiber. For SMF-28 fiber, minimum spacing is equal to the 125 μm cladding diameter, although fibers mounted in a silicon v-groove chip are spaced by at least twice this distance. Consequently, the spacing between channels will almost always be substantially larger than the transverse resolution of the SWI system, and the measured surface will be underconstrained. This is illustrated in Figure 4.16.

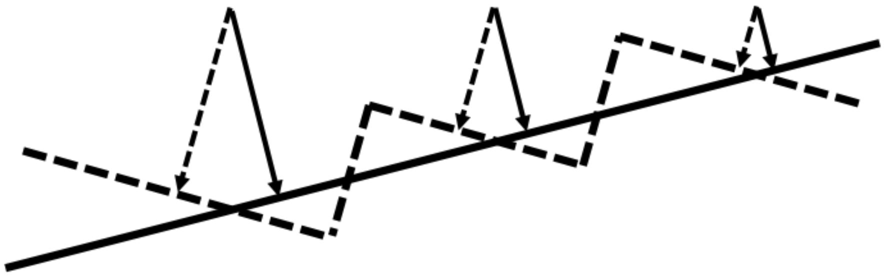

Figure 4.16 Identical sets of distance measurements can be obtained from two dramatically different sample surfaces.

Because the measured surface is underconstrained, the number of reconstructed surfaces is potentially infinite, and an *a priori* judgement must be made about the sample surface. The approach I take here is to assume that the sample surface matches, or very nearly matches, some analytic function. This approach is mathematically straightforward and likely a good fit for many optical surfaces. A different approach, which makes no assumptions about the surface shape and instead seeks to minimize the slope of the reconstructed surface, is explored in Section 5.2.2.

4.4.3 Reconstruction algorithm

After assuming some analytic function[12] $f(x,y)$ that describes the sample surface, the surface reconstruction problem can be stated as follows: what are the coefficients of that function that give a surface with surface normals that (a) pass through the locations c_i of the channel endfaces and (b) have lengths $d_i^{\perp}$ equal to the measured distances d_i^{meas} between each channel endface and the sample surface?

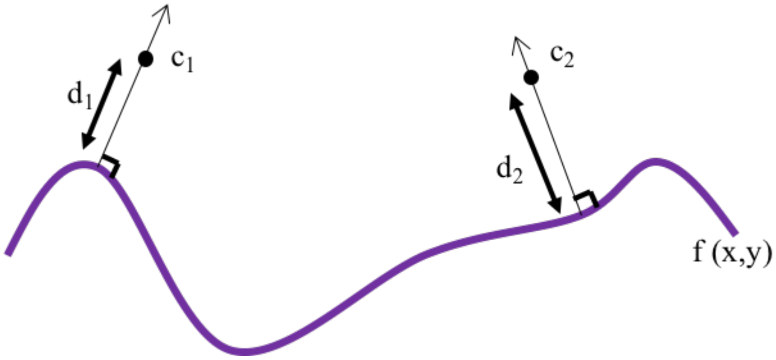

Figure 4.17 Surface function f(x,y) *with surface normals of distances* d_1 *and* d_2 *passing through two channel locations* c_1 *and* c_2.

---

[12] This function may simply be a description of the ideal sample surface, or it may also contain terms to describe surface aberrations.

With reasonable initial guesses for function coefficients, this problem may be solved iteratively using the algorithm outlined below. Figure 4.17 is provided for clarity.

1) Choose an analytic function *f (x,y,)* to describe the sample surface.
2) Make an initial guess for the coefficients of the surface function *f (x,y,)*.
3) Find all surface normals. (These are given by the negative reciprocal of the surface gradient.)
4) Select the surface normals that intersect points c_i, the locations of the *N* fiber endfaces corresponding to each channel.
5) Find lengths $d_i^{\perp}$ of these intersecting surface normals.
6) Compute a merit function by subtracting the lengths of intersecting surface normals from measured distances d_i^{meas} and sum the square of the differences, according to

$$Q = \sum_{i=1}^{N} \left(\begin{bmatrix} d_1^{\perp} \\ \vdots \\ d_N^{\perp} \end{bmatrix} - \begin{bmatrix} d_1^{mease} \\ \vdots \\ d_N^{meas} \end{bmatrix} \right)^2 . \tag{4.6}$$

7) Iterate through steps 3 through 6, optimizing function coefficients to minimize the merit function Q.

This algorithm was successfully used to determine the radius of curvature for a cylindrical lens in the measurement described in Section 4.5.1. However, the algorithm has one serious weakness. In addition to optimizing the coefficients of the sample surface function, it must also optimize six other parameters—the translations and rotations of the sample surface in Cartesian space. For many sample surfaces, one or more of these Euclidean transformations may be functions of the others, and as a result, the high-dimensional optimization search space is not convex and may be rapidly varying. Consequently, the required quality of initial guesses, both for function coefficients and for the position of the sample surface relative to channel endfaces, is unknown and may be extremely high.

4.5 Experimental Results

The time-multiplexed SWI system described in Section 4.2.1 was used to measure two samples, both with rotational symmetry of order two or lower. The first object, a cylindrical lens, was measured with a sampling density that could be easily achieved with a 2D channel array, and its surface was reconstructed using the algorithm described above. The second object, a Columbian 50-peso coin, was measured at a sampling density unachievable without either mechanical scanning of the object or significant alterations to the SWI system (such alterations are briefly discussed in Section 5.2.1). The coin surface is too complex to be reconstructed using an algorithm that relies on an analytic function to describe it, and in the measurement shown in Section 4.5.2, vertical beam paths were assumed. A reconstruction algorithm capable of dealing with complex sufaces of low symmetry is proposed in Section 5.2.2.

4.5.1 Cylindrical lens

A plano-convex cylindrical lens (Figure 4.18) with radius of curvature equal to 25.8 mm, ±3%, was metalized with a 10 nm layer of chrome, followed by a 40 nm layer of gold, to increase its reflectivity. It was then epoxied to a machined aluminum block and mounted approximately 0.6 mm below the silicon v-groove array on an x-y-z stage stack (Newport XMS160, XMS100, GTS30V). The long axis of the lens was mounted roughly parallel to the x-axis of the stage stack, and perpendicular to the line of channel endfaces in the v-groove array. A virtual 17 x 8 channel array was created by stepping the lens in seventeen 500 μm increments in *x*, acquiring a single time-multiplexed measurement at each step. To minimize the impact of thermal variation during the measurement process, this measurement procedure was repeated 50 times, and the delay time measurements of each channel at each *x*-location were averaged. To obtain distance measurements from delay time measurements, an air index value of 1 was assumed.

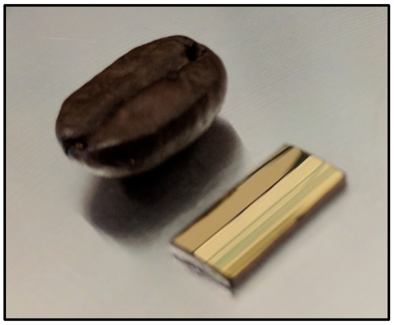

Figure 4.18 Plano-convex cylindrical lens, 5 mm x 10 mm, radius of curvature = 25.8 mm. Coffee bean is shown for scale.

To reconstruct the surface of the cylindrical lens, the algorithm from Section 4.4.3 was used, with the analytic surface function *f(x,y)* being the equation of a cylinder. MATLAB's *fmincon* function [152] (set to use the interior-point algorithm) was used to optimize the radius of curvature of the cylinder equation, along with the location and rotations of the cylinder in Cartesian space. For a convex surface, the length of any surface normal that intersects a point above the surface is also the shortest distance between the surface and the point. Therefore, instead of using an analytic function to determine surface normals in each iteration of the algorithm, a grid of points on the surface of the cylinder was generated, and the shortest distance between each channel point and the nearest surface grid point was taken to be the surface normal. The spacing between grid points was 9 µm, equal to the transverse resolution of the SWI system. Finally, the optimization process was seeded with the following initial guesses for the radius of curvature, location, and extrinsic rotations of the cylindrical surface:

$$R = 25.8 \text{ mm}$$

$$x = 0 \text{ mm}$$

$$y = 1.75 \text{ mm}$$

$$z = 25.8 \text{ mm}$$

$$\phi_x = 0°$$

$$\phi_x = 0°$$

$$\phi_x = 0°$$

The reconstructed cylindrical surface is shown in Figure 4.19. Its radius of curvature is 25.5 mm, well within the manufacturer's 3% error bounds for the specified 25.8 mm radius of curvature. Consistent with the expectations discussed in Section 4.4.1, the reconstructed surface lies within the surface that would be obtained by assuming that all measured distances are vertical (Figure 4.19b).

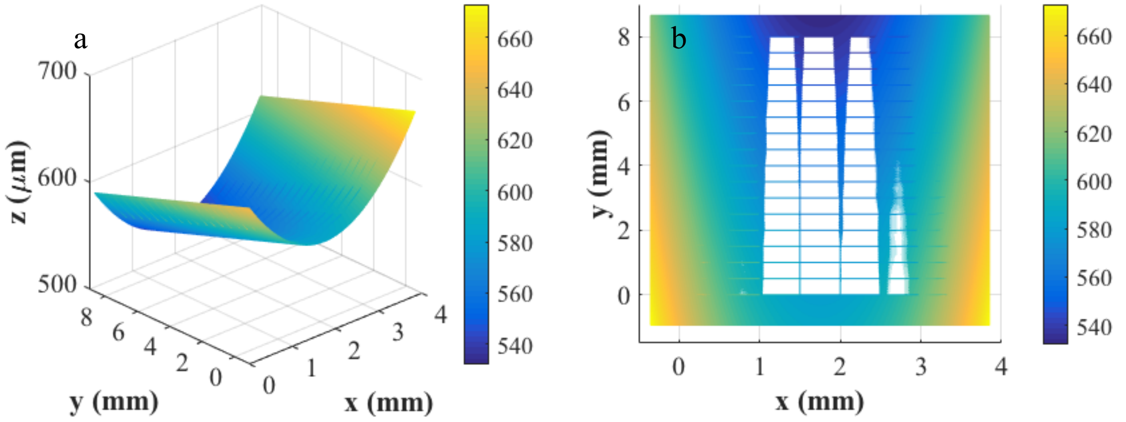

Figure 4.19 (a) Reconstructed cylindrical surface. (b) Top-down view of reconstructed surface plotted along with measured distances (coarse grid).

Figure 4.20 shows the absolute values of the differences between distances measured at each channel location and the lengths of the reconstructed surface normals that intersect those channel locations. These differences have a maximum value of 1.235 μm, roughly five times larger than the ±112 nm accuracy limit derived from the system calibration; and they show strong local variation, making them unlikely to be completely due to variation of the sample surface. However, all difference values are well below the transform-limited resolution of the SWI system (1.235 μm is approximately 2.84 x 10^{-2} of a single DFT bin), and it is difficult to distinguish between measurement errors and the potential shortcomings of the reconstruction algorithm.

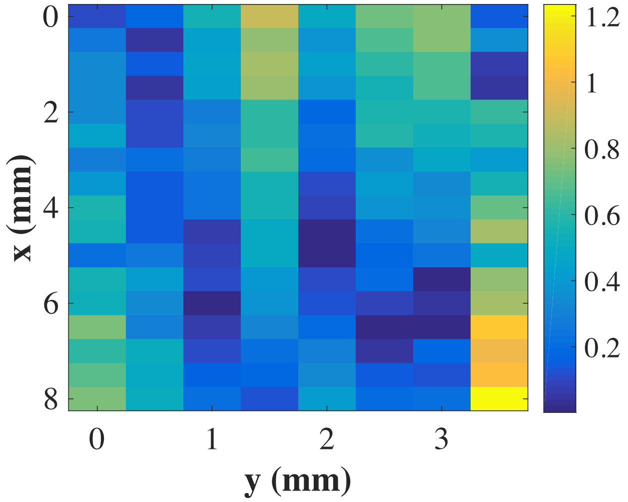

Figure 4.20 Absolute differences, in μm, between measured distances and the lengths of the surface normals that intersect channel locations.

4.5.2 Coin

To measure the 17 mm x 20 mm area surrounding the 50-peso coin (pictured in Figure 4.21a) with a sample spacing of 25 μm, 68,100 measurements were taken over the course of nearly 4 days. While this measurement time may seem excessive, it represents an 8-fold improvement over the time that would be required to measure the same coin at the same sampling density without time-multiplexing. The coin measurement required mechanical scanning in both x and y, and an algorithm for reconstructing its complicated surface does not exist. Nevertheless, the surface recovered by assuming that all measured beam paths are vertical still shows the capability of the time-multiplexed SWI system to make finely superresolved measurements (see Figure 4.22) and demonstrates the need for further algorithm development and improvements to sampling density restrictions.

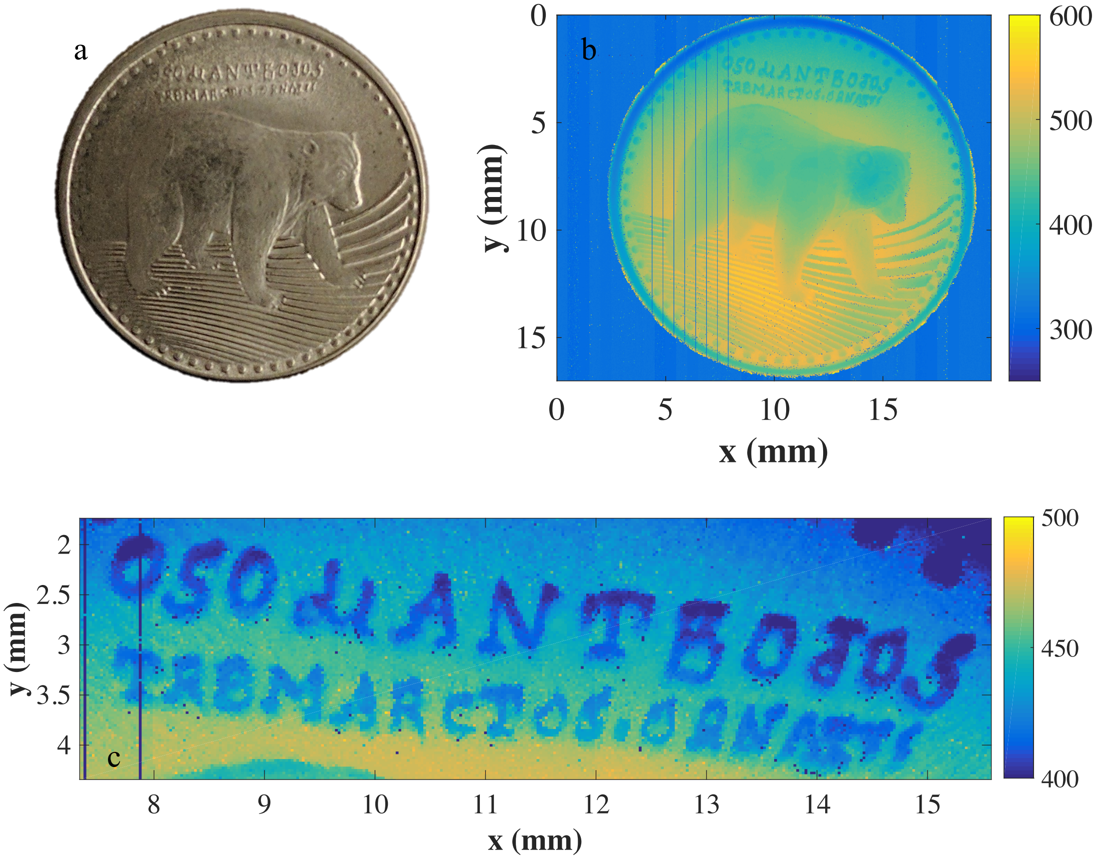

Figure 4.21 (a) Columbian 50-peso coin. (b) Image of measured distances between channel endfaces and the coin. (c) Detailed view of the Spanish and Latin names of the Spectacled Bear. Color bars in µm.

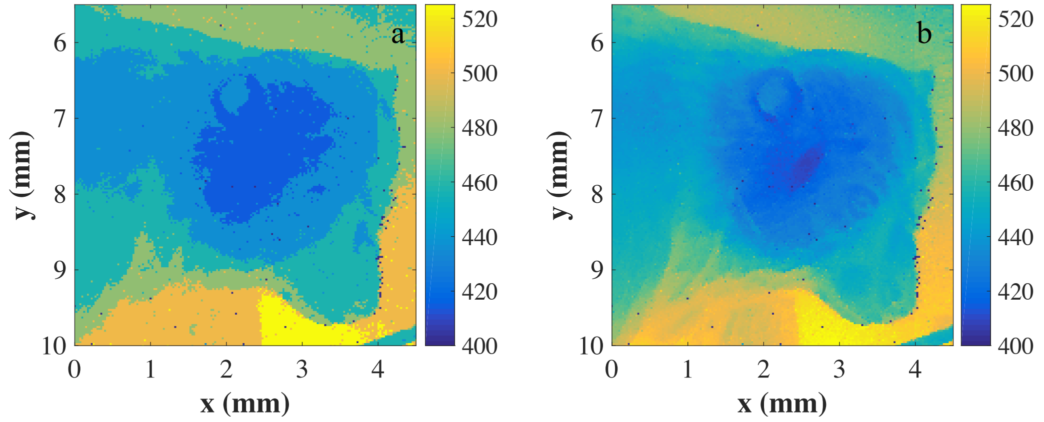

Figure 4.22 Comparison between (a) transform-limited and (b) superresolved images of the Spectacled Bear's cabeza. *Color bars in µm.*

4.6 Conclusions

At the outset of this chapter, I stated that time-multiplexed SWI has the potential to make non-scanning, 3D measurements of steeply sloped, unsymmetrical surfaces. The time-multiplexed SWI system described in this chapter cannot measure steeply-sloped surfaces (due to the linear arrangement of channel endfaces and the relatively small acceptance angle of SMF-28 fiber), and without mechanical scanning of the sample, it is restricted to 2D measurements (due to both the low number of channel endfaces and their linear arrangement). However, neither of these limitations are fundamental. Non-planar, 2D arrays of channel endfaces are can certainty be constructed, and with additional power from the tunable laser source, such arrays could contain many more than eight channels.

The work presented in this chapter is, to the best of my knowledge, the first experimental demonstration of a time-multiplexed SWI system. In applying it to the problem of surface measurement, I have achieved several worthwhile results. First, I have shown that the total time required to measure a 3D surface can be significantly reduced. Second, I demonstrated that the need for mechanical scanning of a 3D sample surface can be reduced, or even eliminated entirely. Third, I have clarified two important requirements for further development of time-multiplexed SWI for 3D surface metrology. These requirements—increased sampling density and surface reconstruction algorithms—will be discussed in the following chapter.

Chapter 5

Summary and Discussion of Future Work

5.1 Summary

This thesis began with a numerical investigation of the precision and uncertainty limits of superresolved swept-wavelength interferometry. Uncertainty in any superresolved SWI measurement is determined by two measures—the uncertainty in the size of a single DFT bin, and the bias present in any sub-transform-limited estimate of delay time. DFT bin size uncertainty is a function of, first, the consistency in the frequency spacing between samples of any measured interference pattern, and second, the accuracy with which that frequency spacing is known. For a SWI system that uses a trigger interferometer to maintain even frequency spacing between samples, DFT bin size uncertainty is dominated by uncertainty in the exact wavelengths of the absorption lines used to calibrated the trigger interferometer.

To evaluate bias in superresolved estimates of delay time, I used a numerical model to compare the accuracy of four frequency estimation methods in making such estimates. Two multiple-frequency estimation methods—Nonlinear Least Squares (NLS) and ESPRIT—and two single-frequency estimation methods—Local Linear Regression (LLR) and Candan's estimator—were applied to numerically generated SWI data and used to estimate delay times between two reflectors. For reflectors separated by roughly 20 DFT bins or less, only NLS estimates are unbiased. However, for more widely separated reflectors, Candan's estimator produces estimates with negligible bias at a fraction of the computation time required by NLS.

To evaluate the precision of NLS, ESPRIT, LLR and Candan's estimator, I used a numerical model to compare the variance of each of these estimators to the Cramér-Rao bound. With the exception of ESPRIT, all these estimators have variances closely approaching the Cramér-Rao bound. However, Candan estimates, computed using only three points from the delay time domain, show the greatest noise tolerance; this is a consequence of Parseval's relation for the DFT.

In an experimental SWI system, measurement accuracy may fail to reach limiting uncertainty values due to a number causes. In Chapter 3, I evaluated six of these potential causes: non-Gaussian noise, spurious delay times, power fluctuation across a laser sweep, dispersion mismatch between trigger and measurement interferometers, temperature drift in the trigger interferometer, and laser sweep rate nonlinearity. For SWI, the consequences of most forms of non-Gaussian noise cannot be predicted either analytically or numerically using existing models, and any systematic measurement error arising from non-Gaussian noise must be determined experimentally. By contrast, the effects of dispersion mismatch and temperature drift can by determined analytically, and the consequences of spurious delay times can be numerically predicted.

The exact effects of laser power fluctuation and laser sweep nonlinearity may be quantified, but they depend on the specific power and sweep-rate variations of any given tunable laser source. For the Agilent 81680A external cavity tunable laser used for all the experiments described in this thesis, I computed the effects of variations in both output power and sweep rate. Power fluctuations have the potential to degrade measurement accuracy to a much greater extent than does sweep rate variation; however, the effects of power variation may be controlled or eliminated by using balanced detection in the measurement interferometer.

Chapter 3 concluded with a description of a series of experimental SWI measurements of 101 distances, spaced equally through a range of 3 DFT bins. This measurement series had a maximum bias of 62 nm, or 1.8×10^{-3} of the SWI system's transform-limited resolution, roughly one order of magnitude larger than the measurement's limiting uncertainty of 4 nm, and an average 1σ standard deviation of 135 nm. The discrepancy between the measured 135 nm standard deviation and the ~1 nm theoretical limit is attributable to temperature variation during the experiment.

The concept of time-multiplexed SWI was first suggested by Dr. Eric Moore (in the concluding chapter of his own Ph.D. thesis) as a possible method for increasing the speed of SWI measurements [51]. In my thesis work, I have built on this idea, experimentally demonstrating the feasibility of time-multiplexed SWI, and exploring its potential to make 3D measurements of low-symmetry surfaces.

In a time-multiplexed SWI system, the unambiguous range of the SWI system is divided among many channels, allowing simultaneous, parallel measurements of delay time to be obtained from each channel. Experimentally, this is accomplished by splitting the sample arm of the measurement interferometer into multiple physical channels. By constructing each channel from different lengths of optical fiber, the channels are assigned different portions of the unambiguous range of the SWI system.

One of the chief concerns in the design of such a system, particularly if delay time measurements are to be superresolved, is maintaining adequate SNR. Because the maximum power returned from each channel is inversely proportional to the total number of channels, SNR may deteriorate rapidly as the number of measurement channels in the system is increased. In a system dominated by quantization noise, signal contrast, and thus SNR, can be maximized with an appropriate choice of the power coupling ratio between reference and sample arms of the measurement interferometer.

To obtain high-accuracy 3D profiles of sample surfaces with a time-multiplexed SWI system, two key requirements must be met. First, the physical locations of all channel termini must be known, relative to each other, to at least the level of accuracy desired from the sample surface profile. Second, a method for reconstructing the sample surface profile from measured distances must be available. In Section 4.3, I described a calibration method for the 8-channel time-multiplexed SWI system that I developed and used for the experiments detailed in Chapter 4. In this system, each of the 8 channels is terminated at a cleaved, polished fiber end face and housed in a silicon v-groove array. Consequently, these channels are separated from each other by much more than the transverse resolution of the system, and unless the sample is mechanically scanned, the sample surface reconstruction will be under-constrained.

In Chapter 4, two surface measurement experiments were described. In the first experiment, I used the 8-channel SWI system to produce a synthetic array of distance measurements (comparable to the sort of measurements that could be obtained from a two-dimensional channel array) to the surface of a cylindrical lens. I then developed an algorithm for reconstructing the surface profile of the cylindrical lens from the array of distance measurements. Because the surface of the cylindrical lens can be described by an analytic function, and because it varies smoothly and slowly on the scale defined by the spacing between channels, the surface reconstruction algorithm was able to determine the radius of curvature of the lens to within the lens manufacturer's margin of error.

In a second experiment, I measured the surface of a Columbian 50-peso coin. This surface is not slowly varying, nor can it be readily described by an analytic function. Consequently, the coin required significant mechanical scanning to achieve reasonable sampling density across its surface. Additionally, the reconstructed surface has lower fidelity than that of the coin, since all measured distances were assumed to be perpendicular to the array of channel endfaces. However, the coin surface measurement clearly illustrates the capability of time-multiplexed SWI to make finely-superresolved surface measurements with greatly reduced measurement times. In the remaining section of this chapter, I outline two potential approaches to the outstanding problems of sampling density and surface reconstruction.

5.2 Future Work

5.2.1 Multistatic SWI

One intriguing possibility for increasing sampling density in a fiber-based, time-multiplexed SWI system is to create a multistatic SWI by allowing crosstalk between channels. This could be accomplished by increasing the distance between the channel endface array and the sample surface, or by using higher NA fiber in the channels, or both. Similar ideas have been proposed in the past [51], and an FMCW ladar system using trilateration along with mechanical scanning has been used to measure surface profiles for diffusely scattering surfaces [153].

One of the primary design concerns in a multistatic system is the proper selection of channel lengths. A simple example can be used to illustrate the complexity of this problem, and to point to a potential method for solving it. In Figure 5.1, a simplified diagram of the sample arm of a 3-channel multistatic SWI system is shown. In addition to the 3 individual path length measurements made by each of the 3 channels, 3 more distance measurements can be obtained in a multistatic configuration.

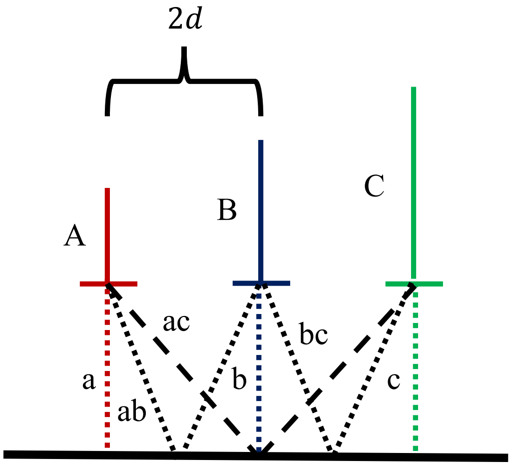

Figure 5.1 Sample arm in a multistatic SWI with three channels. Capital letters denote the channel length, and lower case letters denote the path lengths between channels.

For channels of lengths A, B, and C, spaced along a line at intervals of distance $2d$, and with separations of lengths a, b, and c between the end of each channel endface and the sample surface, Table 5.1 gives the delay times measured by each channel.

Table 5.1 Delay times measured by each channel as a function of channel length (capital letters) and the distances between channel termini and the sample surface (lowercase letters).

Channel 1	**Channel 2**	**Channel 3**
$2A + 2a$	$2B + 2b$	$2C + 2c$
$A + B + 2ab$	$A + B + 2ab$	$B + C + 2bc$
$A + C + 2ac$	$B + C + 2bc$	$A + C + 2ac$

The detected signal is a superposition of the signals in all 3 channels, and its Fourier transform contains peaks at each of the six unique delay times measured by the 3-channel, multistatic system. Figure 5.2 shows the proportional spacing between delay times for the following channel lengths and spacings:

$$A = 2d$$

$$a = b = c = 2d$$

$$B = 2A$$

$$C = 3A$$

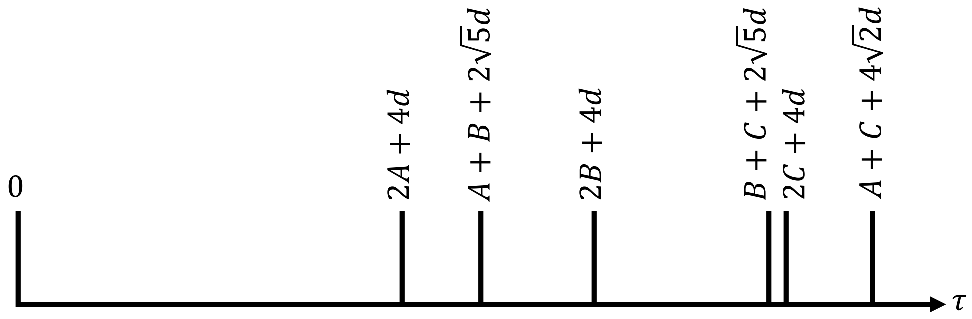

Figure 5.2 Composite signal measured in the 3-channel multistatic SWI.

In any multichannel system, the maximum delay time must be below some value set by either the coherence length of the laser sources, or what is more likely, by the maximum allowable uncertainty in superresolved measurements of delay time (Figure 2.17). Additionally, the minimum spacing between any two delay times must be no less than the Rayleigh resolution of the SWI system. Even in a 3-channel system, adjusting the channel lengths and spacings to meet both these requirements is challenging, and in a multistatic system containing many more than 3 channels, the complexity of the channel length problem is significant.

The problem could be approached numerically, by optimizing channel lengths, or both channel lengths and distances of each channel from the sample surface, or even channel lengths, surface distances, and lateral channel spacings (although optimizing the later requires building a custom channel array). These constants should be optimized so that the minimum distance between any two delay times is at least equal to the Rayleigh resolution of the system, and the maximum delay time satisfies the maximum uncertainty constraint. In the 3-channel example, each of the delay time differences $\Delta\tau_{ij}$ given by

$$\begin{matrix} \tau_1 & \tau_2 & \tau_3 & \tau_4 & \tau_5 & \tau_6 \\ \tau_1 & \tau_2 & \tau_3 & \tau_4 & \tau_5 & \tau_6 \\ \tau_1 & \tau_2 & \tau_3 & \tau_4 & \tau_5 & \tau_6 \\ \tau_1 & \tau_2 & \tau_3 & \tau_4 & \tau_5 & \tau_6 \\ \tau_1 & \tau_2 & \tau_3 & \tau_4 & \tau_5 & \tau_6 \\ \tau_1 & \tau_2 & \tau_3 & \tau_4 & \tau_5 & \tau_6 \end{matrix} - \begin{matrix} \tau_1 & \tau_1 & \tau_1 & \tau_1 & \tau_1 & \tau_1 \\ \tau_2 & \tau_2 & \tau_2 & \tau_2 & \tau_2 & \tau_2 \\ \tau_3 & \tau_3 & \tau_3 & \tau_3 & \tau_3 & \tau_3 \\ \tau_4 & \tau_4 & \tau_4 & \tau_4 & \tau_4 & \tau_4 \\ \tau_5 & \tau_5 & \tau_5 & \tau_5 & \tau_5 & \tau_5 \\ \tau_6 & \tau_6 & \tau_6 & \tau_6 & \tau_6 & \tau_6 \end{matrix}$$

$$= \begin{matrix} \Delta\tau_{11} & \Delta\tau_{21} & \Delta\tau_{31} & \Delta\tau_{41} & \Delta\tau_{51} & \Delta\tau_{61} \\ \Delta\tau_{12} & \Delta\tau_{22} & \Delta\tau_{32} & \Delta\tau_{42} & \Delta\tau_{52} & \Delta\tau_{62} \\ \Delta\tau_{13} & \Delta\tau_{23} & \Delta\tau_{33} & \Delta\tau_{43} & \Delta\tau_{53} & \Delta\tau_{63} \\ \Delta\tau_{14} & \Delta\tau_{24} & \Delta\tau_{34} & \Delta\tau_{44} & \Delta\tau_{54} & \Delta\tau_{64} \\ \Delta\tau_{15} & \Delta\tau_{25} & \Delta\tau_{35} & \Delta\tau_{45} & \Delta\tau_{55} & \Delta\tau_{65} \\ \Delta\tau_{16} & \Delta\tau_{26} & \Delta\tau_{36} & \Delta\tau_{46} & \Delta\tau_{56} & \Delta\tau_{66} \end{matrix} \tag{5.1}$$

must be maximized, or must at least be equal to the system's Rayleigh resolution. Similarly, the maximum value of any individual delay time τ_i should be minimized, or should at least be less than some acceptable ceiling value. Even in the 3-channel case, this problem appears daunting. In a mutistatic SWI system containing many channels (10 or more), the solution to the channel length problem would require much more attention and ingenuity.

One possible solution to the channel length problem is a change in the geometry of the interferometer, from the Michelson, or reflection geometry shown in Figure 5.1, to the Mach-

Zehnder, or transmission geometry, depicted in Figure 5.3. In Figure 5.3, the two transmission channels (dashed lines) emit a signal collected by the three receiver channels (solid lines). This geometry does causes a reduction in sampling density—because some of the fibers in the channel array are used only as emitters—but it significantly reduces the complexity of the channel length problem.

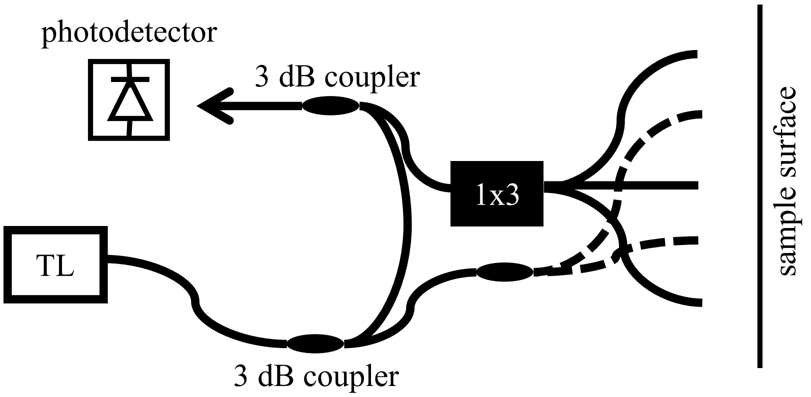

Figure 5.3 System diagram for a multistatic SWI system with Mach-Zehnder geometry. Light emitted by two transmission channels (dashed lines) is collected by the three receiver channels (solid lines). TL = tunable laser.

Figure 5.4 shows a simplified, 2D version of the sample arm of a Mach-Zehnder, multistatic SWI system. In this system, three receiver channels are alternately spaced with two transmitter channels. Each channel is separated from its nearest neighbors by distance 2d, and the channel endface array is separated from the flat sample surface by a distance c. Each of the three receiver channels collects a signal containing two delay times, one originating from each of the transmitter channels.

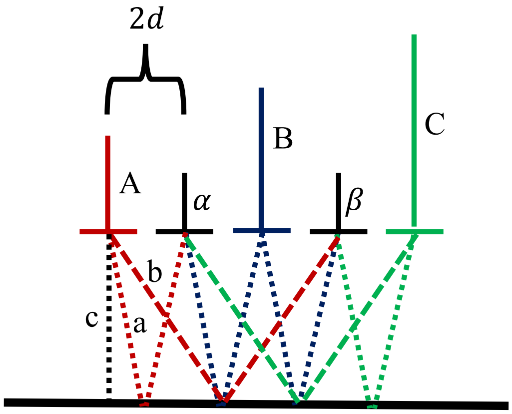

Figure 5.4 Sample arm in a multistatic Mach-Zehnder SWI system with two transmission channels of lengths α and β, and three receiver channels of lengths A, B, and C.

Table 5.2 lists the delay times measured by each of the three receiver channels, assuming the path lengths α and β of the transmitter channels are equal. Unlike the Michelson-geometry multistatic SWI, in which measured delay times are interdependent functions of channel path lengths, the Mach-Zehnder-geometry SWI produces measured delay times that are independent functions of a single channel path length. In the example of Figure 5.4, the two delay times measured by any one receiver channel are separated by a delay time proportional to the distance 2d between channels in the array. And the delay time differences between channels are functions only of the path lengths A, B, and C of the receiver channels. This result allows the channel path lengths to be optimized with relative ease. Consequently, although the Mach-Zehnder geometry comes at the cost of reduced sampling density, it may offer the best path forward for the development of a multistatic SWI system.

Table 5.2 Delay times measured by each channel as a function of channel length and the distances between channel termini and the sample surface.

Channel 1	**Channel 2**	**Channel 3**
$A+\alpha+2\sqrt{d^2+c^2}$	$B+\alpha+2\sqrt{d^2+c^2}$	$C+\alpha+2\sqrt{d^2+c^2}$
$A+\ \alpha+2\sqrt{9d^2+c^2}$	$B+\alpha+2\sqrt{9d^2+c^2}$	$C+\alpha+2\sqrt{9d^2+c^2}$

5.2.2 Surface reconstruction using Hermite splines

For sample surfaces with little or no symmetry, the surface reconstruction algorithm described in Section 4.4.3 cannot be used, as it relies on an analytic function to described the sample surface. Furthermore, it is an optimization algorithm with a search space that is very unlikely to be convex. Because search space changes depending on the analytic function used to describe the sample surface, the tolerances on the "initial guess" that are required for the optimization process to converge to the global maximum are unknown.

Here, I present one potential alternative to the method described in Section 4.4.3. Instead of assuming the sample surface can be described by an analytic function, this method assumes only that the sample surface is the most slowly varying surface that is able to meet the following two constraints:

1) For any distance measurement from any channel, the sample surface must intersect the spherical shell representing all possible directions for that distance measurement.
2) At points of intersection between the sample surface and the spherical shell of distances, the sample surface must be perpendicular to the line between the intersection point and the channel endface location.

These constraints are illustrated for a 2D surface in Figure 5.5.

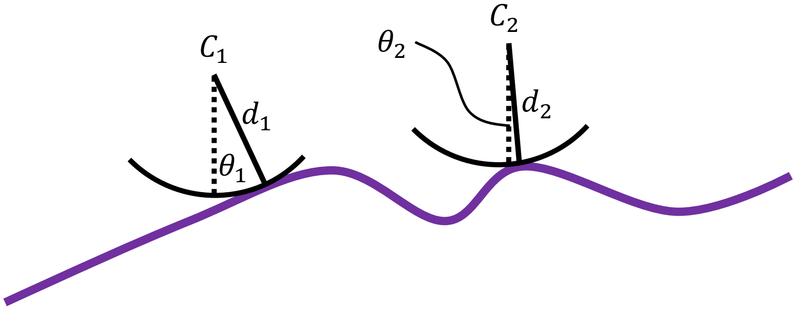

Figure 5.5 For an arbitrary sample surface, the distances d_1 *and* d_2 *measured from channel enface locations* C_1 *and* C_2 *must intersect the sample surface and be perpendicular to the sample surface at the points of intersection.*

An arbitrary sample surface can be described with Hermite splines, which, most conveniently, are defined both by the points they intersect and by the slope of the spline at the points of intersection [154]. The angles corresponding to each measured distance (angles θ_i in the 2D example shown in Figure 5.5) may then be optimized to minimize the maximum derivative of the surface shape, or equivalently, to find the minimum-order Hermite spline necessary to satisfy both of the constraints outlined above.

Bibliography

[1] F. Cardarelli, Encyclopaidia of Scientific Units, Weights and Measures: Their SI Equivalents and Origins, Springer, 2003.

[2] J. Fischer and J. Ullrich, "The new system of units," *Nature Physics,* vol. 12, no. 1, pp. 4-7, 2016.

[3] E. G. Bowen, Radar Days, CRC Press, 1998.

[4] T. H. Maiman, "Stimulated Optical Radiation in Ruby," *Nature,* vol. 187, no. 4736, pp. 493-494, 1960.

[5] A. Orszag, "Moon distance measurement by laser," *Journal of Research of the National Bureau of Standards. Section D: Radio Science,* vol. 69D, no. 12, pp. 1681-1689, 1965.

[6] L. D. Smullin and G. Fiocco, "Optical echos from the moon," *Nature,* vol. 194, no. 4835, p. 1267, 1962.

[7] E. Trickey, P. Church and X. Cao, "Characterization of the OPAL obscurant penetrating LiDAR in various degraded visual environments," *Proceedings of SPIE,* vol. 8737, no. 613, p. 87370E, 2013.

[8] M. C. Amann, T. Bosch, M. Lescure, R. Myllyla and M. Rioux, "Laser ranging: a critical review of useful techniques for distance measurement," *Optical Engineering,* vol. 40, no. 1, pp. 10-19, 2001.

[9] A. G. Stove, "Linear FMCW radar techniques," in *IEE Proceedings F (Radar and Signal Processing)*, 1992.

[10] M. A. Richards, Fundamentals of Radar Signal Processing, New York: McGraw-Hill, 1005.

[11] W. Eickhoff and R. Ulrich, "Optical frequency domain reflectometry in single-mode fiber," *Applied Physics Letters,* vol. 39, no. 9, pp. 693-695, 1981.

[12] M. K. Barnoski and S. M. Jensen, "Fiber waveguides: a novel technique for investigating attenuation characteristics," *Applied Optics,* vol. 15, no. 9, pp. 2112-2115, 1976.

[13] B. J. Soller, D. K. Gifford, M. S. Wolfe and M. E. Froggatt, "High-resolution optical frequency domain reflectometry for characterization of components," *Optics Express,* vol. 13, pp. 666-674, 2005.

[14] J. P. von der Weid, R. Passy, G. Mussi and N. Gisin, "On the characterization of optical fiber network components with optical frequency domain reflectometry," *Journal of Lightwave Technology,* vol. 15, no. 7, pp. 1131-1141, 1997.

[15] M. Froggatt and J. Moore, "High-spatial-resolution distributed strain measurement in optical fiber with Rayleigh scatter," *Applied Optics,* vol. 37, no. 10, pp. 1735-1740, 1998.

[16] D. K. Gifford, M. E. Froggatt and S. T. Kreger, "High precision, high sensitivity destributed displacement and temperature measurements using OFDR-based phase tracking," in *Proceedings of SPIE 7753, 21st Internation Conference on Optical Fiber Sensors, 775331*, 2011.

[17] S. T. Kreger, D. K. Gifford, M. E. Froggatt, B. J. Soller and M. S. Wolfe, "High Resolution Distributed Strain or Temperature Measurements in Single- and Multi- Mode Fiber Using Swept-Wavelength Interferometry," in *Optical Fiber Sensors OSA Technical Digest (CD)*, 2006.

[18] D.-P. Zhou, Z. Qin, W. Li, L. Chen and X. Bao, "Distributed vibration sensing with time-resolved optical frequency-domain reflectometry," *Optics Express,* vol. 20, no. 12, pp. 13138-13145, 2012.

[19] Z. Ding, X. S. Yao, T. Liu, Y. Du, K. Liu, Q. Han, Z. Meng and H. Chen, "Long-range vibration sensor based on correlation analysis of optical frequency-domain reflectometry signals," *Optics Express,* vol. 20, no. 27, pp. 28319-28329, 2012.

[20] E. Baumann, F. R. Giogetta, I. Coddington, L. C. Sinclair, K. Knabe, W. C. Swann and N. R. Newbury, "Comb-calibrated frequency-modulated continuous-wave ladar for absolute distance measurements," *Optics Letters,* vol. 38, no. 12, pp. 2026-2028, 2013.

[21] E. Baumann, F. R. Giorgetta, J. D. Deschenes, W. C. Swann, I. Coddington and N. R. Newbury, "Comb-calibrated laser ranging for three-dimensional surface profiling with micrometer-level precision at a distance," *Optics Express,* vol. 22, no. 21, pp. 24914-24928, 2014.

[22] A. B. Mateo and Z. B. Barber, "Precision and accuracy testing of FMCW ladar-based length metrology," *Applied Optics,* vol. 54, no. 19, pp. 6019-6024, 2015.

[23] Z. W. Barber, J. R. Dahl, T. L. Sharpe and B. I. Erkmen, "Shot noise statistics and information theory of sensitivity limits in frequency-modluated continuous wave ladar," *Journal of the Optical Society of America,* vol. 30, no. 7, pp. 135-1341, 2013.

[24] L. E. Smith, M. Bonesi, R. Smallwood and S. J. Matcher, "Using swept-source optical coherence tomography to monitor the formation of neo-epidermis in tissue-engneered skin," *Journal of tissue engineering and regenerative medicine,* vol. 4, no. 8, pp. 652-658, 2010.

[25] O. Babalola, A. Mamalis, H. Lev-Tov and J. Jagdeo, "Optical coherence tomography (OCT) of collagen in normal skin and skin fibrosis," *Archnives of dermatological research,* vol. 306, no. 1, pp. 1-9, 2014.

[26] I. V. Larina, N. Sudheendran, M. Ghosn, J. Jiang, A. Cable, K. V. Larin and M. E. Dickinson, "Live imaging of blood flow in mammalian embryos using Doppler swept-source optical coherence tomography," vol. 13, no. 6, p. 060506, 2008.

[27] M. Bonesi, S. Matcher and I. Meglinski, "Doppler optical coherence tomography in cardiovascular applications," *Laser Physics,* vol. 20, no. 6, pp. 1491-1499, 2010.

[28] B. Lee, W. Choi, J. J. Liu, C. D. Lu, J. S. Schuman, G. Wollstein, J. S. Duker, N. K. Waheed and J. G. Fugimoto, "Cardiac-Gated En Face Doppler Measurement of Retinal Blood Flow Using Swept-Source Optical Coherence Tomography at 100,000 Axial Scans per Second," *Investigative opthaology & visual science,* vol. 56, no. 4, pp. 2522-2530, 2015.

[29] H. Itakura, S. Kishi, D. Li, K. Nitta and H. Akiyama, "Vitreous Changes in High Myopia Observed by Swept-Source Optical Coherence Tomography," *Investigative opthamology & visual science,* vol. 55, no. 3, pp. 1447-1452, 2014.

[30] I. Grulkowski, J. J. Liu, B. Potsaid, V. Jayaraman, C. D. Lu, J. Jiang, A. E. Cable, J. S. Duker and J. G. Fujimoto, "Retinal, anterior segment and full eye imaging using ultrahigh speed swept source OCT with vertical-cavity surface emitting lasers," *Biomedical Optics Express,* vol. 3, no. 11, pp. 2733-2751, 2012.

[31] V. Jhanji, B. Yang, M. Yu, C. Ye and C. K. Leung, "Corneal thickness and elevation measurements using swept-source optical coherence tomography in normal and keratoconic eyes," *Clinical & experimental ophthalmology,* vol. 41, no. 8, pp. 735-745, 2013.

[32] G. Mussi, N. Gisin, R. Passy and J. P. von der Weid, "-152.5 dB sensitivity high dynamic-range optical freqency-domain reflectometry," *Electronics Letters,* vol. 32, no. 10, pp. 926-927, 1996.

[33] E. D. Moore and R. R. McLeod, "Phase-sensitive swept-source interferometry for absolute ranging with application to measurements of group refractive index and thickness," *Optics Express,* vol. 19, no. 9, pp. 8117-8126, 2011.

[34] V. A. dos Santos, L. Schmetterer, M. Groschl, G. Garhofer, D. Schmidl, M. Kucera, A. Unterhuber, J. Hermand and R. Werkmeister, "In vivo tear film thickness measurement and

tear film dynamics visulization using spectral domain optical coherence tomography," *Optics Express,* vol. 23, no. 16, pp. 21043-21063, 2015.

[35] M. G. Gustafsson, "Surpassing the lateral resolution limit by a factor of two using structured illumination microscopy," *Journal of Microscopy,* vol. 198, no. 2, pp. 82-87, 2000.

[36] S. T. Hess, T. P. Girirajan and M. D. Mason, "Ultra-high resolution imaging by fluorescence photoactivation localization microscopy," *Biophysical Journal,* vol. 91, no. 11, pp. 4258-4272, 2006.

[37] M. J. Rust, M. Bates and X. Zhuang, "Sub-diffraction-limit imaging by stochastic optical reconstruction microscopy (STORM)," *Nature Methods,* vol. 3, no. 10, pp. 793-796, 2006.

[38] S. W. Hell and J. Wichmann, "Breaking the diffraction resolution limit by stimulated emission: stimulated-emission-depletion fluorescence microscopy," *Optics Letters,* vol. 19, no. 11, pp. 780-782, 1994.

[39] J. L. Harris, "Diffraction and resolving power," *JOSA,* vol. 54, no. 7, pp. 931-936, 1964.

[40] C. W. Barnes, "Object restoration in a diffraction-limited imaging system," *JOSA,* vol. 56, no. 5, pp. 575-578, 1966.

[41] R. W. Gerchberg, "Super-resolution through error energy reduction," *Journal of Modern Optics,* vol. 21, no. 9, pp. 709-720, 1974.

[42] M. Betero and P. Boccacci, "Super-resolution in computational imaging," *Micron,* vol. 34, no. 6, pp. 265-273, 2003.

[43] J. W. Goodman, Fourier Optics, 3rd ed. ed., Englewood, CO: Roberts & Company, 2005.

[44] E. J. Candes and C. Fernandez-Granda, "Towards a Mathematical Theory of Super-Resolution," *Communications on Pure and Applied Mathematics,* vol. 67, no. 6, pp. 906-956, 2014.

[45] D. C. Rife and R. R. Boorstyn, "Single tone parameter estimation from discrete-time observations," *IEEE Transactions on Information Theory,* vol. 20, no. 5, pp. 591-598, 1974.

[46] P. Stoica and R. L. Moses, Spectral Analysis of Signals, Upper Saddle River, NJ: Pearson Prentice Hall, 2005.

[47] S. Tretter, "Estimating teh Frequency of a Noisy Sinusoid by Linear Regression," *IEEE Transactions on Information Theory,* vol. 31, pp. 832-835, 1985.

[48] R. G. McKilliam, B. G. Quinn, I. V. Clarkson and B. Moran, "Frequency estimation by phase unwrapping," *IEEE Transactions on Signal Processing,* vol. 58, no. 6, pp. 2953-2963, 2010.

[49] G. Lank, I. Reed and G. Pollon, "A semicoherent detection and doppler estimation statistic," *IEEE Transactions on Aerospace and Electronic Systems,* Vols. AES-9, pp. 151-165, 1973.

[50] M. Fitz, "Further results in the fast estimation of a single frequency," *IEEE Transactions on Communications,* vol. 42, pp. 862-864, 1994.

[51] E. D. Moore, "Advances in Swept-Wavelength Interferometry for Precision Measurements," Boulder, CO, 2011.

[52] E. D. Moore and R. R. McLeod, "Correction of sampling errors due to laser tuning rate fluctuations in swept-wavelength interferometry," *Opt. Express,* vol. 16, no. 17, pp. 13139-13149, 2008.

[53] J. A. Stone, A. Stejskal and L. Howard, "Absolute interferometry with a 670-nm external cavity diode laser," *Applied Optics,* vol. 88, no. 28, pp. 5981-5994, 1999.

[54] P. A. Coe, D. F. Howell and R. B. Nickerson, "Frequency scanning interferometry in ATLAS: remote, multiple, simultaneous and precise distance measurements in a hostile environment," *Measurement Science and Technology,* vol. 15, no. 11, p. 2175, 2004.

[55] P. A. Coe, A. Mitra, S. M. Gibson, D. F. Howell and R. B. Nickerson, "Frequency Scanning Interferometry-A versatile high precision, multiple distance measurement technique," in *Proceedings of the Seventh International Workshop on Accelerator Alignment, SPRING8*, Japan, 2002.

[56] D. Xiaoli and S. Katuo, "High-accuracy absolute distance measurement by means of wavelength scanning heterodyne interferometry," *Measurement Science and Technology,* vol. 9, no. 7, p. 1031, 1998.

[57] H.-J. Yang, S. Nyberg and K. Riles, "High-precision absolute distance measurement using dual-laser frequency scanned interferometry under realistic conditions," *Nuclear Instruments and Methods in Physics Research Section A: Accelerators, Spectrometers, Detectors and Associated Equipment,* vol. 575, no. 3, pp. 395-401, 2007.

[58] K. Minoshima, K. Arai and H. Inaba, "High-accuracy self-correction of refractive index of air using two-color interferometry of optical frequency combs," *Optics Express,* vol. 19, no. 27, pp. 26095-26105, 2001.

[59] R. Roy and T. Kailath, "ESPRIT-estimation of signal parameters via rotational invariance techniques," *IEEE Transactions on Acoustics, Speech, and Signal Processing,* vol. 37, pp. 984-995, 1989.

[60] P. Stoica and N. Arye, "MUSIC, maximum likelihood, and the Cramer-Rao bound," *IEEE Transactions on Acoustics, Speech, and Signal Processing,* vol. 37, no. 5, pp. 720-741, 1989.

[61] C. Candan, "Fine resolution frequency estimation from three DFT samples: Case of windowed data," *Signal Processing,* vol. 114, pp. 245-250, 2015.

[62] P. Stoica, R. L. Moses, B. Friedlander and T. Soderstrom, "Maximum likelihood estimation of the parameters of multiple sinusoids from noisy measurements," *IEEE Transactions on Acoustics, Speech, and Signal Processing,* vol. 37, pp. 378-392, 1989.

[63] J. Shao, Mathematical Statistics, New York: Springer-Verlag New York, Inc., 1999.

[64] P. Stoica and A. Nehorai, "Statistical analysis of two nonlinear least-squares estimators of sine-wave parameters in the colored-noise case," *Circuits, System, and Signal Processing,* vol. 8, pp. 3-15, 1989.

[65] J. A. Nelder and R. Mead, "A Simplex Method for Function Minimization," *The Computer Journal,* vol. 7, no. 4, pp. 308-313, 1965.

[66] M. v. 8.1, Natick, MA: The Mathworks, Inc., 2013.

[67] The MathWorks, Inc. , "Tolerances and Stopping Criteria," R2017a. [Online]. Available: https://www.mathworks.com/help/optim/ug/tolerances-and-stopping-criteria.html. [Accessed 14 3 2017].

[68] R. Roy, A. Paulraj and T. Kailath, "Direction-of-arrival estimation by subspace rotation methods-ESPRIT," in *Acoustics, Speech, and Signal Processing, IEEE International Conference on ICASSP '86*, 1986.

[69] I. Santamaria, C. Pantaleon and J. Ibanez, "A comparitive study of high-accuracy frequency estimation methods," *Mechanical Systems and Signal Processing,* vol. 14, no. 5, pp. 819-834, 2000.

[70] R. O. Schmidt, "A signal subspace approach to multiple emitter location and spectral estimation," Palo Alto, CA, 1981.

[71] G. Bienvenu and L. Kopp, "Adaptivity to background noise spatial coherence for high resolution passive methods," in *Proceedings of the IEEE International Conference on Acoustics, Speech, and Signal Processing*, Denver, CO, 1980.

[72] C. Candan, "A Method For Fine Resolution Frequency Estimation From Three DFT Samples," *IEEE Signal Processing Letters,* vol. 18, no. 6, pp. 351-354, 2011.

[73] C. Candan, "Analysis and further improvement of fine resolution frequency estimation method from three DFT smaples," *IEEE Signal Processing Letters,* vol. 20, no. 9, pp. 913-916, 2013.

[74] B. G. Quinn, "Estimating frequency by interpolation using Fourier coefficients," *IEEE Transactions on Signal Processing,* vol. 42, no. 5, pp. 1264-1268, 1994.

[75] B. G. Quinn, "Estimation of frequency, amplitude, and phase from the DFT of a time series," *IEEE Transactions on Signal Processing,* vol. 45, no. 3, pp. 814-817, 1997.

[76] M. D. Macleod, "Fast nearly ML estimation of the parameters of real or complex single tones or resolved multiple tones," *IEEE Transactions on Signal Processing,* vol. 46, no. 1, pp. 141-148, 1998.

[77] E. Jacobsen and P. Kootsookos, "Fast,accurate frequency estimators," *IEEE Signal Processing Magazine,* vol. 24, pp. 123-125, 2007.

[78] S. Provencher, "Estimation of complex single-tone parameters in the DFT domain," *IEEE Transactions on Signal Processing,* vol. 58, no. 7, pp. 3879-3883, 2010.

[79] H. Rosenfeldt, C. Knothe, J. Cierullies and E. Brinkmeyer, "Evolution of amplitude and dispersion spectra during fiber Bragg grating fabrication," *Bragg Gratings, Photosensitivity, and Poling in Glass Waveguides, 2001 OSA Technical Digest Series,* p. paper BWA4, 2001.

[80] R. Huber, M. Wojtkowski, K. Taira, J. Fujimoto and K. Hsu, "Amplified, frequency swept lasers for frequency domain reflectometry and OCT imaging: design and scaling principles," *Optics Express,* vol. 13, pp. 3513-3528, 2005.

[81] P. A. Roos, R. R. Reibel, T. Berg, B. Kaylor, Z. W. Barber and W. R. Babbitt, "Ultrabroadband optical chirp linearization for precision metrology applications," *Optics Letters,* vol. 34, pp. 3692-3694, 2009.

[82] K. Iiyama, L. T. Wang and K. Hayashi, "Linearizing optical frequency-sweep of a laser diode for FMCW reflectometry," *Journal of Lightwave Technology,* vol. 14, pp. 173-178, 1996.

[83] S. Sherif, C. Flueraru, Y. Mao and S. Change, "Swept Source Optical Coherence Tomography with Nonuniform Frequency Domain Sampling," in *Proceedings Biomedical Optics*, St. Petersburg, FL, 2008.

[84] W. C. Swann and S. L. Gilbert, "Line centers, pressure shift, and pressure broadening of 1530-1560 nm hydrogen cyanide wavelength calibration lines," *Journal of the Optical Society of America B,* vol. 22, pp. 1749-1756, 2005.

[85] L. A. Goodman, "On the Exact Variance of Products," *Journal of the American Statistical Association,* vol. 55, pp. 708-713, 1960.

[86] H. Cramer, Mathematical Methods of Statistics, Princeton, NJ: Princeton University Press, 1946.

[87] C. R. Rao, "Information and the accuracy attainable in the estimation of statistical parameters," *Bulletin of the Calcutta Mathematical Society,* vol. 37, pp. 81-89, 1945.

[88] H. B. Lee, "The Cramer-Rao bond on frequency estimates of signals closely spaced in frequency," *IEEE Transactions on Signal Processing,* vol. 40, no. 6, pp. 1507-1517, 1992.

[89] B. Halder and T. Kailath, "Efficient estimation of closely spaced sinusoidal frequencies using subspace-based methods," *IEEE Signal Processing Letters,* vol. 4, no. 2, pp. 49-51, 1997.

[90] A. V. Oppenheim and R. W. Schafer, Discrete-Time Signal Processing, Second Edition ed., Upper Saddle River, New Jersey: Prentice-Hall, Inc., 1999.

[91] D. Wackerly, W. Mendenhall and R. L. Scheaffer, Mathematical Statistics with Applications, Belmont, CA: Thomson Higher Education, 2008.

[92] Y. Yasuno, V. D. Madjarova, S. Makita, M. Akiba, A. Morosawa, C. Chong, T. Sakai, K.-P. Chan, M. Itoh and T. Yatagai, "Three-dimensional and high-speed swept-source optical coherence tomography for in vivo investigation of human anterior eye segments," *Optics Express,* vol. 13, no. 26, pp. 10652-10664, 2005.

[93] T. Amano, H. Hiro-Oka, D. Choi, H. Furukawa, F. Kano, M. Takeda, M. Nakanishi, K. Shimizu and K. Ohbayashi, "Optical frequency-domain reflectometry with a rapid wavelength-scanning superstructure-grating distributed Bragg reflector laser," *Applied Optics,* pp. 808-816, 5 44 2005.

[94] S. Vankatesh and W. V. Sorin, "Phase noise considerations in coherent optical FMCW reflectometry," *Journal of Lightwave Technology,* vol. 11, no. 10, pp. 1694-1700, 1993.

[95] W. R. Bennett, "Spectra of quantized signals," *Bell Labs Technical Journal,* vol. 27, no. 3, pp. 446-472, 1948.

[96] R. M. Gray, "Quantization noise spectra," *IEEE Transactions on Information Theory,* vol. 36, no. 6, pp. 1220-1224, 1990.

[97] D. Marco and D. L. Neuhoff, "The validity of the additive noise model for uniform scalar quantizers," *IEEE Transactions on Information Theory,* vol. 51, no. 5, pp. 1739-1755, 2005.

[98] A. Papoulis, Probability, Random Variables, and Stochastic Processes, 2nd ed. ed., New York: McGraw-Hill, 1984.

[99] P. J. Wizner, "Shot-noise formula for time-varying photon rates: a general derivation," *Journal of the Optical Society of America B,* vol. 14, no. 10, pp. 2424-2429, 1997.

[100] T. M. Neibauer, R. Schiling, K. Danzmann, R. Albrecht and W. Winkler, "Nonstationary shot noise and its effect on the sensitivity of interferometers," *Physical Review A,* vol. 43, no. 9, p. 5022, 1991.

[101] B. K. Meers and K. A. Strain, "Modulation, signal, and quantum noise in interferometers," *Physical Review A,* vol. 44, no. 7, p. 4693, 1991.

[102] H. K. Kang, H. J. Bang, C. S. Hong and C. B. Kim, "Simultaneous measurement of strain, temperature and vibration frequency using a fibre optic sensor," *Measurement Science and Technology,* vol. 13, no. 8, p. 1191, 2002.

[103] H.-J. Yang, S. Nyberg and K. Riles, "High-precision absolute distance and vibration measurement with frequency scanned interferometry," *Applied Optics,* vol. 44, no. 19, pp. 3937-3944, 2005.

[104] S. Wang, Q. Liu and Z. He, "Distributed fiber-optic vibration sensing based on phase extraction from time-gated digital OFDR," *Optics Express,* vol. 23, no. 26, pp. 33301-33309, 2015.

[105] E. Brinkmeyer and U. Glombitza, "High-resolution coherent frequency-domain reflectometry using continuously tuned laser diodes," *Optical Fiber Communication Conference, OSA Technical Digest Series,* vol. vol. 4, p. paper WN2, 1991.

[106] G. Ulrich and E. Brinkmeyer, "Coherent frequency-domain reflectometry for characterization of single-mode integrated-optical waveguides," *Journal of Lightwave Technology,* vol. 11, no. 8, pp. 1377-1384, 1993.

[107] M. Krzywinski and N. Altman, "Points of Significance: Error Bars," *Nature Methods,* vol. 10, pp. 921-922, 2013.

[108] G. Ghosh, M. Endo and T. Iwasaki, "Temperature-Dependent Sellmeier Coefficients and Chromatic Dispersions for Some Optical Fiber Glasses," *Journal of Lightwave Technology,* vol. 12, no. 8, pp. 1338-1342, 1994.

[109] D. B. Leviton and B. J. Frey, "Temperature-dependent absolute refractive index measuremets of synthetic fused silica," *SPIE Astronomica Telescopes + Instrumentation,* p. 62732K, 2006.

[110] P. E. Ciddor, "Refractive index of air: new equations for the visible and near infrared," *Appl. Opt.,* vol. 35, no. 9, pp. 1566-1573, 1996.

[111] B. Edlen, "The refractive index of air," *Metrologia,* vol. 2, pp. 71-80, 1966.

[112] K. P. Birch and M. J. Downs, "An updated Edlen equation for the refractive index of air," *Metrologia,* vol. 31, pp. 155-162, 1993.

[113] K. P. Birch and M. J. Downs, "Correction to the updated Edlen equation for the refractive index of air," *Metrologia,* vol. 31, pp. 315-316, 1994.

[114] J. A. Stone and J. H. Zimmerman, "Engineering metrology toolbox," 2011. [Online]. Available: http://emtoolbox.nist.gov/Wavelength/Edlen.asp. [Accessed 30 3 2017].

[115] R. Passy, N. Gisin, J. P. von der Weid and H. H. Gilgen, "Experimental and Theoretical Investigations of Coherent OFDR with Semiconductor Laser Sources," *Journal of Lightwave Technology,* vol. 12, no. 9, pp. 1622-1630, 1994.

[116] Z. Ding, D. Yang, Y. Du, K. Liu, Y. Zhou, R. Zhang, Z. Xu, J. Jiang and T. Liu, "Distributed Strain and Temperature Discrimination Using Two Types of Fiber in OFDR," *IEEE Photonics Journal,* vol. 8, no. 5, pp. 1943-0655, 2016.

[117] Y. Du, T. Liu, Z. Ding, Q. Han, K. Liu, J. Jiang, Q. Chen and B. Feng, "Cryogenic Temperature Measurement Using Rayleight Backscattering Spectra Shfit by OFDR," *IEEE Photonics Technology Letters,* vol. 26, no. 11, pp. 1150-1153, 2014.

[118] A. K. Sang, M. E. Froggatt, D. K. Gifford, S. T. Kreger and B. D. Dickerson, "One Centimeter Spatial Resolution Temperature Measurements in a Nuclear Reactor Using Ralyleigh Scatter in Optical Fiber," *IEEE Sensors Journal,* vol. 8, no. 7, pp. 1375-1380, 2008.

[119] A. Faustov, A. Gussarov, M. Wuilpart, A. A. Fotiadi, L. B. Liokumovich, O. I. Kotov, I. O. Zolotovskiy, A. L. Tomashuk, T. Deschoutheete and P. Megret, "Distributed optical fibre temperature measurements in a low dose rate environment based on Rayleigh backscattering," in *Proceedings of SPIE, Optical Sensing and Detection II, 84390C*, 2012.

[120] Y. Yasuno, V. D. Madjarova, S. Makita, M. Akiba, A. Morosawa, C. Chong, T. Sakai, K. P. Chan, M. Itoh and T. Yatagai, "Three-dimensional and high-speed swept-source optical coherence tomography for in vivo investigation of human anterior eye segments," *Optics Express,* vol. 13, no. 26, pp. 10652-10664, 2005.

[121] G. Quellec, K. Lee, M. Dolejsi, M. K. Garvin, M. D. Abramoff and M. Sonka, "Three-dimensional analysis of retinal layer texture: identification of fluid-filled regions in SD-OCT of the macula," *IEEE transactions on medical imaging,* vol. 29, no. 6, pp. 1321-1330, 2010.

[122] T. P. Lynch, B. W. Myer, K. Medicus and J. D. Nelson, "Deterministic form correction of extreme freeform optical surfaces," in *Proceedings of SPIE 9633, Optifab 2015*, 2015.

[123] J. D. Nelson, K. Medicus and G. Frisch, "Tolerancing an optical freeform surface: an optical fabricator's perspective," in *Proceedings SPIE, Current Developments in Lens Design and Optical Engineering XVI*, 2015.

[124] J. Gerd, E. Manske and T. Hausotte, "Nanopositioning and measuring machine," in *euspen: european society for precision engineering and nanotechnology. International conference*, 2001.

[125] E. B. Hughes, A. Wilson and G. N. Peggs, "Design of a High-Accuracy CMM Based on Multi-Lateration Techniques," *CIRP Annals - Manufacturing and Technology,* vol. 49, no. 1, pp. 391-394, 2000.

[126] C. Meng and F. L. Chen, "Curve and surface approximation from CMM measurement data," *Computers & Industrial Engineering,* vol. 30, no. 2, pp. 211-225, 1996.

[127] P. Murphy, G. Forbes, J. Fleig, P. Dumas and M. Tricard, "Stitching Interferometry: A Flexible Solution for Surface Metrology," *Optics and Photonics News,* vol. 14, no. 5, pp. 38-43, 2003.

[128] S. Chen, S. Li and Y. Dai, "Interative algorithm for subaperature stitching interferometry," *Journal of the Optical Society of America,* vol. 22, no. 9, pp. 1929-1936, 2005.

[129] M. C. Kneuer, J. Kaminski and G. Hausler, "Phase measuring deflectometry: a new approach to measure specular free-form surfaces," *Photonics Europe,* pp. 366-376, 2004.

[130] Y. Tang, X. Su, Y. Liu and H. Jing, "3D shape measurement of the aspheric mirror by advanced phase measuring deflectometry," *Optics Express,* vol. 16, no. 19, pp. 15090-15096, 2008.

[131] S. Xianyu and Q. Zhang, "Dynamic 3-D shape measurement method: a review," *Optics and Lasers in Engineering,* vol. 48, no. 2, pp. 191-204, 2010.

[132] J. Geng, "Structured-light 3D surface imaging: a tutorial," *Advances in Optics and Photonics,* vol. 3, no. 2, pp. 128-160, 2011.

[133] R. Tutsch, M. Petz and M. Fischer, "Optical three-dimensional metrology with structured illumination," *Optical Engineering,* vol. 50, no. 10, p. 101507, 2011.

[134] F. Chen, G. M. Brown and M. Song, "Overview of three-dimensional shape measurement using optical methods," *Optical Engineering,* vol. 39, no. 1, pp. 10-22, 2000.

[135] G. E. Sommargren, "Optical heterodyne profilometry," vol. 20, no. 4, pp. 610-618, 1981.

[136] V. Carbone, M. Carocci, E. Savio, G. Sansoni and L. De Chiffre, "Combination of a vision system and a coordinate measuring machine for the reverse engineering of freeform surfaces," *The International Journal of Advanced Manufacturing Technology,* vol. 17, no. 4, pp. 263-271, 2001.

[137] P. E. Murphy, J. Fleig, G. Forbes and M. Tricard, "High precision metrology of domes and aspheric optics," in *Proceedings SPIE 5786, Window and Dome Technologies and Materials IX*, 2005.

[138] J. H. Burge, "Applications of computer-generated holograms for interferometric measurement of large aspheric optics," in *Proceedings SPIE*, 1995.

[139] C. Pruss, S. Teichelt, H. J. Tiziani and W. Osten, "Computer-generated holograms in interferometric testing," *Optical Engineering,* vol. 43, no. 11, pp. 2534-2540, 2004.

[140] H. Shen, R. Zhu, Z. Gao, E. Y. B. PUN, W. H. Wong and X. Zhu, "Design and fabrication of computer-generated holograms for testing optical freeform surfaces," *Chinese Optics Letters,* vol. 11, no. 3, p. 032201, 2013.

[141] A. G. Poleshcuk, R. K. Nasyrov and J. M. Asfour, "Combined computer-generated hologram for testing steeep aspheric surfaces," *Optics Express,* vol. 17, no. 7, pp. 5420-5425, 2009.

[142] J.-M. Asfour and A. G. Poleshchuk, "Asphere testing with a Fizeau interferometer based on a combined computer-generated hologram," *Journal of the Optical Society of America A,* vol. 23, no. 1, pp. 172-178, 2006.

[143] G. S. Khan, "Characterization of Surface Roughness and Shape Deviations of Aspheric Surfaces," University of Erlangen-Nuremberg, 2008.

[144] Y. Zhao, P. Li, C. Wang and Z. Pu, "A novel fiber-optic sensor used for small internal curved surface measurement.," *Sensors and actuators A: Physical,* vol. 86, no. 3, pp. 211-215, 2000.

[145] Y. Zhao, P. Li and Z. Pu, "Shape measurement based on fiber-optic technique for complex internal surface," *Measurement,* vol. 30, no. 4, pp. 289-295, 2001.

[146] K. D. Rao, D. V. Udupa, C. Prathap, A. Rathod, R. Balasubramaniam and N. K. Sahoo, "Optical coherence tomography for shape and radius of curvature measurements of deeply curved machined metalic surfaces: a comparison with two-beam laser interferometry," *Optics and Laser in Engineering ,* vol. 66, pp. 204-209, 2015.

[147] B. K. Goud, D. V. Udupa, C. Prathap, D. D. Shinde, K. D. Rao and N. K. Sahoo, "Noncontact three-dimensional quantitative profiling of fast aspheric lenses by optical coherence tomography," *Advanced Optical Technologies,* vol. 5, no. 5-6, pp. 451-459, 2016.

[148] B. E. A. Saleh and M. C. Teich, Fundamentals of Photonics, 2nd ed. ed., New York: Wiley, 1991.

[149] OZ Optics Ltd., "OZOptics," [Online]. Available: http://www.ozoptics.com/ALLNEW_PDF/DTS0083.pdf. [Accessed 10 04 2017].

[150] A. Ghatak and K. Thyagarajan, An Introduction to Fiber Optics, Cambridge University Press, 1998.

[151] N. Alstshiller-Court, College Geometry: An Introduction to the Modern Geometry of the Triangle and the Circle, 2nd ed. ed., New York: Barnes and Noble, 1952.

[152] M. v. 9.1.0, Natick: The Mathworks, Inc., 2016.

[153] A. B. Mateo and Z. W. Barber, "Multi-dimensional, non-contact metrology using trilateration and high resolution FMCW ladar," *Applied Optics,* vol. 54, no. 19, pp. 5911-5916, 2015.

[154] B. Bradie, A Friendly Introduction to Numerical Analysis, Upper Saddle River, NJ: Pearson Prentice Hall, 2006.

[155] M. Abramowitz and I. A. Stegun, Handbook of Mathematical Functions with Formulas, Graphs, and Mathematical Tables., vol. 55, New York, United States Department of Commerce, National Bureau of Standards: Dover Publications, 1964, p. 355.

[156] C. Candan, "Publications of Prof. Cagatay Candan, Middle East Tecnhical University, Deptartment of Electrical Engineering," 10 2013. [Online]. Available: users.metu.edu.tr/ccandan/pub_dir/correction_factor.m. [Accessed May 2017].

[157] K. E. Atkinson, An Inroduction to Numerical Analysis, 2nd ed. ed., New York: John Wiley & Sons, 1989.

[158] R. G. Lyons, "Reducing FFT Scalloping Loss Errors Without Multiplication," *IEEE Signal Processing Magazine,* vol. 28, no. 2, pp. 112-116, 2011.

[159] F. J. Harris, "On the Use of Windows for Harmonic Analysis with the Discrete Fourier Transform," *Proceedings of the IEEE,* vol. 66, no. 1, pp. 51-83, 1978.

[160] D. C. Rife and R. R. Boorstyn, "Multiple Tone Parameter Estimation From Discrete-Time Observations," *Bell Labs Technical Journal,* vol. 55, no. 9, pp. 1389-1410, 1976.

[161] G. Moschetti, A. Forbes, R. K. Leach, X. Jiang and D. O'Conner, "Quadrature wavelength scanning interferometry," *Applied Optics,* vol. 55, no. 20, pp. 5332-5340, 2016.

[162] X. Jiang, K. Wang, F. Gao and H. Muhamedsalih, "Fast surface measurement using wavelength scanning interferometry with compensation of environmental noise," *Applied Optics,* vol. 49, no. 15, pp. 2903-2909, 20101.

[163] F. Gao, H. Muhamedsalih and X. Jian, "Surface and thickness measurement of a transparent film using wavelength scanning interferometry," *Optics Express,* vol. 20, no. 19, pp. 21450-21456, 2012.

Appendix A

Derivation of Equation for Vibrational Sidelobes

Here, I present the derivation of Equation (3.1). The derivation here closely resembles the work presented in [19]. I have modified the notation to match the rest of the work presented in this thesis, and explicitly noted the inclusion of assumptions upon which Equation (3.1) depends.

To begin, consider a Michelson-geometry SWI system in which the sample arm contains only one reflector. If the sample arm is disturbed by mechanical vibration, the electric field *E* at the photodetector is given by

$$E[\nu(t)] = \sqrt{a}\sqrt{1-a}E_0 e^{-j2\pi\nu(t)\tau_R} + \sqrt{a}\sqrt{1-a}\sqrt{R_s}E_0 e^{-j[2\pi\nu(t)\tau_S + A\sin(2\pi f_m t)]} \,. \quad \text{(A.1)}$$

The electric field *E* is a function of the time-varying instantaneous optical frequency ν, and its amplitude E_0 is assumed to be constant across the laser sweep. The time delays of the reference and sample arms are given by τ_R and τ_S, respectively. The reflectivity of the single reflector in the sample arm is given by R_S. The coupling ratio *a* of the optical coupler may take on values between 0 and 1. For a 3 dB coupler, its value would be 0.5.

Mechanical vibration induces a periodic variation of the phase in the sample arm of the SWI. This is represented by the term $A\sin(2\pi f_m t)$, where *A* is the amplitude of the vibration-induced phase variation and f_m is its frequency.

Using the Jacobi-Anger expansion [155], the exponential term with a sine as its argument can be expressed as a sum of Bessel functions of the first kind, so

$$e^{-jA\sin(2\pi f_m t)} = \sum_{n=-\infty}^{n=\infty} J_n(A) e^{-j2\pi n f_m t}\,. \tag{A.2}$$

In Figure A.1, orders zero through four of the Bessel functions are plotted.

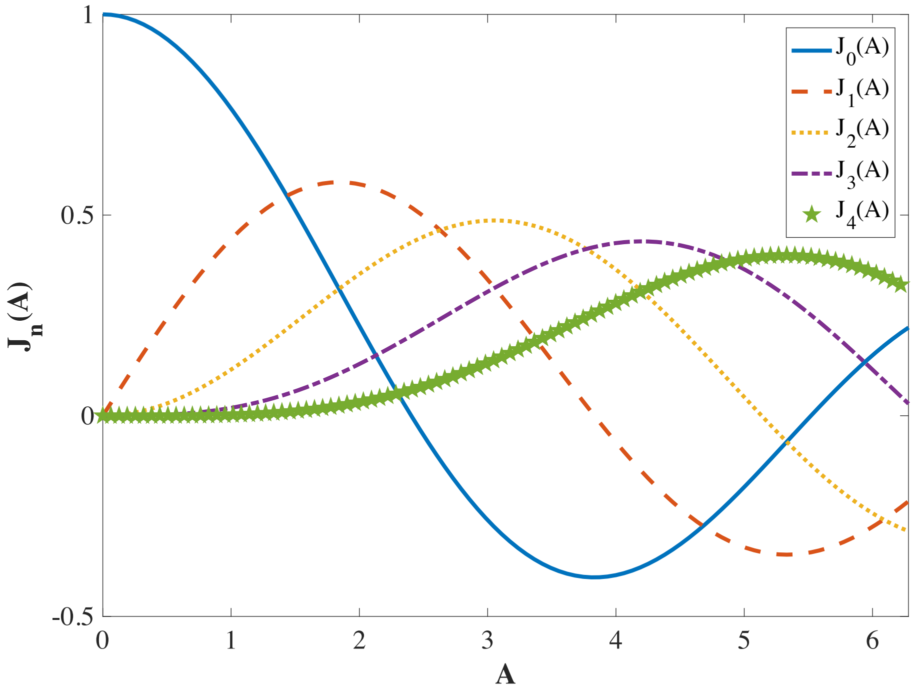

Figure A.1 Bessel functions of the first kind for orders 0, 1, 2, 3, and 4. For small vibration amplitudes A*, the values of second and higher order Bessel functions are negligible.*

Provided vibration amplitude A is small, then Equation (A.2) is well-approximated by its zeroth-order and first-order terms,

$$e^{-jA\sin(2\pi f_m t)} \approx J_0(A) + J_1(A)e^{-j2\pi f_m t} - J_1(A)e^{j2\pi f_m t}\,. \tag{A.3}$$

In this case, Equation (A.3) can be rewritten as

$$\begin{aligned} E[\nu(t)] = {} & \sqrt{a}\sqrt{1-a}E_0 e^{-j2\pi\nu(t)\tau_R} \\ & + \sqrt{a}\sqrt{1-a}\sqrt{R_{s_s}}E_0 e^{-j[2\pi\nu(t)\tau_S]}\big[J_0(A) + J_1(A)e^{-j2\pi f_m t} \\ & - J_1(A)e^{j2\pi f_m t}\big] \,. \end{aligned} \tag{A.4}$$

The intensity at the photodetector is given by the squared modulus of the electric field, so

$$\begin{aligned} I[\nu(t)] = {} & \big|\sqrt{a}\sqrt{1-a}E_0 e^{-j2\pi\nu(t)\tau_R} \\ & + \sqrt{a}\sqrt{1-a}\sqrt{R_s}E_0 e^{-j[2\pi\nu(t)\tau_S]}\big[J_0(A) + J_1(A)e^{-j2\pi f_m t} \\ & - J_1(A)e^{j2\pi f_m t}\big]\big|^2 \,. \end{aligned} \tag{A.5}$$

By representing the time delay difference between the two arms of the SWI as

$$\tau_0 = \tau_S - \tau_R \,, \tag{A.6}$$

Equation (A.5) can be expanded to become

$$
\begin{aligned}
I[\nu(t)] = {} & a(1-a)I_0 + a(1-a)R_S I_0 [J_0^2(A) + 2J_1^2(A)] \\
& + a(1-a)\sqrt{R_S} J_0(A) I_0 e^{j2\pi\nu(t)\tau_0} \\
& + \ a(1-a)\sqrt{R_S} J_0(A) I_0 e^{-j2\pi\nu(t)\tau_0} \\
& + a(1-a)\sqrt{R_S} J_1(A) I_0 e^{j2\pi\nu(t)\tau_0} e^{j2\pi f_m t} \\
& \qquad + a(1-a)\sqrt{R_S} J_1(A) I_0 e^{-j2\pi\nu(t)\tau_0} e^{-j2\pi f_m t} \\
& - a(1-a)\sqrt{R_S} J_1(A) I_0 e^{j2\pi\nu(t)\tau_0} e^{-j2\pi f_m t} \\
& \qquad - a(1-a)\sqrt{R_S} J_1(A) I_0 e^{-j2\pi\nu(t)\tau_0} e^{j2\pi f_m t} \\
& + a(1-a)R_S J_0(A) J_1(A) I_0 e^{j2\pi f_m t} \\
& + a(1-a)R_S J_0(A) J_1(A) I_0 e^{-j2\pi f_m t} \\
& - a(1-a)R_S J_0(A) J_1(A) I_0 e^{-j2\pi f_m t} \\
& - a(1-a)R_S J_0(A) J_1(A) I_0 e^{j2\pi f_m t} \\
& - a(1-a)R_S J_1^2(A) I_0 e^{-j2\pi 2 f_m t} - a(1-a)R_S J_1^2(A) I_0 e^{j2\pi 2 f_m t} .
\end{aligned}
\tag{A.7}
$$

If the laser sweep rate is assumed to be linear, with sweep rate γ, then the instantaneous optical frequency $\nu(t)$ can be expressed as

$$\nu(t) \approx \nu_0 + \gamma t \, , \tag{A.8}$$

and time *t* can be written as a function of instantaneous optical frequency, i.e.

$$t = \frac{\nu_0 - \nu(t)}{\gamma} . \tag{A.9}$$

After substituting Equation (A.9) into Equation (A.7), simplifying, and applying Euler's identity, detected intensity *I* is given by

$$
\begin{aligned}
I[\nu] = {} & a(1-a)I_0 + a(1-a)R_S I_0[J_0^2(A) + 2J_1^2(A)] \\
& + 2a(1-a)\sqrt{R_S}J_0(A)I_0\cos(2\pi\nu(t)\tau_0) \\
& + a(1-a)\sqrt{R_S}J_1(A)I_0 e^{j2\pi f_m\frac{\nu_0}{\gamma}} e^{j2\pi\nu\left[\tau_0-\frac{f_m}{\gamma}\right]} \\
& \quad + a(1-a)\sqrt{R_S}J_1(A)I_0 e^{-j2\pi f_m\frac{\nu_0}{\gamma}} e^{-j2\pi\nu\left[\tau_0-\frac{f_m}{\gamma}\right]} \\
& - a(1-a)\sqrt{R_S}J_1(A)I_0 e^{-j2\pi f_m\frac{\nu_0}{\gamma}} e^{j2\pi\nu\left[\tau_0+\frac{f_m}{\gamma}\right]} \\
& \quad - a(1-a)\sqrt{R_S}J_1(A)I_0 e^{j2\pi f_m\frac{\nu_0}{\gamma}} e^{-j2\pi\nu\left[\tau_0+\frac{f_m}{\gamma}\right]} \\
& - a(1-a)R_S J_1^2(A)I_0 e^{-j2\pi 2f_m\frac{\nu_0}{\gamma}} e^{j2\pi\nu\frac{2f_m}{\gamma}} \\
& \quad - a(1-a)R_S J_1^2(A)I_0 e^{-j2\pi 2f_m\frac{\nu_0}{\gamma}} e^{j2\pi\nu\frac{2f_m}{\gamma}} .
\end{aligned}
\tag{A.10}
$$

Taking the Fourier transform of Equation (A.10) gives the following expression:

$$
\begin{aligned}
\tilde{I}[\tau] = {} & \{a(1-a)I_0 + a(1-a)R_S I_0[J_0^2(A) + 2J_1^2(A)]\}\delta(0) \\
& + a(1-a)\sqrt{R_S}J_0(A)I_0\{\delta(\tau-\tau_0) + \delta(\tau+\tau_0)\} \\
& + a(1-a)\sqrt{R_S}J_1(A)I_0\left\{e^{j2\pi f_m\frac{\nu_0}{\gamma}}\delta\left[\tau-\left(\tau_0-\frac{f_m}{\gamma}\right)\right]\right. \\
& + e^{-j2\pi f_m\frac{\nu_0}{\gamma}}\delta\left[\tau+\left(\tau_0-\frac{f_m}{\gamma}\right)\right] + e^{-j2\pi f_m\frac{\nu_0}{\gamma}}\delta\left[\tau-\left(\tau_0+\frac{f_m}{\gamma}\right)\right] \\
& \left. + e^{j2\pi f_m\frac{\nu_0}{\gamma}}\delta\left[\tau+\left(\tau_0+\frac{f_m}{\gamma}\right)\right]\right\} \\
& - (1-a)^2 R_S J_1^2(A)I_0\left\{e^{-j2\pi 2f_m\frac{\nu_0}{\gamma}}\delta\left(\tau-\frac{2f_m}{\gamma}\right)\right. \\
& \left. + e^{-j2\pi 2f_m\frac{\nu_0}{\gamma}}\delta\left(\tau+\frac{2f_m}{\gamma}\right)\right\}.
\end{aligned}
\tag{A.11}
$$

Both sidebands contain reflection peaks, centered at $\tau = \pm\tau_0$. If the vibrational amplitude *A* is nonzero, each reflection peak has two sidelobes spaced from their main peak by a delay times determined by the vibrational frequency f_m and the laser sweep rate γ. The stronger the vibrational amplitude A, the more the energy in the main lobe is transferred into the sidelobes, and the lower the vibrational frequency f_m, the closer the sidelobes are to the main lobe in delay time.

Mechanical vibration also causes sidelobes to appear on either side of the DC term; however, the amplitude of these sidelobes is proportional to the square of the value of the first-order Bessel function, and provided the assumption that vibrational amplitude A is small holds, the amplitude of these sidelobes is negligible. Dropping these squared terms and rearranging gives

$$\begin{aligned}
\tilde{I}[\tau] = {} & \{a^2 I_0 + (1-a)^2 R_S I_0 [J_0^2(A) + 2J_1^2(A)]\}\delta(0) \\
& + a(1-a)\sqrt{R_S} J_0(A) I_0\, \delta(\tau - \tau_0) \\
& \quad + a(1-a)\sqrt{R_S} J_1(A) I_0 \left\{ e^{j2\pi f_m \frac{\nu_0}{\gamma}} \delta\left[\tau - \left(\tau_0 - \frac{f_m}{\gamma}\right)\right] \right. \\
& \quad \left. + e^{-j2\pi f_m \frac{\nu_0}{\gamma}} \delta\left[\tau - \left(\tau_0 + \frac{f_m}{\gamma}\right)\right] \right\} \\
& + a(1-a)\sqrt{R_S} J_0(A) I_0\, \delta(\tau + \tau_0) \\
& \quad + a(1-a)\sqrt{R_S} J_1(A) I_0 \left\{ e^{-j2\pi f_m \frac{\nu_0}{\gamma}} \delta\left[\tau + \left(\tau_0 - \frac{f_m}{\gamma}\right)\right] \right. \\
& \quad \left. + e^{j2\pi f_m \frac{\nu_0}{\gamma}} \delta\left[\tau + \left(\tau_0 + \frac{f_m}{\gamma}\right)\right] \right\}.
\end{aligned} \tag{A.12}$$

A final simplification is achieved by dropping the terms in the negative sideband, assuming that coupling ratio a is equal to 0.5, and multiplying the entire expression by 4; this results, at last, in Equation (3.1):

$$\begin{aligned}\tilde{I}[\tau] = {} & \{I_0 + R_S I_0 [J_0^2(A) + 2J_1^2(A)]\}\delta(0) \\ & + \sqrt{R_S} J_0(A) I_0 \, \delta(\tau - \tau_0) \\ & + \sqrt{R_S} \, J_1(A) I_0 \left\{ e^{j2\pi f_m \frac{\nu_0}{\gamma}} \delta\left[\tau - \left(\tau_0 - \frac{f_m}{\gamma}\right)\right] \right. \\ & \left. + e^{-j2\pi f_m \frac{\nu_0}{\gamma}} \delta\left[\tau - \left(\tau_0 + \frac{f_m}{\gamma}\right)\right] \right\}. \end{aligned} \tag{A.13}$$

Appendix B

Matlab Code for Numerical Model

B.1 Nonlinear Least Squares (NLS)

B.1.1 Script for evaluating the precision of NLS estimates

```
% NLSNoise.m
% Script to calculate precision of Nonlinear Least Squares (NLS) estimates
% of the delay time between two reflectors of equal amplitude.  Simulation
% parameters are defined in two blocks, between dashed lines in the first
% section.
%
% Author: Martha I. Bodine
% Date: 22 May 2017
%
% Ref: Stoica, Petre, and Randolph L. Moses. Spectral analysis of signals.
% Vol. 452. Upper Saddle River, NJ: Pearson Prentice Hall, 2005.
%*************************************************************************
%% Set sampling conditions

% Physical constants
c0          = 299792458;    % light speed [m/s]

% SIMULATION PARAMETERS, PART 1 -------------------------------------------
lambda1     = 1500e-9;      % sweep start wavelength [m]
lambda2     = 1505e-9;      % sweep end wavelength [m]
tau_t       = 100e-9;       % trigger delay time [s]
tau1        = tau_t/4;      % delay time to first reflector [s]
% -----------------------------------------------------------------------

% Calculate vector of optical frequencies
nu1 = c0/lambda1;   % start frequency [Hz]
nu2 = c0/lambda2;   % end frequency [Hz]
N   = round((nu1 - nu2)*tau_t); % number of samples

nu  = nu1 - (0:N-1).'/tau_t;    % vector of optical frequencies [Hz]
nu  = fliplr(nu);

dnu = nu(1)-nu(2);  % spacing between samples in frequency [Hz]
dtau   = tau_t/N;    % spacing between samples in delay time [s]

% SIMULATION PARAMETERS, PART 2 -------------------------------------------
% vector of delay times to second reflector[s]
tau2   = (tau1 + (5000:5001)*dtau).';
```

```
% SNR levels to test (This is SNR in the delay time domain.)
SNR     = 10:10:110;

% Number of simulations to run at each SNR
Nnoise  = 30;

w   = hann(N);  % Define window function
% ---------------------------------------------------------------------------

%****************************************************************************
%% NLS estimation

% Preallocate space for errors and elapsed time
tau1r   = zeros(numel(tau2),numel(SNR),Nnoise);
tau2r   = zeros(numel(tau2),numel(SNR),Nnoise);
etime   = zeros(numel(tau2),numel(SNR),Nnoise);

% Define variables to track execution percentage
ti  = numel(tau2)*numel(SNR)*Nnoise;    % total number of iterations
I   = 0;    % completed iterations

% Convert SNR from delay time domain to optical frequency domain.
SNR     = SNR - 10*log10(N);

% Run simulations
for ij = 1:numel(tau2)
    for jk  = 1:numel(SNR)
        for kl = 1:Nnoise

            % Start the timer
            tic

            % Calculate the sampled signal from the measurement
            % interferometer
            u   = 2 + cos(2*pi*nu*tau1) + cos(2*pi*nu*tau2(ij));

            % Add white Gaussian noise
            u   = awgn(u,SNR(jk),'measured');

            % FFT to find transform-limited delay times
            U   = fft(u);

            % FT resolved peak centers
            p1      = round(tau1/dtau) + 1;
            p2      = round(tau2(ij)/dtau) + 1;

            % Scale initial guesses for NLS
            scale_factor = 2*pi*dnu*dtau;
            tau1_scaled  = p1*scale_factor;
            tau2_scaled  = p2*scale_factor;

            % Vector of initial guesses for both sidebands
            tau_guess   = [-tau2_scaled, -tau1_scaled, 0, tau1_scaled, ...
                            tau2_scaled];

            % Options in for Nelder-Mead Simplex search
            options = optimset('TolX', scale_factor*10e20);
```

```
            % Search using Nelder-Mead simplex
            [tauNLS,~,~] = fminsearchSmallSimplex(@(tau) nls( tau, U ),...
                                                    tau_guess, options);

            % Record error
            tau1r(ij,jk,kl)  = tauNLS(end-1)/(2*pi*dnu);
            tau2r(ij,jk,kl)  = tauNLS(end)/(2*pi*dnu);

            % Record elapsed time
            etime(ij,jk,kl)     = toc;

            % Update counting variable
            I   = I + 1;

            % Display completion percentage every 100 iterations
            if mod(I,100) == 0
                disp(I/ti*100)
            end

        end

    end

end
```

B.1.2 Subroutine for NLS optimization method

```
function Q = nls( tau, U )
%---------------------------------------------------------------------------
% The NLS optimization method for frequency estimation.
%
% INPUTS:   tau -  vector of guesses for frequencies/delay times in data
%                  vector U
%           U   -  the data vector
%
% OUTPUTS:  w   - the frequency estimates
%
% Author: Martha I. Bodine
% Date: 22 May 2017
%
% Ref: Stoica, Petre, and Randolph L. Moses. Spectral analysis of signals.
% Vol. 452. Upper Saddle River, NJ: Pearson Prentice Hall, 2005.
%
%---------------------------------------------------------------------------


% Make sure that the signal vector U is a column vector.
U = U(:);

% Number of samples
N   = numel(U);

% Number of frequencies (reflectors)
n   = numel(tau);

% Make sure the vector of frequency (delay time) guesses is a row
```

```
% vector.
tau = tau(:).';

% Matrix of powers
powers  = repmat((1:N)',1,n);

% Matrix B (see Stoica, Nonlinear Least Squares Method)
B   = repmat( exp( 1i*tau ) , N , 1) .^ powers;

% Clear space in memory
clear powers

% Calculate output.  This quantity should be maximized to estimate
% frequencies.
Q   = U'*B*( (B'*B)^-1 )*B'*U;

% Flip the value of f so to switch from a maximization to a minimization
% problem.  Keep only the real part.
Q   = -1*real(Q);


end
```

B.1.3 Notes on modification of MATLAB function *fminsearch*

The script provided in Section B.1.1 included a call to a Matlab function titled *fminsearchSmallSimplex*. This function is a modified version of Matlab's Nelder-Mead optimization function *fminsearch*. Lines 257 and 258 of the original function define the initial size of the simplex and are as follows:

```
usual_delta = 0.05;            % 5 percent deltas for non-zero terms
zero_term_delta = 0.00025;     % Even smaller delta for zero elements of x
```

These lines must be altered so that the optimizer does not leave the vicinity of the global maximum during the first iteration of the search process. The lines in the modified function *fminsearchSmallSimplex* are:

```
usual_delta = 1e-7;
zero_term_delta = 5e-10;
```

B.2 ESPRIT

B.2.1 Script for evaluating the precision of ESPRIT estimates

```
% ESPRITNoise.m
% Script to calculate precision of ESPRIT estimates of the delay time
% between two reflectors of equal amplitude.  Simulation parameters are
% defined in two blocks, between dashed lines in the first section.
%
% Author: Martha I. Bodine
% Date: 22 May 2017
%
% Ref: Santamaria, Ignacio, Carlos Pantaleon, and Jesus Ibanez.
% "A comparative study of high-accuracy frequency estimation methods."
% Mechanical Systems and Signal Processing, vol. 14, no. 5, p. 819-834.
% (2000).
%
%***************************************************************************
%% Set sampling conditions

% Physical constants
c0          = 299792458;    % light speed [m/s]

% SIMULATION PARAMETERS, PART 1 -----------------------------------------
lambda1     = 1500e-9;      % sweep start wavelength [m]
lambda2     = 1570e-9;      % sweep end wavelength [m]
tau_t       = 100e-9;       % trigger delay time [s]
tau1        = tau_t/4;      % delay time to first reflector [s]
% -------------------------------------------------------------------------

% Calculate vector of optical frequencies
nu1 = c0/lambda1;   % start frequency [Hz]
nu2 = c0/lambda2;   % end frequency [Hz]
N   = round((nu1 - nu2)*tau_t); % number of samples

nu  = nu1 - (0:N-1).'/tau_t;    % vector of optical frequencies [Hz]
nu  = fliplr(nu);

dnu = nu(1)-nu(2);  % spacing between samples in frequency [Hz]
dtau   = tau_t/N;    % spacing between samples in delay time [s]

% SIMULATION PARAMETERS, PART 2 -----------------------------------------
% vector of delay times to second reflector[s]
tau2   = (tau1 + dtau/2+(20:10:30)*dtau).';

% SNR levels to test (This is SNR in the delay time domain.)
SNR     = 10:100:110;

% Number of simulations to run at each SNR
Nnoise  = 2;

% Set parameters for ESPRIT
n       = 2;    % Number of frequencies in real-valued signal
m       = 100;  % order of covariance matrix
B       = 1;    % interleaving factor
% -------------------------------------------------------------------------
```

```
%**************************************************************************
%% ESPRIT

% Preallocate space for errors and elapsed time
tau1r   = zeros(numel(tau1),numel(SNR),Nnoise);
tau2r   = zeros(numel(tau1),numel(SNR),Nnoise);
etime   = zeros(numel(tau1),numel(SNR),Nnoise);

% Define variables to track execution percentage
ti  = numel(tau2)*numel(A2)*Nnoise;    % total number of iterations
I   = 0;    % completed iterations

% Convert SNR from delay time domain to optical frequency domain.
SNR     = SNR - 10*log10(N);

% Run the simulations
for ij = 1:numel(tau2)
    for jk  = 1:numel(SNR)
        for kl = 1:Nnoise

                % Start the timer
                tic

                % Calculate sampled signal from measurement interferometer
                U   = 2 + cos(2*pi*nu*tau1) + cos(2*pi*nu*tau2(ij));

                % Add white Gaussian noise
                U   = awgn(U,SNR(jk),'measured');

                % Make data complex
                U   = ifft(fft(U));

                % Get ESPRIT delay time estimates
                w   = espritCF(U,2*n+2,m,B);

                % Scale delay time estimates
                w   = w/(2*pi*dnu*B);

                % Record error.  Don't know order of ESPRIT estimates, so
                % record minimum error.
                [~,a]               = min(abs(tau1 - w));
                tau1r(ij,jk,kl)     = w(a);
                [~,a]               = min(abs(tau2(ij) - w));
                tau2r(ij,jk,kl)   = w(a);

                % Record elapsed time
                etime(ij,jk,kl)     = toc;

                % Update counting variable
                I   = I + 1;

                % Display completion percentage every 100 iterations
                if mod(I,100) == 0
                    disp(I/ti*100)
                end

        end
```

```
    end
end
```

B.2.2 Subroutine for the ESPRIT estimation process

```
function  [ w ] = espritCF(y,n,m,B)
%---------------------------------------------------------------------------
% The ESPRIT method for frequency estimation.
%
% INPUTS:    y    -  the data vector
%            n    -  the model order
%            m    -  the order of the covariance matrix
%            B    -  the interleaving factor
%
% OUTPUTS:   w    - the frequency estimates
%
% Original ESPRIT code published in 1996 by R. Moses
% Modified 18 March 2015 by M. I. Bodine.  Added the option for a
% non-unitary interleaving factor.  Based on B Halder and T. Kailath 1997.
%
%---------------------------------------------------------------------------

y   = y(:);             % make sure data vector is a column vector
N   = length(y);        % data length
Nt  = N - B*(m-1);      % number of "snapshots"

% compute the sample covariance matrix
R   = zeros(m,m);
for i = 1 : Nt
   R = R + y( i : B : i+B*(m-1) ) * y( i : B : i+B*(m-1) )' / Nt;
end

% get the eigendecomposition of R; use svd because it sorts eigenvalues
[U,~,~] = svd(R);
S       = U(:,1:n);

phi     = S(1:m-1,:)\S(2:m,:);

% Estimate frequencies
w   = -angle(eig(phi));

return
```

B.3 Local Linear Regression (LLR)

B.3.1 Script for evaluating bias in LLR estimates

```
% LLRBias.m
% Script to calculate bias in Local Linear Regression (LLR) estimates of
% the delay time between two reflectors.  Simulation parameters are defined
```

```
% in two blocks, between dashed lines in the first section.
%
% Author: Martha I. Bodine
% Date: 22 May 2017
%
% Ref: Eric D. Moore and Robert R. McLeod, "Phase-sensitive swept-source
% interferometry for absolute ranging with application to measurements of
% group refractive index and thickness," Opt. Express 19, 8117-8126 (2011).
%
%*************************************************************************
%% Set sampling conditions

clear all

% Physical constants
c0          = 299792458;    % light speed [m/s]

% SIMULATION PARAMETERS, PART 1 ------------------------------------------
lambda1     = 1500e-9;      % sweep start wavelength [m]
lambda2     = 1570e-9;      % sweep end wavelength [m]
tau_t       = 100e-9;       % trigger delay time [s]
tau1        = tau_t/4;      % delay time to first reflector [s]
% ------------------------------------------------------------------------

% Calculate vector of optical frequencies
nu1 = c0/lambda1;   % start frequency [Hz]
nu2 = c0/lambda2;   % end frequency [Hz]
N   = round((nu1 - nu2)*tau_t); % number of samples

nu  = nu1 - (0:N-1).'/tau_t;    % vector of optical frequencies [Hz]
nu  = fliplr(nu);

dnu = nu(1)-nu(2);  % spacing between samples in frequency [Hz]
dtau   = tau_t/N;    % spacing between samples in delay time [s]

% SIMULATION PARAMETERS, PART 2 ------------------------------------------
% vector of delay times to second reflector[s]
tau2   = (tau1 + (50:60)*dtau/5).';

% vector of amplitudes of second reflector relative to first
A2  = [1 2];

w   = hann(N);  % Define window function
% ------------------------------------------------------------------------

%*************************************************************************
%% Superresolved LLR estimate

% Preallocate space for errors and elapsed time
tau1r   = zeros(numel(tau2),numel(A2));
tau2r   = zeros(numel(tau2),numel(A2));
etime   = zeros(numel(tau2),numel(A2));

% Define variables to track execution percentage
ti  = numel(tau2)*numel(A2);    % total number of iterations
I   = 0;    % completed iterations

% Run simulations
```

```
for ij = 1:numel(tau2)
    for jk = 1:numel(A2)

            % Start the timer
            tic

            % Calculate the sampled signal from the measurement
            interferometer
            u   = 1 + A2(jk) + cos(2*pi*nu*tau1) + ...
                    A2(jk).*cos(2*pi*nu*tau2(ij));

            % Window the entire data set
            u   = u.*w;

            % Take the FFT of the windowed data set
            U   = fft(u);

            % Fourier-transform (FT) resolved peak centers
            p1  = round(tau1/dtau) + 1;
            p2  = round(tau2(ij)/dtau) + 1;

            % Distance between FT resolved peak centers in DFT bins
            m   = p2 - p1;

            % LLR window constants
            prw     = abs(m)/2; % spacing between FT resolved peak centers
            % Set the number of data points to be extracted from around
            % each peak center.
            if prw > 200
                prw = 200;  % Max number of points is 200.
            end
            % Set the number of endpoints to be excluded (20%).
            prec    = round(0.2*prw);

            % Window out peaks
            peak1   = U(p1-round(prw/2):p1+round(prw/2)-1);
            peak2   = U(p2-round(prw/2):p2+round(prw/2)-1);

            % Get the unwrapped phase of the IFFT of the shifted peak
            phase1  = unwrap(angle(ifft(ifftshift(peak1))));
            phase2  = unwrap(angle(ifft(ifftshift(peak2))));

            % Curve fit to find slope of phases
            dx      = 1/(numel(phase1));  % x-axis scaling, in index
            x       = dx*(0:numel(phase1)-2*prec-1).';
            y1      = phase1(1+prec:end-prec)/(2*pi);
            y2      = phase2(1+prec:end-prec)/(2*pi);

            f1      = fit(x,y1,'poly1');
            f2      = fit(x,y2,'poly1');

            cf1     = coeffvalues(f1);
            cf2     = coeffvalues(f2);
            m1      = cf1(1);
            m2      = cf2(1);

            % Precision ranging peak location, in index
            % Subtract one so that first point is at time zero.
```

```
            p1 = p1 + m1 - 1;
            p2 = p2 + m2 - 1;

            % Record recovered reflector times
            tau1r(ij,jk)     = p1*dtau;
            tau2r(ij,jk)     = p2*dtau;

            % Record elapsed time
            etime(ij,jk)     = toc;

            % Update counting variable
            I   = I + 1;

            % Display completion percentage every 100 iterations
            if mod(I,100) == 0
                disp(I/ti*100)
            end
    end

end
```

B.3.2 Script for evaluating the precision of LLR estimates

```
% LLRNoise.m
% Script to calculate precision of LLR estimates of the delay time
% between two reflectors of equal amplitude.  Simulation parameters are
% defined in two blocks, between dashed lines in the first section.
%
% Author: Martha I. Bodine
% Date: 22 May 2017
%
% Ref: Eric D. Moore and Robert R. McLeod, "Phase-sensitive swept-source
% interferometry for absolute ranging with application to measurements of
% group refractive index and thickness," Opt. Express 19, 8117-8126 (2011).
%
%***************************************************************************
%% Set sampling conditions

clear all

% Physical constants
c0          = 299792458;    % light speed [m/s]

% SIMULATION PARAMETERS, PART 1 -------------------------------------------
lambda1     = 1500e-9;      % sweep start wavelength [m]
lambda2     = 1570e-9;      % sweep end wavelength [m]
tau_t       = 100e-9;       % trigger delay time [s]
tau1        = tau_t/4;      % delay time to first reflector [s]
% -------------------------------------------------------------------------

% Calculate vector of optical frequencies
nu1 = c0/lambda1;   % start frequency [Hz]
nu2 = c0/lambda2;   % end frequency [Hz]
N   = round((nu1 - nu2)*tau_t); % number of samples

nu  = nu1 - (0:N-1).'/tau_t;    % vector of optical frequencies [Hz]
```

```
nu  = fliplr(nu);

dnu = nu(1)-nu(2);  % spacing between samples in frequency [Hz]
dtau   = tau_t/N;    % spacing between samples in delay time [s]

% SIMULATION PARAMETERS, PART 2 -------------------------------------------
% vector of delay times to second reflector[s]
tau2   = (tau1 + (50:60)*dtau/5).';

% SNR levels to test (This is SNR in the delay time domain.)
SNR     = 10:50:110;

% Number of simulations to run at each SNR
Nnoise  = 2;

w   = hann(N);  % Define window function
% -------------------------------------------------------------------------

%**************************************************************************
%% LLR estimates

% Preallocate space for errors and elapsed time
tau1r   = zeros(numel(tau2),numel(SNR),Nnoise);
tau2r   = zeros(numel(tau2),numel(SNR),Nnoise);
etime   = zeros(numel(tau2),numel(SNR),Nnoise);

% Define variables to track execution percentage
ti  = numel(tau2)*numel(SNR)*Nnoise;    % total number of iterations
I   = 0;    % completed iterations

% Convert SNR from delay time domain to optical frequency domain.
SNR     = SNR - 10*log10(N);

% Run simulations
for ij = 1:numel(tau2)
    for jk  = 1:numel(SNR)
        for kl = 1:Nnoise

            % Start the timer
            tic

            % Calculate the sampled signal from the measurement
            interferometer
            u   = 2+ cos(2*pi*nu*tau1) + cos(2*pi*nu*tau2(ij));

            % Add white Gaussian noise
            u   = awgn(u,SNR(jk),'measured');

            % Window the entire data set
            u   = u.*w;

            % Take the FFT of the windowed data set
            U   = fft(u);

            % Fourier-transform (FT) resolved peak centers
            p1  = round(tau1/dtau) + 1;
            p2  = round(tau2(ij)/dtau) + 1;
```

```
        % Distance between FT resolved peak centers in DFT bins
        m   = p2 - p1;

        % LLR window constants
        prw     = abs(m)/2; % spacing between FT resolved peak centers
        % Set the number of data points to be extracted from around
        % each peak center.
        if prw > 200
            prw = 200;  % Max number of points is 200.
        end
        % Set the number of endpoints to be excluded (20%).
        prec    = round(0.2*prw);

        % Window out peaks
        peak1   = U(p1-round(prw/2):p1+round(prw/2)-1);
        peak2   = U(p2-round(prw/2):p2+round(prw/2)-1);

        % Get the unwrapped phase of the IFFT of the shifted peak
        phase1  = unwrap(angle(ifft(ifftshift(peak1))));
        phase2  = unwrap(angle(ifft(ifftshift(peak2))));

        % Curve fit to find slope of phases
        dx      = 1/(numel(phase1));  % x-axis scaling, in index
        x       = dx*(0:numel(phase1)-2*prec-1).';
        y1      = phase1(1+prec:end-prec)/(2*pi);
        y2      = phase2(1+prec:end-prec)/(2*pi);

        f1      = fit(x,y1,'poly1');
        f2      = fit(x,y2,'poly1');

        cf1     = coeffvalues(f1);
        cf2     = coeffvalues(f2);
        m1      = cf1(1);
        m2      = cf2(1);

        % Precision ranging peak location, in index
        % Subtract one so that first point is at time zero.
        p1 = p1 + m1 - 1;
        p2 = p2 + m2 - 1;

        % Record recovered reflector times
        tau1r(ij,jk,kl)     = p1*dtau;
        tau2r(ij,jk,kl)     = p2*dtau;

        % Record elapsed time
        etime(ij,jk,kl)     = toc;

        % Update counting variable
        I   = I + 1;

        % Display completion percentage every 100 iterations
        if mod(I,100) == 0
            disp(I/ti*100)
        end

    end

end
```

```
end
```

B.4 Candan's Estimator

B.4.1 Script for evaluating bias in Candan estimates

```
% CandanBias.m
% Script to calculate bias in Candan estimates of the delay time between
% two reflectors.  Simulation parameters are defined in two blocks, between
% dashed lines in the first section.
%
% Author: Martha I. Bodine
% Date: 22 May 2017
%
% Ref: C. Candan, "Fine Resolution Frequency Estimation From Three DFT
% Samples: Windowed Case," Elsevier Signal Processing, v. 114, p. 245-250,
% Sept. 2015.
%**************************************************************************
%% Set sampling conditions

clear all

% Physical constants
c0          = 299792458;    % light speed [m/s]

% SIMULATION PARAMETERS, PART 1 -------------------------------------------
lambda1     = 1500e-9;      % sweep start wavelength [m]
lambda2     = 1570e-9;      % sweep end wavelength [m]
tau_t       = 100e-9;       % trigger delay time [s]
tau1        = tau_t/4;      % delay time to first reflector [s]
% -------------------------------------------------------------------------

% Calculate vector of optical frequencies
nu1 = c0/lambda1;   % start frequency [Hz]
nu2 = c0/lambda2;   % end frequency [Hz]
N   = round((nu1 - nu2)*tau_t); % number of samples

nu  = nu1 - (0:N-1).'/tau_t;    % vector of optical frequencies [Hz]
nu  = fliplr(nu);

dnu = nu(1)-nu(2);  % spacing between samples in frequency [Hz]
dtau   = tau_t/N;    % spacing between samples in delay time [s]

% SIMULATION PARAMETERS, PART 2 -------------------------------------------
% vector of delay times to second reflector[s]
tau2   = (tau1 + (1:50)*dtau/5).';

% vector of amplitudes of second reflector relative to first
A2  = [1 2];

w   = hann(N);  % Define window function
% -------------------------------------------------------------------------
```

```
%*************************************************************************
%% Super-resolved Estimate

% Preallocate space for errors and elapsed time
tau1r   = zeros(numel(tau2),numel(A2));
tau2r   = zeros(numel(tau2),numel(A2));
etime   = zeros(numel(tau2),numel(A2));

% Define variables to track execution percentage
ti  = numel(tau2)*numel(A2);    % total number of iterations
I   = 0;    % completed iterations

% Get the correction factor for the window function
cN  = correction_factor(w);

% Run the simulations
for ij = 1:numel(tau2)
    for jk = 1:numel(A2)

            % Start the timer
            tic

            % Calculate the sampled signal from the measurement
            % interferometer
            u   = 1 + A2(jk) + cos(2*pi*nu*tau1) + ...
                    A2(jk).*cos(2*pi*nu*tau2(ij));

            % Window the entire data set
            u   = u.*w;

            % FT resolved peak centers
            p1      = round(tau1/dtau) + 1;
            p2      = round(tau2(ij)/dtau) + 1;

            % Offset estimate
            delta1  = candan_estimate(u,p1,cN);
            delta2  = candan_estimate(u,p2,cN);

            % Precision ranging peak locations, in index
            p1      = p1 + delta1 - 1;   % Subtract one so that first point
                                           is at time zero.
            p2      = p2 + delta2 - 1;

            % Record recovered reflector times
            tau1r(ij,jk)     = p1*dtau;
            tau2r(ij,jk)     = p2*dtau;

            % Record elapsed time
            etime(ij,jk)     = toc;

            % Update counting variable
            I   = I + 1;

            % Display completion percentage every 100 iterations
            if mod(I,100) == 0
                disp(I/ti*100)
            end
    end
```

```
end
```

B.4.2 Script for evaluating the precision of Candan estimates

```
% CandanNoise.m
% Script to calculate precision of Candan estimates of the delay time
% between two reflectors of equal amplitude.  Simulation parameters are
% defined in two blocks, between dashed lines in the first section.
%
% Author: Martha I. Bodine
% Date: 22 May 2017
%
% Ref: C. Candan, "Fine Resolution Frequency Estimation From Three DFT
% Samples: Windowed Case," Elsevier Signal Processing, v. 114, p. 245-250,
% Sept. 2015.
%************************************************************************
%% Set sampling conditions

clear all

% Physical constants
c0          = 299792458;    % light speed [m/s]

% SIMULATION PARAMETERS, PART 1 -----------------------------------------
lambda1     = 1500e-9;      % sweep start wavelength [m]
lambda2     = 1570e-9;      % sweep end wavelength [m]
tau_t       = 100e-9;       % trigger delay time [s]
tau1        = tau_t/4;      % delay time to first reflector [s]
% ----------------------------------------------------------------------

% Calculate vector of optical frequencies
nu1 = c0/lambda1;   % start frequency [Hz]
nu2 = c0/lambda2;   % end frequency [Hz]
N   = round((nu1 - nu2)*tau_t); % number of samples

nu  = nu1 - (0:N-1).'/tau_t;    % vector of optical frequencies [Hz]
nu  = fliplr(nu);

dnu = nu(1)-nu(2);  % spacing between samples in frequency [Hz]
dtau   = tau_t/N;    % spacing between samples in delay time [s]

% SIMULATION PARAMETERS, PART 2 -----------------------------------------
% vector of delay times to second reflector[s]
tau2   = (tau1 + (1:50)*dtau/5).';

% SNR levels to test (This is SNR in the delay time domain.)
SNR     = 10:50:110;

% Number of simulations to run at each SNR
Nnoise  = 2;

w   = hann(N);  % Define window function
% ----------------------------------------------------------------------

%************************************************************************
```

```
%% Super-resolved Estimate

% Preallocate space for errors and elapsed time
tau1r   = zeros(numel(tau2),numel(SNR),Nnoise);
tau2r   = zeros(numel(tau2),numel(SNR),Nnoise);
etime   = zeros(numel(tau2),numel(SNR),Nnoise);

% Define variables to track execution percentage
ti  = numel(tau2)*numel(SNR)*Nnoise;    % total number of iterations
I   = 0;    % completed iterations

% Convert SNR from delay time domain to optical frequency domain.
SNR     = SNR - 10*log10(N);

% Get correction factor
cN  = correction_factor(w);

% Run the simulations
for ij = 1:numel(tau2)
    for jk  = 1:numel(SNR)
        for kl = 1:Nnoise

            % Start the timer
            tic

            % Calculate the sampled signal from the measurement
            % interferometer
            u   = 2 + cos(2*pi*nu*tau1) + cos(2*pi*nu*tau2(ij));

            % Add white Gaussian noise
            u   = awgn(u,SNR(jk),'measured');

            % Window the entire data set
            u   = u.*w;

            % FT resolved peak centers
            p1      = round(tau1/dtau) + 1;
            p2      = round(tau2(ij)/dtau) + 1;

            % Offset estimate
            delta1  = candan_estimate(u,p1,cN);
            delta2  = candan_estimate(u,p2,cN);

            % Precision ranging peak locations, in index
            % Subtract one so that first point is at time zero.
            p1      = p1 + delta1 - 1;
            p2      = p2 + delta2 - 1;

            % Record recovered reflector times
            tau1r(ij,jk,kl)     = p1*dtau;
            tau2r(ij,jk,kl)     = p2*dtau;

            % Record elapsed time
            etime(ij,jk,kl)     = toc;

            % Update counting variable
            I   = I + 1;
```

```
            % Display completion percentage every 100 iterations
            if mod(I,100) == 0
                disp(I/ti*100)
            end

        end

    end

end
```

B.4.3 Subroutine for the Candan estimation process

```
function [ d ] = candan_estimate( r, k, cN )
%---------------------------------------------------------------------------
% Procedure make superresolved frequency estimator using the method
% described by Candan.
%
% INPUTS:   r    -  windowed data set
%           k    -  transform limited estimate (an index in data set r)
%           cN   -  coefficient associated with the window used on data set
%                   r
%
% OUTPUTS:  d   -  fine frequency estimate, a fraction of a DFT bin from
%                  the index k
%
% Author: Martha I. Bodine
% Date: 31 October 2016
%
% Ref: C. Candan, "Fine Resolution Frequency Estimation From Three DFT
% Samples: Windowed Case," Elsevier Signal Processing, v. 114, p. 245-250,
% Sept. 2015.
%
%---------------------------------------------------------------------------

% Determine the number of points in the data set
N   = numel(r);

% Calculate DFT of r
R   = fft(r);

% First order estimate of delta
d1  = cN * real( ( R(k-1) - R(k+1) ) / ( 2*R(k) - R(k-1) - R(k+1) ) );

% Second order estimate of delta
r2  = r .* exp( -1i*2*pi/N*d1*(0:N-1) ).';
R2  = fft(r2);
d2  = cN * real( ( R2(k-1) - R2(k+1) ) / ( 2*R2(k) - R2(k-1) - R2(k+1) ) );

% Final estimate of delta
d   = d1 + d2;

end
```

B.4.4 Subroutine for calculating window-specific correction factors

The following Matlab function was written by C. Candan and copied exactly from the author's webpage [156]. I have reproduced it here for completeness.

```
function out = correction_factor(win,N2)
% function out = correction_factor(win,N2)
% Gives the correction factor for the estimator described in [1,2,3]
% for an arbitrary window
%
% [1] C. Candan, "A Method For Fine Resolution Frequency Estimation From
Three
% DFT Samples," IEEE Signal Processing Letters, Vol. 18, No.6, p. 351-354,
% June 2011.
%
% [2] C. Candan, "Analysis and Further Improvement of Fine Resolution
% Frequency Estimation Method From Three DFT Samples,"
% IEEE Signal Processing Letters, vol.20, no.9, pp.913–916, Sept. 2013.
%
% [3] C. Candan, "Fine Resolution Frequency Estimation From Three DFT
% Samples: Windowed Case," Elsevier Signal Processing, vol. 114, p. 245-250,
% Sept. 2015.
%
%
% Input:
% win : Windowing function
% N2  : Number of DFT points
%
% Output:
% out : Correction factor
%
% Note:
% -----
% The case of zero-padding (N2 > length(win)) is identical to the
% correction factor of the zero-padded window, i.e.
% win_zero_padded = [win(:) zeros(N2-length(win),1)];
%
% Some usage examples:
% win = hamming(N)';
% win = window(@hamming,N)';
% win = window(@blackman,N)';
%
% c_N = correction_factor(hamming(16),32);
%
% Oct. 2013,
% Cagatay Candan
%

win = win(:).';

if exist('N2')==0,
    N2 = length(win);
elseif N2~=length(win),
    win = [win zeros(1,N2-length(win))];
end;
```

```
N = length(win);
nvec = 0:N-1;

fd = @(inp) sum(repmat(win,length(inp),1).*exp(1j*2*pi/N*inp(:)*nvec),2);
fdp = @(inp)
1j*2*pi/N*sum(repmat(win.*nvec,length(inp),1).*exp(1j*2*pi/N*inp(:)*nvec),2);


A0 = imag(fd(1)-fd(-1));
A1 = fdp(1) - fdp(-1);

B0 = 2*fd(0) - fd(1) - fd(-1);
B1 = imag(2*fdp(0) - fdp(1) - fdp(-1));
%%%%%%%

c1 = (A1*B0+A0*B1)/B0^2;
out = 1/c1;
```